Dynamics and Stability of Liquid-liquid Thin Films and Suspensions Spreading on a Spinning Disc

Thesis Submitted to AcSIR For the Award of
the Degree of
DOCTOR OF PHILOSOPHY
In Chemical Engineering

By
Subhadarshinee Sahoo
Registration Number: 20EE12A26075

Under the guidance of
Dr. Ashish Orpe
Dr. Pankaj Doshi

CSIR–National Chemical Laboratory, Pune 411008

सीएसआईआर - राष्ट्रीय रासायनिक प्रयोगशाला
(वैज्ञानिक तथा औद्योगिक अनुसंधान परिषद)
डॉ. होमी भाभा मार्ग, पुणे - 411 008, भारत
CSIR - NATIONAL CHEMICAL LABORATORY
(Council of Scientific & Industrial Research)
Dr. Homi Bhabha Road, Pune - 411 008, India

Certificate

This is to certify that the work incorporated in this Ph.D. thesis entitled **"Dynamics and Stability of Liquid-liquid Thin Films and Suspensions Spreading on a Spinning Disc"** submitted by **Ms. Subhadarshinee Sahoo** to Academy of Scientific and Innovative Research (AcSIR) in fulfilment of the requirements for the award of the Degree of **DOCTOR OF PHILOSOPHY**, embodies original research work under our supervision/guidance. We further certify that this work has not been submitted to any other University or Institution in part or full for the award of any degree of diploma. Research material obtained from other sources has been duly acknowledged in the thesis. Any text, illustration, table etc., used in the thesis from other sources, have been duly cited and acknowledged.

Subhadarshinee Sahoo	Dr. Pankaj Doshi	Dr. Ashish Orpe
(Student)	(Research Co-Supervisor)	(Research Supervisor)

Communication Channels
NCL Level DID : 2590
NCL Board No. : +91-20-25902000
EPABX : +91-20-25893300
: +91-20-25893400
FAX
Director's Office : +91-20-25902601
COA's Office : +91-20-25902660
SPO's Office : +91-20-25902664
WEBSITE
www.ncl-india.org

Dedication

This thesis is dedicated to my

Parents and

my brothers
for their love, support,
guidance and understanding.

Abstract

The flow of a liquid film over a horizontal spinning disc has numerous industrial applications including coating, microlithography, atomization etc. In spin coating process, a drop of liquid spreads under the influence of centrifugal force to form a flat thin film at the center and a capillary ridge near the contact line which eventually leads to the formation of so-called FINGERING INSTABILITY. Fingering instability for the spreading of a single Newtonian viscous liquid with a free surface is very well understood in the literature. However, contact line instability in centrifugal spreading of two-layered flows and flow of suspension films is essentially unexplored. This study assesses the impact of the presence of an outer liquid interface and particles on the spreading of a drop of liquid, shape of the capillary ridge, and contact line instability. This work is significant not only from a fundamental perspective, but also due to its applications, viz., in multi-layer coating and micro-encapsulation processes.

The evolution of a two-layer film on a spinning disc is investigated using an axisymmetric 1D model. The governing Navier-Stokes equation for the flow is simplified using lubrication approximation. A precursor layer model is used to relieve the contact line singularity. The evolution equations are solved numerically employing a novel Galerkin finite element method (G/FEM) based approach. Simulation results reveal that with increase in the viscosity ratio, bulkiness of the capillary ridge increases. Further, sharpness of capillary ridge increases with decrease in the surface to interfacial tension ratio. The uniformity of the two-layer film formed, however, was found to be independent of the initial volume ratio of the two liquids used. The axisymmetric simulations, however, do not account for the development of instability in spreading liquid films.

An experimental study on simultaneous spreading of superposed drops (drop-on-drop) of two Newtonian liquids on top of a horizontal spinning disc is, thus, carried out to understand the contact line instability. The flow dynamics is captured using high-

speed camera imaging. The quantitative results of the image analysis are presented for varying volume ratios of the two liquids keeping the inner liquid volume fixed, and compared to the single liquid spreading. For all the volume ratios studied, the inner liquid spreads to a larger extent and breaks into more number of fingers as compared to corresponding single fluid, which is expected due to the lowering in the interfacial tension. The number of fingers N_f observed experimentally is compared to that of the value predicted using available theory for single fluid just by replacing the surface tension of the inner fluid with the liquid-liquid interfacial tension. It is found that the theory over predicts the value of N_f for the inner liquid while it is covered by an outer liquid. A new theory is derived by using linear stability analysis for small but finite surface tension ratio of the two liquids, and it is found that the presence of the outer interface brings down the value of wave number which is equivalent to the decrease in the number of fingers observed in our experiments.

A detailed investigation on the spreading and fingering of thin film of a density-matched non-Brownian suspension spreading on a spinning disc is carried out using high-speed flow visualization experiments. The effect of volume fraction of particles (ϕ_p) on the spreading, onset and evolution of the instability was investigated in detail with the help of image analysis. The results were compared to the spreading in case of Newtonian liquids of similar viscosity or wetting properties. The critical radius for the onset of instability shows an increase with increase in the particle fraction (ϕ_p) before decreasing slightly at the highest value of ϕ_p studied. However, the instability wavelength (λ) exhibits a non-monotonic dependence in this small range of ϕ_p. The behavior is close to a partially wetting liquid for a lower ϕ_p, decreases with increasing ϕ_p eventually showing behavior close to that of a wetting liquid for the largest ϕ_p. This peculiar behavior of λ is governed by the spatial variation of the particle concentration within the capillary ridge.

Keywords: Density-matched suspension, high-speed imaging, Mathematical modeling, Spin coating, Thin-film flow, Two-layer flow

Acknowledgments

First and foremost, I would like to thank my advisors, *Dr. Ashish Orpe* and *Dr. Pankaj Doshi*, for their invaluable guidance, constant encouragement, constructive criticism, and everlasting support. They helped me develop both from professional as well as personal fronts during the course of my PhD and motivated me to pursue high quality research. Thanks to them for showing a lot of patience to help me grow as an independent researcher and for being excellent mentors. I am also grateful to them for patiently going through my manuscripts and thesis. It has been a fantastic experience working with you both!

I thank *Dr. Ashish Lele*, *Dr. Sarika Bhattacharyya*, and *Dr. Suresh Bhat* for being part of my thesis committee and for providing critical and useful feedback on my research work which has helped to improve the quality of my research. I also thank *Dr. Arun Banpurkar* (Pune University), and *Dr. Apratim Chatterji* (IISER, Pune) for appearing in my upgradation seminars. My sincerest thanks to *Dr. M. S. Shashidhar* (Chairman, SAO) and *Dr. Chetan Gadgil* (AcSIR coordinator) for efficiently handling all the document processing relating to PhD and helping us graduate on time.

I appreciate the excellent and advanced courses taught by our course-work instructors: *Dr. Ashish Orpe*, *Dr. Guruswamy Kumaraswamy*, *Dr Pankaj Doshi*, *Dr. Chetan Gadgil*, *Dr. Ravi Kumar*, and *Dr. Leelavati Narlikar*, which has helped me to get a clear fundamental understanding of the major subjects of my research field without which it would have been difficult to pursue the tough research with my Bachelor's degree background. I thank CSIR for funding my research work.

It was a great experience to work with *Akash*, as I could learn many new things from him which has helped me in improving my scientific writing skills. Chapter 3 of this thesis is a collaborative work with him. I would also like to acknowledge some of my seniors *Dr. Sumeet Thete*, *Manoj Kumar*, *Dr. Sucheta Gokhale*, and *Dr. Dimpal Nayanit* for encouraging me a lot and helping me with their invaluable guidance while

writing this thesis and some other discussions regarding my future career prospects.

Among the non-academic staffs, I thank *Ms. Purnima Kolhe*, *Komal*, *Vaishali*, *Harshita*, and others from SAO for sorting out the official and hostel accommodation matters. I also thank *Mr. Raheja* (Section Officer, CEPD) and other staff members at the Chemical Engineering Division for their invaluable help while dealing with some administrative matters. I also thank mess cooks of New Hostel for serving nice food during my stay at NCL.

I am grateful to my current and past lab members, *Bhavna madam, Saprativ, Sameer, Mayuresh* and *Profesar* with whom I always had great scientific discussions and lots of fun; *Suvankar, Amit, Sandesh, Rohit, Priyanka, Shraddha, Bharat, Apurva, Shubhada, Sneha, Anushua, Amardeep, Sameena*; thank you all for creating a productive environment in the lab and sharing fun moments especially ordering delicious food. I appreciate the help from my friends *Gunwant, Nilesh, Raja, Amruta, Akshay, Karthika, Gaurav, Suvankar, Sourya, Asheesh,* and *Prathit*. Special thanks to my roommates *Richa* and *Ekta* with whom I always had a great time with lot of shopping, long gossip sessions sharing our frustrations, roaming around places, watching movies and the cooking sessions. You both have been amazing friends and without your help it would have been difficult to be in Pune and finish this thesis work! I also want to acknowledge my friends *Preeti, Barsha,* and *Kiran* for having trust in me and constantly encouraging me throughout my PhD.

Most importantly, I thank my parents (especially my mother) for their eternal care, support, trust and teaching me the value of diligence and patience and advising me to *dream bigger*. I thank my brothers *(Sanjit & Sambit)* for always inspiring me, sharing all the fun, and loving me unconditionally.

Finally, I am grateful to *Lord Jagannath* for this beautiful life.

Subhadarshinee Sahoo

List of Publications

Journal Publications

- **S. Sahoo**, A. V. Orpe, and P. Doshi, Spreading dynamics of superposed drops of two liquids on a spinning disk, *Phys. Fluids* 30, 012110 (2018). *(Featured article for January, 2018)*
- **S. Sahoo**, A. Arora, and P. Doshi, Two-layer spin coating flow of Newtonian liquids: A computational study, *Computers & Fluids 131*, 180 (2016).
- M. Kulkarni, **S. Sahoo**, P. Doshi, and A. V. Orpe, Fingering instability of a suspension film spreading on a spinning disk, *Phys. Fluids* 28, 063303 (2016).

Contributed Talks

- "'16 AIChE Annual Meeting", San Francisco, CA, USA, Nov. 2016
- "APS DFD Annual Meeting", Portland, OR, USA, Nov. 2016
- "Compflu-2016", IIIT Hyderabad, Dec. 2016
- "Mumbai-Pune Soft Matter Meeting", IIT Mumbai, Mar. 2016

Posters

- "'16 AIChE Annual Meeting", San Francisco, CA, USA, Nov. 2016
- "Compflu-2015", IISER Pune, Jan. 2016
- "National Science Day", CSIR-NCL, Feb. 2015
- "Compflu-2014", JNCASR, Bengaluru, Dec. 2014

- "SERB School on Rheology of Complex Fluids: Advanced Computational Methods & Symposium on Rheology of Complex Fluids-2013", IIT Delhi, Dec. 2013
- "CompFlu-2012", IISER Pune, Dec. 2012

Contents

List of Figures

List of Tables

Chapter 1

Introduction

1.1 Motivation

Thin liquid films are predominant in nature and technology. They find applications in diverse areas of science including physics, biology, geology as well as engineering. Thin films are encountered in numerous industrial applications such as coating, soldering, printing, photolithography, and microfluidic device fabrication. Further applications of the spreading thin films are discussed in the reviews by Oron *et al.*[1] and Craster *et al.*[2] Often, their flow behavior plays a crucial role in such applications. A fundamental understanding of thin film flow is, therefore, of paramount importance in design of relevant applications.

Flow of thin films under the influence of body forces such as gravity or centrifugal acceleration often exhibit fascinating dynamics. The examples include wave propagation, wave modulation and transition from periodic to chaotic structure depending on the liquid flow rate, pattern formation, thin-film rupture and hole formation, spreading of fronts, droplet formation at the leading edge of the film as well as development of fingers. The radial flow of a thin liquid film on a rotating horizontal disc is encountered in many industrial processes such as spin coating and spinning disc atomization. Spin coating process is used in the manufacturing of compact discs, TV screens, optical mirrors, anti-reflective coatings in solar cell applications, microlithography and many others.[3–9] These thin film flows are prone to exhibit instability behavior result-

ing in the formation of non-uniform films, which is undesirable in coating applications. However, as mentioned later on, the instability is desirable in certain applications.

1.1.1 Thin film flow on a spinning disc

A drop of liquid placed on the axis of rotation of a spinning substrate spreads under the influence of centrifugal force to form a flat thin film at the center and a capillary ridge near the air-liquid-substrate contact line, which eventually leads to the formation of instability. The centrifugal force acting on the fluid pushes it in the radially outward direction while, the viscous force tends to resist its motion in the so called "outer" region away from the contact line. In the capillary ridge near the contact line, known as "inner" region, the flow is governed by a balance between surface tension and centrifugal force. As the flow evolves with time, the capillary ridge becomes unstable to perturbations in the azimuthal direction, leading to the development of fingers at the liquid-substrate contact line. These fingers then, spread radially towards the periphery of the disc, wherein they break into fine droplets. A schematic of the various stages of a drop spreading process on a spinning disc is shown in Fig. 1.1.

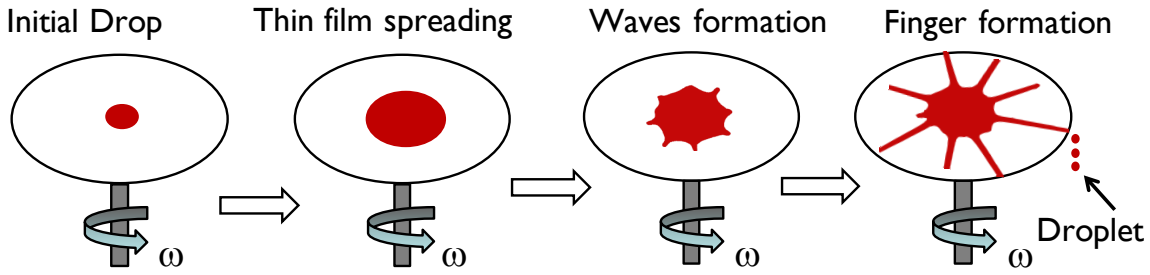

Figure 1.1: Different stages of spreading of a drop of liquid in spin-disc flow.

If the viscosity of fluid is low, Coriolis force comes into play and bending of the fingers is observed[10]. Due to the azimuthal deflection and merging of fingers at the base, the spreading area and critical time for the onset of instability increases.

In coating applications, apart from the requirement of a uniform thin film, the role of evaporation becomes increasingly important in determining the rate of thinning of

the film during the final processing stage. However, the rate of evaporation remains constant, independent of the film thickness. This takes over as the dominant process until the fluid gets completely dried up.

Thin film flow finds application in pharmaceutical industries to form drug micro-spheres for encapsulation in drug delivery. Spinning disc atomization is the predominant method to form these micro-spheres of desired shape, size and density[11–14]. In a spinning disc atomizer, a nozzle introduces fluid at the center of a spinning disc rotating at a very high speed. Centrifugal force carries the fluid in the radially outward direction. Once it reaches the edge of the disc, the fluid gets thrown off from the disc. The liquid forms fingers (or ligaments) which eventually break up due to the surface tension of the liquid to form fine droplets. Depending on the inlet flow rate and rotational speed of the disc, three distinct droplet disintegration modes have been observed[15–18]: (i) direct drop formation, (ii) ligament formation, and (iii) sheet formation. At low flow rates, direct droplet formation is observed at the edge of the disc where discrete drops of uniform size are formed. With increasing flow rates, there is a transition from direct droplet formation to ligament formation. The drops formed are smaller in this mode than the earlier mode and are generated by break up of long jets. Film disintegration emerges at even higher flow rates and the surface of the atomizing disc is covered by a continuous film moving from the center to the circumference of the disc and extending beyond, which eventually disintegrates creating a wide spectrum of drop sizes.

Another application of radial thin film flow is the spinning disc reactor (SDR) technology which is employed to produce drug crystals (API) in pharmaceutical industries[19,20]. In a SDR, the film is subjected to very high shear stress (τ), promoting very high heat-transfer rates between the film and the disk, and high mass-transfer rates between the liquid streams or between the film and the gas in the surrounding atmosphere. High rotational speed offers reaction optimization, resulting in better mixing, and shorter residence times. The SDR is, in principle, capable of producing fine crystals with a very narrow size distribution.

1.1.2 Challenges in the Study of Thin Film Flow

Thin films flows on the scales ranging from nano- to macro have been extensively studied through experiments, simulations, and, mathematical analysis. The spreading of a drop of liquid on a spinning disc is a free surface problem with a moving contact line. These flows are complex in nature. Theoretical investigation of this type of problem requires finding the location of the free surface as part of the solution of the non-linear equation; making it more complex.

The thickness and uniformity of thin films which are important parameters for their technological applications, depend on experimental conditions including the rotation time and speed, physical properties of the fluids, and evaporation rates, concentration of the suspension, and characteristics of the substrate surface. The flow behavior as a function of the fluid properties in thin film spreading helps to recognize its efficient performance in practical applications and has been investigated for single-layer Newtonian fluids by many research groups through different theory and experiments. One of the outstanding and practically relevant problem is to understand the spreading behavior of multi-layered films. Additionally it is also important to understand the behavior of thin film flow of non-Newtonian fluids like polymeric fluids and suspensions which are encountered in practical applications. The fundamental investigation of thin film flow in above-mentioned system forms the overall objective of this work.

1.2 Organization of the Thesis

The outline of the thesis is provided in Fig. 1.2. The left column in Fig. 1.2 represents the particular problem being investigated and corresponding key result is shown on the right side.

The remainder of this thesis is organized as follows. In chapter 2, previous experimental studies as well as modeling efforts are summarized in a comprehensive literature survey. The gaps in the existing literature are identified and detailed objective of the thesis is presented.

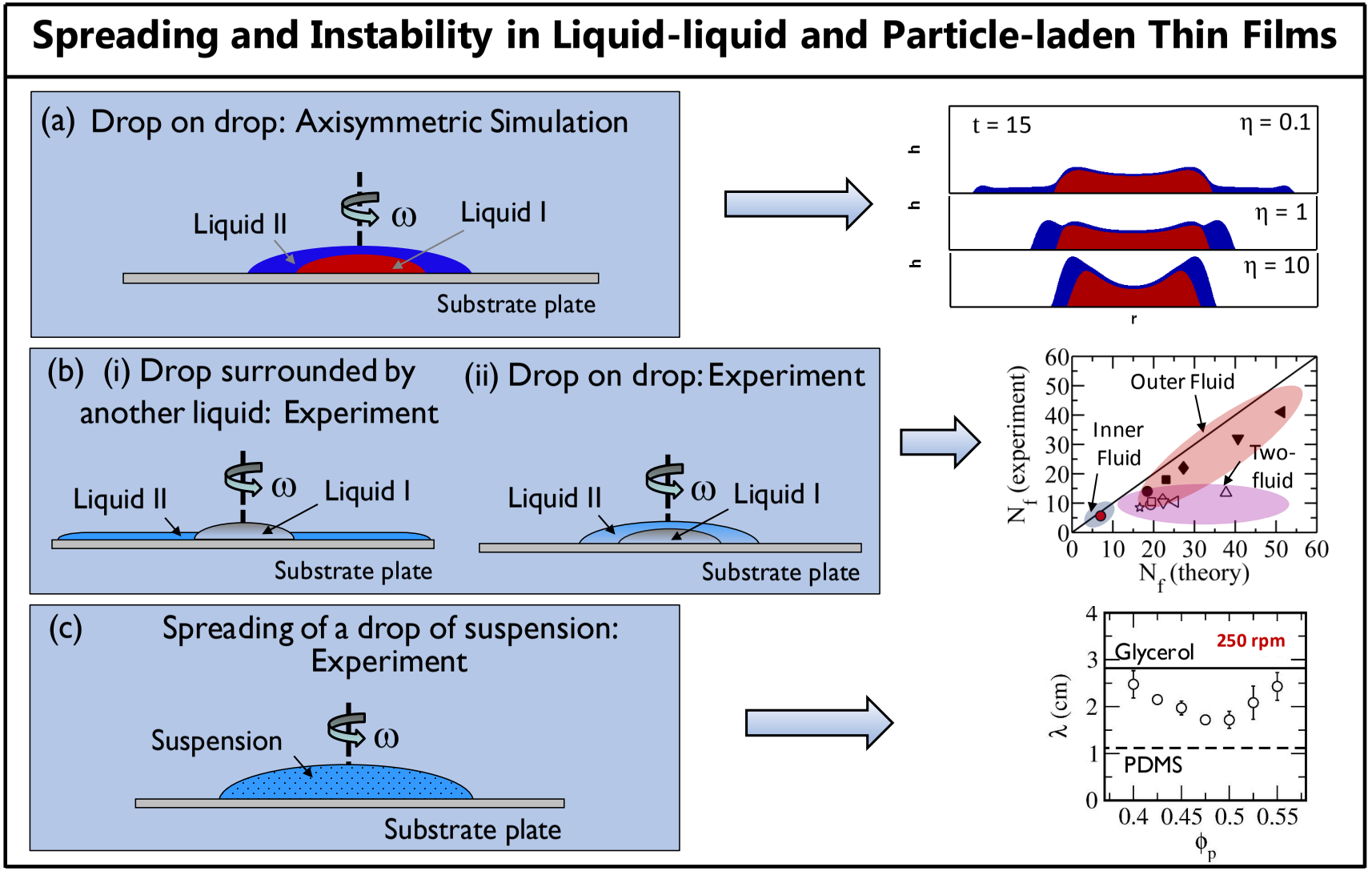

Figure 1.2: Overview of the thesis.

Chapter 3 discusses about the 1D axisymmetric mathematical modeling of a two-layer spin coating process. The governing equations for the flow of one fluid on top of the other on a spinning disc are solved numerically to investigate the effect of various fluid property ratios (i.e., viscosity ratio, interfacial tension ratio) and also, other process parameters such as volume ratio of the two fluids and precursor layer thicknesses. Fig. 1.2(a) depicts the effect of viscosity ratio of the two fluids on the formation of two-layer film.

In chapter 4, an experimental study on superposed drops of two liquids spreading on a spinning disc is discussed in detail. The experiments are carried out for varying volume ratios of the two fluids keeping the inner liquid volume fixed. The flow dynamics is captured using high speed imaging. The quantitative experimental results are presented for the two-fluid case and compared to the single fluid spreading in each case. The comparison between the number of fingers predicted using available theory and observed experimentally are presented in Fig. 1.2(b). A new theory is derived in the limit of small surface tension ratio to explain the effect of presence of outer liquid interface on the finger formation.

Chapter 5 describes a detailed experimental investigation on the spreading and fingering of thin film of a suspension spreading on a spinning disc. High speed imaging technique is used to capture the spreading of the suspension drops. The effect of volume fraction of particles on the spreading, onset and evolution of the instability is investigated in detail. The results are compared to the spreading in case of Newtonian liquids of similar viscosity or wetting properties. Fig. 1.2(c) depicts the wavelength of instability (λ) as a function of the increasing particle volume fraction.

Finally, in Chapter 6, the major findings and conclusions are summarized. Various outstanding issues are identified and suggestions for future research are provided.

Chapter 2

Review of Literature

Centrifugal drop spreading on a solid substrate finds multitude of applications in industrial processes as discussed in the previous chapter. Therefore, extensive research has been carried out in this area to understand the film spreading dynamics and instability. In this chapter, an overview of the research on thin film flow on a solid substrate under an external forcing (gravity or centrifugal) is presented. Yet, the primary focus will be on centrifugally driven thin films. Nevertheless, due to inherent similarities between the spreading mechanisms in case of films driven by gravity and centrifugal force, we will review the previous research work in the former case wherever necessary. Overall, the existing literature on thin film flow can be broadly divided into two major categories i.e. thin film spreading and fingering instability. In the subsequent sections, we will explore the existing experimental as well as theoretical work in the above two categories based on the type of fluid used i.e. Newtonian, non-Newtonian or suspension.

2.1 Thin Film Spreading

Preparation of uniform films of desired thickness by spin coating has been widely studied in the past. In these flows, typically, the characteristic length scale in the direction perpendicular to the plane of the flow (i.e. the film thickness), is much smaller than the characteristic length scale in the direction of flow. Generally, the existence

of the small aspect ratio (small parameter, ϵ) is exploited to expand the governing Navier-Stokes equations in a perturbation series in powers of ϵ. This approximation is known as *"Lubrication Approximation"* or *"Long-wave Approximation"*. It has been used extensively in the modeling of thin-film flow due to the thinness of the coating film. It reduces the governing equations as well as boundary conditions to a much simplified system consisting of a non-linear partial differential equation still capable of capturing the dominant physics.

2.1.1 Flow of Viscous Newtonian Fluids

The pioneering analysis of spin coating flow was performed by Emslie *et al.*[21] (1958). The authors considered the spreading of a thin axisymmetric film of Newtonian fluid on a planar substrate rotating with a constant angular velocity. They modeled the flow by applying lubrication theory on Navier-Stokes equation and obtained an equation determining the evolution of the film thickness due to purely centrifugal and viscous forces:

$$\frac{\partial h}{\partial t} = -\frac{\rho\omega^2}{3\eta}\frac{1}{r}\frac{\partial}{\partial r}(r^2h^3), \tag{2.1}$$

where, ρ is the density of the fluid, η is the viscosity of the fluid, ω is the rotational speed of the disc, r is the radial coordinate and h is the height of the free surface. The model ignored the effect of inertia, gravitational, capillary, and Coriolis forces. Using the method of characteristics, they were able to examine the evolution of a variety of known initial surface contours. The solution shows that spin coating process always yields a uniform flat film for any given initial profile.

Although, Emslie *et al.*[21] made a seminal contribution in this field, their study was not quite general to be applicable to practical coating situations. One of the limitations of their study was the assumption that the flow is governed by the balance between centrifugal and viscous force and all other forces are relatively unimportant. As we will discuss later, the outer rim (contact line) of a spreading film is always susceptible to instability which arises when the surface tension force becomes important. Hence, neglecting the surface tension force is not a valid assumption and thus produces

undesirable results. Secondly, the model is valid only for Newtonian fluids, whereas materials used for practical coating applications are generally non-Newtonian.

Subsequent authors have generalized the work of Emslie *et al.*[21] to include various additional physical effects, including surface tension[22,23], surface shear[24], surface roughness[25], Coriolis effects[10,26–29], fluid inertia[30], evaporation and absorption[31].

Later, Moriarty *et al.*[32] (1991), presented a solution for the evolution of the free surface profile for a thin liquid film flowing under gravity using asymptotic analysis. The study was carried out assuming surface tension to be small in the lubrication equation. These authors divided the flow domain into an outer region (region far away from contact line), and an inner region (region close to contact line). The composite solution applicable throughout the flow domain was found by matching outer and inner region solutions that were obtained separately. In order to verify the accuracy of the asymptotic solutions, they also simulated the model numerically by using a finite difference time marching scheme which solves the whole lubrication equation, without making any small surface tension assumptions. The composite solution matched very well with their numerical solution of the governing lubrication equation obtained using precursor film model for the contact line (See 2.1.2), for small surface tension values. The analysis was extended for two different types of flow namely spin coating flow, and the flow caused by blowing a jet of air. Their analysis manifested that all these flows share a common mechanism which led to the instability at the front of the propagating film. The authors' analysis was based on the assumption of low Reynolds number flow as was done by Emslie *et al.*[21] The method of asymptotic expansion used in their study can also be used to analyze the solution for arbitrary Reynolds number flows which was successfully carried out by Brian Higgins.[33]

2.1.2 Contact Line Paradox

As discussed in Chapter 1, when a contact line is driven by a constant force, the fluid interface becomes unstable and breaks into fingers. In particular, a moving contact line coupled with "no-slip" boundary condition at the solid surface leads to divergence

of stresses as well as viscous dissipative forces which is known as the so-called *"contact line paradox"*. In general context of partially wetting fluids, this stress singularity is relieved by either relaxing the no-slip boundary condition, or by accounting for the effects of the long range intermolecular van der Waals force (disjoining pressure). In the former case, the contact line is allowed to slip with a velocity proportional to the stress at that point.[34–37] However, in case of completely wetting fluids, experimental evidence has revealed the presence of a microscopic film in front of the apparent contact line. In a precursor layer model, it is assumed that the liquid is never in direct contact with the solid surface. It allows no-slip condition to be applicable everywhere; thereby removing the contact line singularity.[38–43] Diez *et al.*[44] have studied the contact line motion using global models where either precursor film or slip are allowed and have concluded considerable computational advantage of the precursor film model over slip model.

McKinley *et al.*[45], in 1999, formulated a general model depicting the evolution of free surface for the flow of a viscous Newtonian liquid on a rotating disc. The authors used a generalized *Tanner Law* to include the dynamics of contact line (See 2.1.2) and obtained a dimensionless equation for a Newtonian fluid spreading on a rotating disc:

$$Ch_t + \frac{1}{r}\left[\frac{rh^3}{3}\left(\left(\frac{1}{r}(rh_r)_r - G^2 h\right)_r + Jr\right)\right]_r = 0 \ , \tag{2.2}$$

where, $J = \rho\omega^2 L^3/\sigma\theta_0$ is the measure of centrifugal force, $C = \kappa\eta/\sigma\theta_0^3$ (κ being the characteristic horizontal velocity scale) is the capillary number, which measures the competition between the viscous force and surface tension force (capillary force) and $G^2 = \rho g L^2/\sigma$ is the Bond number, which is the ratio of the gravitational force to the surface tension force.

The above model is helpful in understanding the dynamics of the flow of thin films in various conditions just by a simple modification in the dimensionless parameters. Also, by appropriate adjustment of the constants in the above equation, it is possible to recover the model equations derived in previous studies. For example, replacing $G = 0$ in the above equation results in the equation provided by Moriarty *et al.*[32]

Moreover, the governing equation in terms of dimensionless groups helps in relating the spin coating flow with other flows like draining of a liquid drop under gravity and spreading of a liquid drop by a jet of air. These authors analyzed the flow in the limits of small capillary number ($C \to 0$), in which the flow can be treated as quasi-static, which essentially means that the contact line moves very slowly relative to the bulk of the fluid. The drop profiles are predicted by changing the initial condition in the simulation. Further, they carried out a linear stability analysis of these profiles to small perturbations which is discussed in the next section.

More recently, Wilson *et al.*[23] studied the axisymmetric spreading of Newtonian fluid on a spinning disc for a constant angular speed. Using asymptotic methods, they were able to capture the qualitative features of the flow (prior to instability formation) in the asymptotic limit of small surface tension. However, quantitative agreement with the experimental results[46,47] was obtained by numerically solving the governing equations using slip model (See 2.1.2) employing both static and dynamic contact angle conditions, including finite surface tension effects.

Although a majority of work over the past few decades has focused on the analysis of a single evolution equation, in recent years the field has moved towards the study of thin film flows governed by a system of coupled evolution equations for the film thickness. More recently, McIntyre Brush[48] used lubrication theory to derive an axisymmetric model for the spin coating of two immiscible vertically stratified Newtonian thin films which included gravitational, van der Waals, capillary and viscous forces, differences in liquid layer properties and evaporation/condensation effects. However, the simulation results were reported without considering the effect of capillary force and for films which are infinite in extent. The authors showed that the disturbances to the lower layer have a greater impact on the upper layer than those of disturbances of the upper layer on the lower layer and the disturbances along the upper gas-liquid free surface propagate outward more rapidly than those along the lower liquid-liquid interface. Dandapat and Singh[49] have established the role played by viscosity, initial film thickness and density ratio (of two different liquids) on final film thickness (for films which are infinite in extent) at large time for large Reynolds

number. The initial rate of film thinning was found to increase for smaller thickness of the top layer. However, the overall effect of the various parameters was insensitive to the final film thickness at large time. In a recent article by Dandapat and Singh [50], the authors presented long time scale solution for an unsteady two-layer liquid film flow on a horizontal rotating disc analytically and explained the findings, physically for small Reynolds number. It was observed that the final film thickness attains an asymptotic value at large time. Their results established that viscous force dominates over centrifugal force and upper layer thins faster than lower layer at large time.

2.1.3 Flow of Non-Newtonian Fluids

Considering the fact that the fluids used for for practical applications are mostly non-Newtonian, Acrivos *et al.* [51] (1960) extended the analysis of Emslie *et al.* [21] for the flow of a non-Newtonian power-law fluid on a rotating disc. Using similarity transformation, the authors were able to examine the effect of spinning on the uniformity of the film for varying power-law indices. The study concluded that centrifugation of a non-Newtonian fluid film that is initially uniform tends to destroy the uniformity and this departure from uniformity is particularly noticeable for fluids with significant non-Newtonian behavior. In fact, the results showed a central spike followed by a sloping region dependent on the power-law index. Thus, the study suggested that, it is challenging to develop a uniform coating film of complex materials like polymers which show non-Newtonian characteristics.

Later, Jenekhe *et al.* [52] (1984), showed that this central spike was an artifact of the power-law (viscosity) constitutive model. Using Carreau model, they were able to show that spin coating results in thin uniform flat films for any given initial profiles. Therefore, they concluded that the power-law fluids are an improper choice for modeling of axisymmetric free surface flows. Subsequently, there have been a few numerical and analytical studies of such flows. [53,54] However, almost all of these studies have investigated the flat film formation away from the contact line neglecting the effect of surface tension.

Very recently, Charpin *et al.* [55] have numerically studied the axisymmetric spin

coating flows of shear thinning fluids including surface tension effect. The authors used power-law and Ellis constitutive models to depict the rheology of the fluid. The movement of contact line was modeled using a precursor layer condition, i.e. the fluids are fully wetting. The authors showed that including the surface tension term removes the spike in the central part of the film as reported in few previous studies.[51,52] Moreover, the study established that shear thinning power-law fluids, in general, spread faster than the Newtonian fluids only except for few cases close to Newtonian fluids where the trend was found to be reversed.

Apart from the above studies, Hu and Kieweg[56] studied the capillary ridge formation in the flow of power-law fluids down an inclined plane. The authors have shown that the height of capillary ridge increased with larger value of surface tension, steeper inclination angle, higher initial thickness, and more Newtonian nature of the fluids. Moreover, their study provided initial insights into the effect of process parameters on the formation and shape of the capillary ridge in non-Newtonian fluids. However, the study lacks in depicting the dynamics of fingering instability.

Most recently, Arora *et al.*[57] performed a numerical study to examine the effect of non-Newtonian nature of the fluid on the film evolution and associated contact line instability using lubrication theory. The movement of the contact line was modeled using a constant angle slip model. Numerical results revealed that spreading rate of the fluid strongly depends on power-law exponent (n). It was found to increase with the increase in the shear thinning nature of the fluid and decreases with the increase in shear thickening nature of the fluid. Moreover, the shape of the capillary ridge was found to becomes sharper with an increase in the value of n. The fingering instability for shear thinning and shear thickening fluids carried out in this work will be discussed in the next section.

2.2 Fingering Instability

Typically. for a liquid drop spreading on a solid substrate, the *contact line* refers to the boundary where the three phases (solid- liquid-air) meet. *Fingering instability*

describes how the moving contact line at the front develops perturbations during flow. Forced spreading of a straight or circular contact line, due to gravity or centrifugal force, respectively, is unstable to the formation of instability (fingers) in a direction transverse to the flow direction. The examples of such flows include flow of a viscous liquid flowing down an inclined plane, liquid drop spreading on a rotating disc etc. These flows are associated with accumulation of liquid at the flow front (contact line) leading to the development of instability in the cross-flow direction. The coating fluid preferentially flows through the fingers and bypasses some portions of the substrate leaving a defective end product. This instability in thin-film flow has been studied extensively in the literature to understand the underlying mechanism behind finger formation, which is discussed below in detail.

2.2.1 Flow of Liquids

The mechanism behind this fingering instability was first studied experimentally by Huppert[58], who described the instability of a driven contact line for fixed volume of a liquid flowing down an inclined plane experimentally. The author presented an expression for the wavelength of the fingers, which depends on the surface tension of the fluid but independent of the viscosity of the liquid. Surface tension becomes important near the contact line which is shown by scaling arguments. The experimental data of Huppert suggested that the formation of rivulets occur on capillary length scale. Thus, for the first time it was confirmed that the fingering instability in coating flows is hydrodynamic in origin.

A linear stability of the Newtonian capillary ridge for a film flowing down an inclined plane was first carried out by Troian *et al.*[59] using a precursor layer model. Their stability analysis of the quasi-static solution in the inner region showed that, it is always unstable to sufficiently long-wavelength disturbances in the cross-flow direction. Moreover, the instability was found to be the largest near the contact line, where the surface tension force becomes comparable with the viscous and gravitational force. The dimensionless growth rate of the most unstable mode was found to be approximately 0.5, depending weakly on the thickness of the precursor film. The *most*

unstable mode is defined as the wavelength at which the initial disturbance grows most rapidly and is the most likely initial spacing between ridges for a randomly imposed perturbation. The mechanism of this instability has been discussed by Bertozzi and Brenner and Spaid and Homsy.[22,60]

A more general analysis of the stability of these thin-films was carried out by McKinley *et al.*[61] for arbitrary capillary cumber (C) values. It was found that for both the cases ($C = 0$ and $C \neq 0$), the drop was found to be unconditionally unstable to perturbations in cross-flow direction resulting into finger formation (discussed in the upcoming section). Overall, the eq. 2.2 describing the spin coating flow is highly non-linear and results into various instabilities such as sudden jumps and formation of fingers. The study established that for producing a uniform thin film of desired thickness by spin coating, finger formation is an undesirable phenomenon, yet inevitable, and thus, needs to be controlled. The following section highlights the previous research work in this field to understand the underlying mechanism behind the fingering instability associated with thin film flows.

Experimental studies using viscous Newtonian liquids under external forcing have demonstrated that the film height profile is nearly flat except near the advancing front where liquid gets accumulated to form a capillary ridge eventually leading to the formation of instability[46,62,63]. Capillary ridge refers to the bump formation at the front of the spreading fluid. First ever experimental study on the fingering instability in case of a spinning drop was carried out by Melo *et al.*[62] They have performed experiments using silicone oils for a range of viscosities (very high viscosity), rotation speeds, and fluid volumes on a silicon substrate and measured the time evolution of the drop profile, critical radius for the onset of instability and the fastest growing instability wavelength. The authors introduced theoretical scaling parameters for which the dimensionless spreading radius as well as the film thickness data for various experimental parameters collapsed onto two separate master curves when plotted against dimensionless time. In other words, the spreading radius ($R(t)$) and the film thickness (h) followed the power law dependence ($R \propto t^{1/4}$ and $h \propto t^{-1/2}$), as predicted by the lubrication theory, irrespective of the experimental conditions

considered.

It was confirmed that the existence of a bump in the profile, which gives rise to capillary pressure gradient in a direction transverse to the main flow, is the main cause of instability that occurs in thin films which was also shown by Troian *et al.*[59]. The authors analyzed the occurrence of instability by introducing a dimensionless parameter, β, defined as a ratio between capillary forces and centrifugal force. It was found that for small β, indicating large centrifugal force, the critical radius for the onset of instability (R_c) as well as the wavelength of instability (λ) are functions of β. It was experimentally also shown that for $\beta < 0.01$, both the above quantities increase. Hence, they concluded that the model based on lubrication approximation is invalid for smaller β (β<0.01), i.e. when centrifugal forces become large. The study, thus, provided the range of applicability of the lubrication theory.

A large number of experimental studies have been carried out later on, to study initial instability characteristics by varying experimental parameters like rotational speed, drop volume, wetting properties of the fluid (surface tension and contact angle), and the rheology of the fluid. Fraysse and Homsy[46] performed experiments for both Newtonian and non-Newtonian fluids to study the instability characteristics with the change in the fluid properties and process parameters mentioned above. The ultimate objective was not only to study the wavelength of instability at the onset of fingering, but also to predict the growth rate of these instabilities. It was observed that the wetting properties of the liquid play an important role in determining R_c and λ. For the liquids which have poor wetting properties (high surface tension), onset of instability occurs much earlier as compared to liquids with good wetting properties. Comparison of these experiments with the linear stability theory of Troian *et al.*[59] showed good quantitative agreement for both the wavelength and growth rate of the instability, the values for onset time and critical radius being taken from the experiment. Their analytical expression for calculating the number of fingers has been verified by several experimental as well as theoretical studies. Although, Fraysse and Homsy[46] were successful in predicting the effect of surface tension, they failed to show the dependence of instability characteristics on the rotational speed, volume

of the fluid and even on the viscoelastic nature of the fluid.

Both Melo *et al.*[62] and Fraysse and Homsy[46] have shown that the most unstable wavelength was independent of the drop size as well as rotation speed of the disc in the range of their experimental parameters considered. In addition, they both have reported slight discrepancy between the theory and experiment, for the asymptotic spreading rate before instability (slope of $^1/_3$ instead of predicted theoretical slope of $^1/_4$). This discrepancy occurred due to the assumption of a flat film shape in the theory, which in practice, evolves with time.

Recently, de Bruyn and co-workers[63] reported an experimental study on the centrifugal drop spreading in which they went beyond the instability onset and showed how the fingers grow once the instability occurs in the system. In order to study the growth rate of fingers, they have performed a series of experiments using a drop of low-viscosity silicone oil by varying the rotational speed and initial volume of the fluid. Their experimental results showed that the scaling used for non-dimensionalization in the analysis of Frasse and Homsy was inappropriate causing the discrepancy between theory and experiments for the evolution of the drop radius. Furthermore, they have shown that the instability wavelength as well as growth rate of instability depend on the rotational frequency as well the liquid volume, in contrast to the observations reported by Fraysse and Homsy.[46] In fact, the growth rate was found to increase linearly with the initial volume of the fluid while the relation between the growth rate and rotational speed was highly non-linear.

The previous work was then further extended by Spaid and Homsy[22] to study the instability characteristics of viscoelastic fluids in comparison to that of the Newtonian fluids. They used linear stability analysis and energy analysis method to study the instability of different fluids. It was found that the capillary ridge is more stable in case of viscoelastic fluids as compared to Newtonian fluid. This is expected given the fact that the viscoelastic fluid which possesses a finite restoring force when stretched will always tend to attain its stable free surface profile. Thus, contact line in case of viscoelastic fluid when perturbed will always tend to stabilize the advancing front. It was shown that R_c in case of viscoelstic fluid was larger as compared to that of

Newtonian fluid. Moreover, viscoelastic material having a finite relaxation time, thus, will take longer to respond to the modulations of the contact line. The authors also studied the dynamics of the contact line for two different kinds of models namely slip model and precursor layer model, and found that the dynamics of the viscoelastic fluid was sensitive to the type of contact line model used. However, for Newtonian fluids, the study revealed that instability characteristics is weakly dependent on the contact line model. The above work, thus, proved that the instability will always occur in spin coating process immaterial of the fluid used, the only difference lies in the values of R_c and N_f. All these studies reported in the past address the study on instability characteristics confined to low Re flow (i.e., low rotational speed) which verifies the assumptions of negligible Coriolis force. In an another work, Spaid and Homsy[47] studied the effect of viscoelasticity on the onset and evolution of fingering instability. They have found that elastic force stabilizes the drop by increasing the critical radius and delaying the onset time of instability. They also showed that increase in the rotational speed has more pronounced effect on the stabilization.

Recently, probably the most advanced 3D model for the spreading of a drop to understand the fingering instability in spin coating process was reported by Schwartz and Roy.[28] Numerical simulation of the model was found to be in accord with the previous experiments.[46] The study also investigated the effect of Coriolis force in a spin coating process. Several theories have been reported in the literature to study the effect of Coriolis force. The effect of Coriolis force can be observed by increasing the flow Re. They used properties of Boger fluid as reported in the experiments by Homsy and co-workers[46], and simulated the system by reducing the viscosity by a factor of 14, thus increasing Re to 0.2. It was observed that due to Coriolis force, the fingers deflected in the clockwise direction while the disc rotates in the counter-clockwise direction. In other words, Coriolis force results in bent fingers in which tip of the fingers move in the direction opposite to the direction of rotation of the spinning disc. By invoking a disjoining pressure model for relieving the contact line singularity, the authors also demonstrated that imperfect wetting behavior is the primary reason behind the fingering instability during spin coating.

The most recent work on fingering instability for power-law fluids was carried out by Arora *et al.*[57] using a linear stability theory. The dispersion relationship depicting the growth rate for a given wave number was reported and compared for different power-law fluids. The study established that growth rate of the instability decreases as the fluid becomes more shear thinning in nature, whereas it increases for more shear thickening fluids.

2.2.2 Flow of Suspensions

In recent years, several studies have been carried out on particle-laden thin film flows on an inclined plane geometry owing to its applicability in diverse contexts.[64–70] In general, the flow of suspensions is similar to that of pure liquids, which allows the flow to be modeled using Navier-Stokes equation just by replacing the viscosity of the liquid by appropriate constitutive relation accounting for the non-Newtonian nature of the fluid. Lubrication theory is also used in modeling these flows due to thinness of the film.

Timberlake and Morris[71] measured the velocity and concentration profiles in such flow of a concentrated suspensions down an inclined plane for various inclinations and concentrations. The data was successfully compared with the predictions of a particle-migration model. They observed that the free surface became more deformed with increasing concentration or inclination.

Fingering instability at the contact line of a yield stress clay suspension flowing down an inclined plane was studied by de Bruyn *et al.*[72]. They derived an expression for the wavelength of the instability for a Herschel-Bulkley fluid. Their experimental data using clay suspensions agreed well with their theoretical predictions.

Zhou *et al.*[64] carried out experimental as well as theoretical study to explain the emergence of particle-rich ridge on an inclined plane flow of particle-laden film. The particle volume fraction (ϕ_p) and inclination angle (α) were varied over a wide range and three distinct regimes were observed. When ϕ_p and α are small, settled regime results. For larger ϕ_p and α the ridged regime occurs and finally for intermediate values of the above quantities, the suspension remains well-mixed and fingering in-

stability occurs. The authors have found that the ridge formation occurs due to two shocks arising from differential transport rates of fluid and particles. Their study was focused on the ridged regime. Moreover, it was observed that finger formation was somewhat suppressed in the experiment by the formation of the particle-rich ridge suppressing the advancing contact line with respect to the transverse perturbations. However, they have not addressed anything about the fingering instability.

Tabuteau *et al.*[73] studied the spreading of a yield stress fluid on a spinning disc both experimentally and theoretically. They calculated the critical angular velocity for the yielding of the material for varying geometrical conditions of the drop. The effect of angular acceleration, yield stress, and substrate roughness on the drop spreading was also investigated experimentally. Although, the work mainly deals with spreading, finger formation was also observed in their work at high enough angular velocity.

Balmforth *et al.*[74] investigated the fingering instability in a thin layer viscoplastic fluid flowing down an inclined plane. The authors derived the governing equations for the flow including the effect of surface tension and yield stress using lubrication theory. A linear stability analysis of the base state solution was carried out to model finger growth to understand the effect of yield stress. The instability wave number (q) corresponds to the instability wavelength ($\lambda = 2\pi/q$) and refers to actual number of fingers observed in experiments. It was found to decrease with the increase in concentration of suspension which was in qualitative agreement with their analytical results, when the concentration corresponds to the yield stress.

Ward *et al.*[65] carried out experiments with particle concentrations ranging from 35 to 55%. Various input parameters (particle size, fluid viscosity, initial volume, plane inclination) were varied. Among other variables, they measured the evolution of the front position $x_f(t)$. They showed that, even though departures from the $x_f \propto t^{1/3}$ theoretical trend were observed, this scaling was the correct approximation at long times. This trend was also reported by Huppert[58] for a clear liquid flowing down an inclined plane.

Cook *et al.*[75] performed a linear stability analysis of particle-laden thin-film flows

on an inclined plane and their study demonstrated that the particle settling moderately reduces the growth rate of unstable modes, while increasing the most unstable wavelength.

Grunewald *et al.*[76] explained the self-similarity occurring in case of constant volume inclined plane flow based on lubrication model. Their major focus was on the effect of precursor layer thickness on the model prediction. The front position in this case agreed to the $t^{1/3}$ scaling law.

Recently, Murisic *et al.*[66] studied the particle-laden thin-film flow on an inclined plane. They have performed experiments for a range of particle volume fraction and fluid viscosity. The authors have studied the effect of particle volume fraction and inclination angle on the flow and found that viscosity affects the time scale on which particles settle or remain well-mixed. In another study by these authors,[67] they have studied the settled regime experimentally and observed that particle settle due to gravity and shear-induced migration helps in particle re-suspension. The theoretical model agreed well with their experimental data.

In a very recent study by Ancey *et al.*[68] on neutrally buoyant non-colloidal suspensions, they have simultaneously measured the local properties far from side wall as well as macroscopic flow features like front position and flow depth profile. For 45% suspension, flow behavior does not differ much from pure Newtonian case. For $52 - 56\%$ particle volume fraction the flow depth and front position were fairly well predicted by lubrication theory. For volume fraction $> 56\%$ the flow reached a steady state.

2.3 Gaps in the Existing Literature

As discussed above, the existing literature on spin disc flow has focused almost exclusively on the spreading and instability of a single Newtonian viscous liquid with a free surface. Recently, film spreading in case of two-layer coating flows has been explored, which endeavors to study film thinning behavior and interfacial instability between the two layers, which are assumed to be infinite in extent. Moreover, exper-

imental studies on two-layer spin coating flow does not exist. In fact, there exist no theoretical/experimental study which focuses on the contact line instability in case of two-layer spin coating flow. Also, experimental/theoretical studies on particle-laden flow of thin films are primarily restricted to inclined plane geometry, where the suspending medium used is a fully wetting liquid. Therefore, deciphering the mechanism behind the contact line instability in above-mentioned systems, to address the above gaps in the existing spin coating literature sets the stage for this thesis work. The contribution of this thesis and the objectives of this study are presented below.

2.4 Objective of the Thesis

The overall objective of the thesis is to investigate:

1. the spreading behavior and contact line instability in case of a liquid spreading in presence of another liquid on top, and to compare with that of a single fluid spreading with a free air-liquid interface by performing experiments.

2. the effect of physical properties of liquids and other process parameters on film thickness and contact line evolution, and the shape of the capillary ridge in the above case using numerical simulation.

3. the effect of presence of particles on the overall spreading dynamics and contact line instability using experiments.

2.5 Contribution of this Thesis

In this work, we seek to study the spreading and instability behavior of a liquid by perturbing the contact line from both inside and outside. This can be achieved in the following two ways: (1) by adding another liquid on the outside, (2) by adding particles (solid phase) in the liquid. The latter case refers to the spreading of a suspension. This work is significant not only from a fundamental perspective, but

also due to its applications, viz., in multi-layer coating (thin film of co-flowing fluids) and micro-encapsulation processes (flow of suspensions).

Chapter 3

Numerical Simulation of Axisymmetic Two-layer spin coating flow of Newtonian liquids

3.1 Introduction

In recent years, materials having a multi-layered coating have gained considerable attraction because of their gamut of applications. For example, multi-layer coatings are used to make CDs, DVDs, optical mirrors, semiconductors and biodegradable polymeric films. One of the applications in electronic industry is to fabricate organic solar cells using a bi-layer coating[77]. Depending upon the application, multi-layer films can have thicknesses ranging from nanometers scale as for Langmuir films[78] to several microns as for semiconductors. These layers can be of common liquids such as oil or water, or can be of complex materials such as polymer melts or suspensions. Each of the layers provide a unique functionality to the material which enhances its properties and transforms it into an advanced material. For example, coatings of mono-nitride and mono-carbide are applied on numerous materials to improve the mechanical strength and corrosion behavior, respectively.

In the multi-layer spin coating process, two or more liquids are placed on one

another on a rotating disc, which spread and thin to form a multi-layer film of finite thickness. Spin coating process for depositing a single-layer of material on a flat substrate has been studied widely in the past through several experimental and theoretical studies which have been reviewed in detail in Chapter 2. Unlike the single-layer coating, spin coating process for depositing multiple layers of liquid on a flat substrate has received lesser attention in the literature. Two-layer film flow on a rotating disk was first studied theoretically by Sisoev and Shkadov[79]. Recently, McIntyre and Brush[48] used lubrication theory to investigate the spin coating flow of two immiscible vertically stratified Newtonian thin films. Their study focused on examining the interfacial instabilities associated with the liquid-air and liquid-liquid interfaces present in the thin two-layered film. In their investigation, effects of viscous forces and condensation/evaporation of the upper layer was considered to study the spreading and thinning of the film. It was observed that the disturbances in any of the layer thicknesses affect the uniformity of the other, however, the disturbances to the lower layer thickness have greater effect on the upper layer thickness as compared to vice-versa. More recently, Dandapat and Singh[49] have established the role played by viscosity, initial film thickness and density ratio (of the layered fluids) on final film thickness for large Reynolds number at long times. In a recent article by Dandapat and Singh[50], they have analytically presented long-time solution for an unsteady two-layer liquid film flow on a horizontal rotating disk, and explained the findings physically for small Reynolds number. It was observed that the final film thickness attains an asymptotic value after a long time duration. They have also established that viscous force dominates over centrifugal force and upper layer thins faster than lower layer at long times.

Similar to the single-layer spin coating process, in two-layer spin coating process each of the fluid layers spread to form thin flat film at the center and a capillary ridge at the respective outer boundary. The formation of multiple capillary ridges affects the uniformity of the final film and can lead to significant loss of the coating liquids. The uniformity of the film depend upon numerous process parameters such as disc rotation speed and initial volume of each fluid. Furthermore, ratios of the physical

properties of the layered fluids significantly affect the evolution of film profiles. All the studies for two-layer spin coating process reported so far examined the effect of interfacial instabilities on the final film profile. However, the effect of surface tension on the uniformity of the film and the formation of capillary ridges has not been studied yet.

This chapter reports a numerical study on axisymmetric two-layer thin film flow on a spinning disc. The focus is on the formation of capillary ridges close to the two contact lines. The axisymmetric (1D) model equations governing the two-layer spin coating flow are simplified using lubrication approximation. Precursor-layer model is used to relive the singularity of the contact line. A Galerkin finite element method (G/FEM) based approach is used to solve the equations numerically. The effect of various fluid property ratios such as viscosity ratio, surface to interfacial tension ratio and process parameters like volume ratios of fluids present in both the layers and ratio of precursor layer thicknesses are studied.

3.2 Axisymmetric Model

This section describes the formulation of the governing equations describing the axisymmetric flow of two-layer thin film on a rotating disc. The axisymmetric model of spin coating flow assumes that the height of the free surface varies only with the radial distance r and is independent of the transverse direction.

3.2.1 Mathematical Formulation

The system under consideration consists of two incompressible and immiscible Newtonian fluids; fluid I having density $\tilde{\rho}_1$, surface tension $\tilde{\sigma}_1$, and dynamic viscosity $\tilde{\eta}_1$, and fluid II having density $\tilde{\rho}_2$, surface tension $\tilde{\sigma}_2$, and dynamic viscosity $\tilde{\eta}_2$, respectively. The layer of fluid II is placed on the layer of fluid I and both are placed on a disc which is rotating with a constant angular velocity $\tilde{\omega}$ as shown in Fig. 3.1. The layer of fluid II is surrounded by air which is at a constant ambient pressure but exerts no shear stress on the fluid-air interface. Throughout this chapter, the dimensional

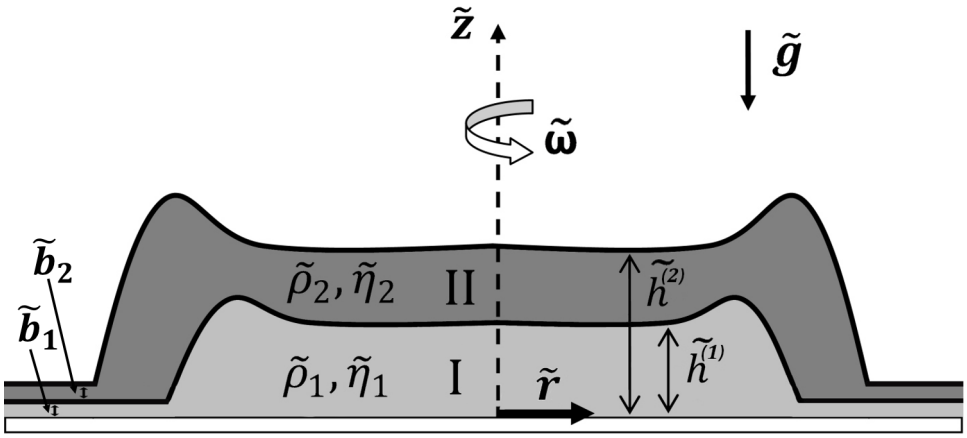

Figure 3.1: Schematic illustration of two-layer thin-film flow on a spinning disc. Dimensional notations are used. The precursor layer thicknesses are greatly exaggerated.

variables have tilde, $\tilde{(.)}$, over them whereas the corresponding dimensionless variables are denoted without tilde, (.) and vector quantities are represented in bold italics. Hereafter, the layer of fluid present in fluid II is referred to as upper layer, and fluid I is referred to as lower layer. For mathematical convenience, we use the cylindrical coordinate system $(\tilde{r}, \tilde{\theta}, \tilde{z})$ as shown in the Fig. 3.1. Since the flow is axisymmetric, at any point along the radial direction, the shape of the liquid-liquid interface and the liquid-air interface are denoted by $\tilde{z} = \tilde{h}^{(1)}(\tilde{r}, \tilde{t})$, and $\tilde{z} = \tilde{h}^{(2)}(\tilde{r}, \tilde{t})$, respectively [see Fig. 3.1]. The isothermal flow of fluid in each of the layers is governed by Navier-Stokes equation and continuity equation:

$$\tilde{\rho_i}\left(\frac{\partial \tilde{\boldsymbol{u}}^{(i)}}{\partial \tilde{t}} + \tilde{\boldsymbol{u}}^{(i)}.\tilde{\nabla}\tilde{\boldsymbol{u}}^{(i)}\right) = -\tilde{\nabla}\tilde{P}^{(i)} + \tilde{\eta_i}\tilde{\nabla}^2\tilde{\boldsymbol{u}}^{(i)} - \tilde{\rho_i}[2\tilde{\boldsymbol{\omega}} \times \tilde{\boldsymbol{u}}^{(i)} + \tilde{\boldsymbol{\omega}} \times (\tilde{\boldsymbol{\omega}} \times \tilde{\boldsymbol{r}}) + \tilde{\boldsymbol{g}}], \tag{3.1}$$

$$\tilde{\nabla} \cdot \tilde{\boldsymbol{u}}^{(i)} = 0, \tag{3.2}$$

where $\tilde{\boldsymbol{u}}^{(i)} = (\tilde{u}^{(i)}, 0, \tilde{v}^{(i)})$ is the velocity of the fluid in the i^{th} layer, $\tilde{\boldsymbol{\omega}}$ is the angular velocity and $\tilde{\boldsymbol{g}}$ is the gravity vector pointing downwards as shown in the Fig. 3.1. On the right hand side of Eq. (3.1), the third term represents the Coriolis force and the fourth term represents the centrifugal force. Equations (3.1) and (3.2) are

non-dimensionalized with appropriate scales as follows: disc radius, R_0 is the length scale in the radial direction; initial mean film thickness, H_0 is the length scale in the vertical direction; U_0 is the velocity scale in the radial direction; V_0 is the velocity scale in the vertical direction, and P_0 is the scale for pressure. The scale for density and viscosity are ρ_0 and η_0, respectively, which for convenience are taken to be the parameters of one of the layer fluids. Since, the flow is axisymmetric, the terms in the radial-direction momentum balance equation that involve azimuthal velocity are negligible [55]. Moreover, the momentum balance equation in azimuthal direction is neglected. The non-dimensional form of the equations (3.1) and (3.2) in the relevant directions are:

$$\epsilon \cdot Re\left(\frac{\partial u^{(i)}}{\partial t} + u^{(i)} \cdot \nabla u^{(i)}\right) = -\frac{\partial P^{(i)}}{\partial r} + \epsilon^2 \eta_i \frac{\partial}{\partial r}\left[\frac{1}{r}\frac{\partial (ru)}{\partial r}\right] + \eta_i \frac{\partial^2 u^{(i)}}{\partial z^2} + r, \tag{3.3}$$

$$\begin{aligned}\epsilon^3 \cdot Re\left(\frac{\partial v^{(i)}}{\partial t} + u^{(i)} \cdot \nabla v^{(i)}\right) = &-\frac{\partial P^{(i)}}{\partial z} + \epsilon^2 \eta_i \frac{\partial^2 v^{(i)}}{\partial z^2} \\ &+ \epsilon^4 \eta_i \left[\frac{1}{r}\frac{\partial}{\partial r}\left(r\frac{\partial v}{\partial r}\right)\right] - B + O(\epsilon^2),\end{aligned} \tag{3.4}$$

$$\frac{1}{r}\frac{\partial (ru^{(i)})}{\partial r} + \frac{\partial v^{(i)}}{\partial z} = 0, \tag{3.5}$$

where $\eta_i = \tilde{\eta}_i/\eta_0$, and $\rho_i = \tilde{\rho}_i/\rho_0$ are the dimensionless viscosity and density, respectively. The velocities in the radial and vertical directions are $\tilde{u}^{(i)}$ and $\tilde{v}^{(i)}$, respectively. $Re = \rho_0 U_0 H_0/\eta_0$ is the Reynolds number, $B = \rho_0 g H_0^3/\eta_0 R_0 U_0$ is the Bond number, and $\epsilon = H_0/R_0$ is the aspect ratio. In each of the layers, flow is governed by the balance between the centrifugal force and the viscous force that gives the radial velocity scale as $U_0 = \rho_0 \omega^2 R_0 H_0^2/\eta_0$, and the vertical velocity scale as $V_0 = U_0 H_0/R_0$. Here, $\nabla = R_0.\tilde{\nabla}$ is the dimensionless gradient operator. The pressure scale is $P_0 = \rho_0 \omega^2 R_0^2$, and the time scale is $T = R_0/U_0$.

The Reynolds number associated with the flow is assumed to be very small so that inertial effects are negligible. It has been shown previously [27] that coriolis force drives

the flow in azimuthal direction and is negligible for the axisymmetric flow considered here. Moreover, we assume that the film height is small and the gravitational effects are negligible ($B \approx 0$). The spreading film is sufficiently thin that allows use of the standard lubrication assumptions: $\epsilon \ll 1$ and $Re.\epsilon \ll 1$. A more general discussion on the lubrication theory for n-layer thin film flow with applications to multilayer coating can be found in Anturkar *et al.* and Renardy [80,81]. Using lubrication assumption, Eqs. (3.3)-(3.5) are simplified as:

$$0 = -\frac{\partial P^{(i)}}{\partial r} + \eta_i \frac{\partial^2 u^{(i)}}{\partial z^2} + r, \tag{3.6}$$

$$0 = -\frac{\partial P^{(i)}}{\partial z} - B, \tag{3.7}$$

$$0 = \frac{1}{r}\frac{\partial (r u^{(i)})}{\partial r} + \frac{\partial v^{(i)}}{\partial z}. \tag{3.8}$$

These equations are subjected to the following boundary conditions:

$$u^{(1)} = 0 \quad \text{at } z = 0, \tag{3.9}$$

$$u^{(1)} = u^{(2)} \quad \text{at } z = h^{(1)}(r,t), \tag{3.10}$$

$$\eta_1 \frac{\partial u^{(1)}}{\partial z} = \eta_2 \frac{\partial u^{(2)}}{\partial z} \quad \text{at } z = h^{(1)}(r,t), \tag{3.11}$$

$$\frac{\partial u^{(2)}}{\partial z} = 0 \quad \text{at } z = h^{(2)}(r,t), \tag{3.12}$$

$$P^{(1)} = p_0 - C_1 \nabla^2 h^{(1)} - C_2 \nabla^2 h^{(2)} \quad \text{at } z = h^{(1)}(r,t), \tag{3.13}$$

$$P^{(2)} = p_0 - C_2 \nabla^2 h^{(2)} \quad \text{at } z = h^{(2)}(r,t), \tag{3.14}$$

where $C_i = \epsilon^3 \sigma_i / \eta_0 U_0$ is the inverse Capillary number, p_0 is the atmospheric pressure, and $\nabla^2 = \frac{1}{r}\frac{\partial}{\partial r}(r\frac{\partial}{\partial r})$. Equation (3.9) represents the no-slip condition at the planar substrate. Equations (3.10) and (3.11) represent the continuity of velocity and tangential stress at liquid-liquid interface, respectively. Equation (3.12) represents the zero tangential stress at the liquid-air interface, and Eqs. (3.13) and (3.14) represent the normal stress condition that incorporates the surface tension force at the

respective surface.

From here on wards, the scales $\rho_0 = \rho_1$, and $\eta_0 = \eta_1$ are chosen to be the properties of the lower layer fluid. The radial velocities $u^{(1)}$ and $u^{(2)}$ are obtained by integrating Eqs. (3.6) and (3.7) for both the layers and applying boundary conditions given by Eqs.(3.9)-(3.14).

$$\begin{aligned} u^{(1)} =& -\left(\hat{\sigma}C\frac{\partial}{\partial r}(\nabla^2 h^{(2)}) + C\frac{\partial}{\partial r}(\nabla^2 h^{(1)}) + r\right)\frac{z^2}{2} \\ &+ \left(C\frac{\partial}{\partial r}(\nabla^2 h^{(1)}) + (1-\hat{\rho})r\right)zh^{(1)} + \left(\hat{\sigma}C\frac{\partial}{\partial r}(\nabla^2 h^{(2)}) + \hat{\rho}r\right)zh^{(2)}, \end{aligned} \tag{3.15}$$

$$\begin{aligned} u^{(2)} =& -\left(\frac{\hat{\sigma}}{\hat{\eta}}C\frac{\partial}{\partial r}(\nabla^2 h^{(2)}) + \frac{\hat{\rho}}{\hat{\eta}}r\right)\left[\frac{z^2}{2} - zh^{(2)}\right] \\ &+ \left(\hat{\sigma}C\frac{\partial}{\partial r}(\nabla^2 h^{(2)}) + C\frac{\partial}{\partial r}(\nabla^2 h^{(1)}) + r + \left[\hat{\sigma}C\frac{\partial}{\partial r}(\nabla^2 h^{(2)}) + \hat{\rho}r\right]\left[2 - \frac{1}{\hat{\eta}}\right]\right)\frac{{h^{(1)}}^2}{2} \\ &+ \left(\frac{\hat{\sigma}}{\hat{\eta}}C\frac{\partial}{\partial r}(\nabla^2 h^{(2)}) + \frac{\hat{\rho}}{\hat{\eta}}r\right)(\hat{\eta}-1)h^{(1)}h^{(2)}, \end{aligned} \tag{3.16}$$

where $\hat{\sigma} = \sigma_2/\sigma_1$, $\hat{\eta} = \eta_2/\eta_1$, $\hat{\rho} = \rho_2/\rho_1$ and $C = \epsilon^3\sigma_1/\eta_1 U_1$. Integrating the continuity equation Eq. (3.8) for both the layers and using the kinematic condition gives the usual mass balance as

$$\frac{\partial h^{(1)}}{\partial t} + \frac{1}{r}\frac{\partial (rQ^{(1)})}{\partial r} = 0\ , \tag{3.17}$$

$$\frac{\partial h^{(2)}}{\partial t} + \frac{1}{r}\frac{\partial (r[Q^{(1)} + Q^{(2)}])}{\partial r} = 0\ , \tag{3.18}$$

where

$$Q^{(1)} = \int_0^{h^{(1)}} u^{(1)}dz \quad \text{and} \quad Q^{(2)} = \int_{h^{(1)}}^{h^{(2)}} u^{(2)}dz\ . \tag{3.19}$$

The quantities $Q^{(1)}$ and $Q^{(2)}$ are the fluxes in radial direction across the layer of fluid I and fluid II respectively. Using Eq. (3.15) and Eq. (3.16), the fluxes $Q^{(1)}$ and $Q^{(2)}$ are obtained as

$$Q^{(1)} = \left(\hat{\sigma}C\frac{\partial}{\partial r}(\nabla^2 h^{(2)}) + C\frac{\partial}{\partial r}(\nabla^2 h^{(1)}) + r\right)\frac{{h^{(1)}}^3}{3} + \left(\hat{\sigma}C\frac{\partial}{\partial r}(\nabla^2 h^{(2)}) + \hat{\rho}r\right)\frac{{h^{(1)}}^2}{2}(h^{(2)} - h^{(1)}), \tag{3.20}$$

$$Q^{(2)} = \left(\hat{\sigma}C\frac{\partial}{\partial r}(\nabla^2 h^{(2)}) + \hat{\rho}r\right)\left[\frac{\left(h^{(2)} - h^{(1)}\right)^3}{3\hat{\eta}} + h^{(1)}(h^{(2)} - h^{(1)})^2\right] + \left(\hat{\sigma}C\frac{\partial}{\partial r}(\nabla^2 h^{(2)}) + C\frac{\partial}{\partial r}(\nabla^2 h^{(1)}) + r\right)\frac{{h^{(1)}}^2}{2}(h^{(2)} - h^{(1)}). \tag{3.21}$$

Substituting the value of $Q^{(1)}$ and $Q^{(2)}$ in Eq. (3.17) and (3.18), the two equations describing the evolution of internal surface and free surface, respectively are obtained as

$$\frac{\partial h^{(1)}}{\partial t} + \frac{1}{r}\frac{\partial}{\partial r}\left[r\left\{\left(\hat{\sigma}C\frac{\partial}{\partial r}(\nabla^2 h^{(2)}) + C\frac{\partial}{\partial r}(\nabla^2 h^{(1)}) + r\right)\frac{{h^{(1)}}^3}{3} + \left(\hat{\sigma}C\frac{\partial}{\partial r}(\nabla^2 h^{(2)}) + \hat{\rho}r\right)\frac{{h^{(1)}}^2}{2}(h^{(2)} - h^{(1)})\right\}\right] = 0, \tag{3.22}$$

$$\frac{\partial h^{(2)}}{\partial t} + \frac{1}{r}\frac{\partial}{\partial r}\left[r\left\{\left(\hat{\sigma}C\frac{\partial}{\partial r}(\nabla^2 h^{(2)}) + \hat{\rho}r\right)\left[\frac{\left(h^{(2)} - h^{(1)}\right)^3}{3\hat{\eta}} + h^{(1)}(h^{(2)} - h^{(1)})\left(h^{(2)} - \frac{h^{(1)}}{2}\right)\right] + \left(\hat{\sigma}C\frac{\partial}{\partial r}(\nabla^2 h^{(2)}) + C\frac{\partial}{\partial r}(\nabla^2 h^{(1)}) + r\right)\frac{{h^{(1)}}^2}{2}\left(h^{(2)} - \frac{h^{(1)}}{3}\right)\right\}\right] = 0. \tag{3.23}$$

Now, defining $\hat{h}_1 = h^{(1)}$ and $\hat{h}_2 = h^{(2)} - h^{(1)}$, so that $\hat{h}_i$ represents the thickness of the i^{th} layer, the two equations describing the time evolution of the thicknesses of the two layers with respect to spatial coordinate r are obtained as

$$\frac{\partial \hat{h}_1}{\partial t} + \frac{1}{r}\frac{\partial}{\partial r}\left[r\left\{\frac{\hat{h}_1^3}{3}\left(\hat{\sigma}C\frac{\partial}{\partial r}(\nabla^2[\hat{h}_1 + \hat{h}_2]) + C\frac{\partial}{\partial r}(\nabla^2 \hat{h}_1) + r\right)\right.\right.$$

$$+\left(\hat{\sigma}C\frac{\partial}{\partial r}(\nabla^2[\hat{h}_1+\hat{h}_2])+\hat{\rho}r\right)\frac{\hat{h}_1^2\hat{h}_2}{2}\Bigg\}\Bigg]=0, \tag{3.24}$$

$$\frac{\partial\hat{h}_2}{\partial t}+\frac{1}{r}\frac{\partial}{\partial r}\Bigg[r\Bigg\{\frac{\hat{h}_1^2\hat{h}_2}{2}\left(\hat{\sigma}C\frac{\partial}{\partial r}(\nabla^2[\hat{h}_1+\hat{h}_2])+C\frac{\partial}{\partial r}(\nabla^2\hat{h}_1)+r\right)$$
$$+\left(\hat{\sigma}C\frac{\partial}{\partial r}(\nabla^2[\hat{h}_1+\hat{h}_2])+\hat{\rho}r\right)\left(\frac{\hat{h}_2^3}{3\hat{\eta}}+\hat{h}_1\hat{h}_2^2\right)\Bigg\}\Bigg]=0. \tag{3.25}$$

Equation (3.24) determines the film thickness $\hat{h}_1(r,t)$ of the lower layer while Eq. (3.25) determines the film thickness $\hat{h}_2(r,t)$ of the upper layer. Both the governing equations are fourth order non-linear PDEs which are subjected to the following initial and boundary conditions:

$$\hat{h}_1=\hat{h}_{10}(r)\quad\text{and}\quad\hat{h}_2=\hat{h}_{20}(r)\quad\text{at } t=0, \tag{3.26}$$

$$\hat{h}_{1r}=0\quad\text{and}\quad\hat{h}_{2r}=0\quad\text{at } r=0, \tag{3.27}$$

$$\hat{h}_{1rrr}=0\quad\text{and}\quad\hat{h}_{2rrr}=0\quad\text{at } r=0, \tag{3.28}$$

$$\hat{h}_1=b_1\quad\text{at } r=R_1(t)\text{ and}\quad\hat{h}_2=b_2\quad\text{at } r=R_2(t), \tag{3.29}$$

$$\hat{h}_{1r}=0\quad\text{at } r=R_1(t)\text{ and}\quad\hat{h}_{2r}=0\quad\text{at } r=R_2(t). \tag{3.30}$$

Equation (3.26) represents the initial conditions, i.e., the surface profiles $\hat{h}_{10}(r)$, and $\hat{h}_{20}(r)$ at $t=0$ are known. Equation (3.27) maintains the uniformity of the film at the center and Eq. (3.28) ensures that no flux is added to the system at that point. Equation (3.29) represents that the films $\hat{h}_1(r)$, and $\hat{h}_2(r)$ touch the precursor layer of height b_1 and b_2, respectively. Here, $R_1(t)$ and $R_2(t)$ are the contact radius for the lower and upper layer, respectively. Equation (3.30) enforces that the film thicknesses touch the respective precursor layer by decaying the derivatives at that point. A similar derivation but taking into account the additional effect of van der Waals force and evaporation/condensation can be found in McIntyre and Brush[48].

3.2.2 Numerical Method

The governing equations [see Eq. (3.24) and Eq. (3.25)] are solved numerically by a method of lines that uses the Galerkin/finite element method (G/FEM)[82] for spatial discretization and an adaptive finite difference method for discretization in time[83]. In order to achieve high accuracy, quadratic basis functions $\phi^i(r)$ are used to approximate the unknowns $\hat{h}_1$, $\hat{h}_2$ and r. The unknowns are then expanded in terms of a series of basis functions $z(r,t) = \sum_{i=1}^{N} z_i(t)\phi^i(r)$, where $z = h$ or r with $z_i = \hat{h_i}$ or r_i as the corresponding nodal value that needs to be determined. The quantity N is the total number of nodes. Since quadratic basis elements are used, the total number of nodes is $N = 2NE + 1$, where NE is the number of elements in the system.

The numerical domain is defined as a line of length L that is divided into N segments of equal length initially. At each node in the domain, Galerkin weighted residuals are calculated by multiplying Eq. (3.24) and Eq. (3.25) by basis function $\phi^i(r)$ and integrating the resulting expressions over the numerical domain. Weighted residuals of third and fourth order derivatives are integrated by parts and simplified using the boundary conditions [see Eqs. (3.27) and (3.28)]. Consequently, the residual equations at the first and last nodes are discarded and replaced by the Dirichlet boundary conditions [see Eq. (3.30)].

3.2.2.1 Galerkin weighted residuals

The weighted residual equations for the four unknowns ($\hat{h}_1, \hat{h}_2, F$ and G) are:

$$R_1^i = \int_\Omega \phi^i \frac{\partial \hat{h}_1}{\partial t}\, d\Omega$$
$$- \int_\Omega \nabla\phi^i \cdot \left[\left(\frac{\hat{h}_1^3}{3}\right)\Big(\nabla F + \nabla G + r\Big) + \left(\frac{\hat{h}_1^2 \hat{h}_2}{2}\right)\Big(\nabla F + \rho r\Big)\right] d\Omega = 0, \qquad (3.31)$$

$$R_2^i = \int_\Omega \phi^i \frac{\partial \hat{h}_2}{\partial t}\, d\Omega$$

$$-\int_{\Omega} \nabla\phi^i \cdot \left[\left(\frac{\hat{h}_2^3}{3\eta} + \hat{h}_1\hat{h}_2^2\right)\left(\nabla F + \rho r\right) + \left(\frac{\hat{h}_1^2\hat{h}_2}{2}\right)\left(\nabla F + \nabla G + r\right)\right] d\Omega = 0, \tag{3.32}$$

$$R_F^i = \int_{\Omega} \phi^i F \, d\Omega + C\sigma \int_{\Omega} \nabla\phi^i \cdot \nabla\hat{h}_2 \, d\Omega = 0, \tag{3.33}$$

$$R_G^i = \int_{\Omega} \phi^i G \, d\Omega + C \int_{\Omega} \nabla\phi^i \cdot \nabla\hat{h}_1 \, d\Omega = 0. \tag{3.34}$$

where, Ω is the unknown computational domain, $F = C\sigma\nabla^2 h_2$, and $G = C\nabla^2 h_1$.

3.2.2.2 Time Integration

The Galerkin/finite element weighted residuals are a set of nonlinear time-dependent ordinary differential equations. The time derivatives appearing in the residuals are discretized at each time step using one of the two finite-difference methods: (1) backward-difference integrator and forward- difference predictor (BDI/FDP) which is a first-order accurate method, or (2) trapezoid-rule integrator and Adams-Bashforth predictor (TRI/ABP), which is a second-order accurate method.

Spinning disc flow is a type of time dependent free surface flow problem, where the boundary of the finite element mesh moves with time. This is accounted for by transforming the time derivative of any physical quantity (say, h) appearing the governing equation as:

$$\frac{\partial h}{\partial t} = \dot{h} - \dot{x} \cdot \nabla h \tag{3.35}$$

where, $\dot{h}$ is the time derivative in a fixed time frame and $\dot{x}$ is the mesh velocity. In the above equation, the time derivative of a physical quantity is obtained as:

$$\dot{h} = \frac{c_1}{\Delta t_n}\left(h_n - h_{n-1}\right) - c_2\dot{h}_{n-1} \tag{3.36}$$

where, c_1 and c_2 are constants, $c_1 = 1$ and $c_2 = 0$ in case of backward Euler corrector and $c_1 = 2$ and $c_2 = 1$ for trapezoidal rule corrector.

3.2.2.3 Solution Method

At every time step, the resulting system of $4N$ non-linear equations representing four unknowns $(\hat{h}_1, \hat{h}_{1rr}, \hat{h}_2, \hat{h}_{2rr})$ is solved using Newton's method with an analytically computed Jacobian.

Analytical Jacobians:

The Jacobians are calculated analytically for each of the residual equation with respect to the four unknowns are:

Jacobian of $\mathbf{R_1}$ residual:

$$\frac{\partial R_1^i}{\partial \hat{h}_1^j} = \int_\Omega \phi^i \phi^j \frac{c}{\Delta t}\, d\Omega$$
$$- \int_\Omega \nabla \phi^i \cdot \left[\phi^j \left(\hat{h}_1^2 \Big(\nabla F + \nabla G + r \Big) + \hat{h}_1 \hat{h}_2 \Big(\nabla F + \rho r \Big) \right) \right] d\Omega, \tag{3.37}$$

$$\frac{\partial R_1^i}{\partial \hat{h}_2^j} = - \int_\Omega \nabla \phi^i \cdot \left[\phi^j \frac{\hat{h}_1^2}{2} \Big(\nabla F + \rho r \Big) \right] d\Omega, \tag{3.38}$$

$$\frac{\partial R_1^i}{\partial F^j} = - \int_\Omega \nabla \phi^i \cdot \left[\nabla \phi^j \left(\frac{\hat{h}_1^3}{3} + \frac{\hat{h}_1^2 \hat{h}_2}{2} \right) \right] d\Omega, \tag{3.39}$$

$$\frac{\partial R_1^i}{\partial G^j} = - \int_\Omega \nabla \phi^i \cdot \left[\nabla \phi^j \frac{\hat{h}_1^3}{3} \right] d\Omega. \tag{3.40}$$

Jacobian of $\mathbf{R_2}$ residual:

$$\frac{\partial R_2^i}{\partial \hat{h}_1^j} = - \int_\Omega \nabla \phi^i \cdot \left[\phi^j \hat{h}_2^2 \Big(\nabla F + \rho r \Big) + \phi^j \hat{h}_1 \hat{h}_2 \Big(\nabla F + \nabla G + r \Big) \right] d\Omega, \tag{3.41}$$

$$\frac{\partial R_2^i}{\partial \hat{h}_2^j} = \int_\Omega \phi^i \phi^j \frac{c}{\Delta t}\, d\Omega$$
$$- \int_\Omega \nabla \phi^i \cdot \left[\phi^j \left(\left(\frac{\hat{h}_2^2}{\eta} + 2 \hat{h}_1 \hat{h}_2 \right) \Big(\nabla F + \rho r \Big) + \frac{\hat{h}_1^2}{2} \Big(\nabla F + \nabla G + r \Big) \right) \right] d\Omega, \tag{3.42}$$

$$\frac{\partial R_2^i}{\partial F^j} = -\int_\Omega \nabla\phi^i \cdot \nabla\phi^j \left[\left(\frac{\hat{h}_2^3}{3\eta} + \hat{h}_1\hat{h}_2^2 + \frac{\hat{h}_2\hat{h}_1^2}{2}\right)\right] d\Omega, \tag{3.43}$$

$$\frac{\partial R_2^i}{\partial G^j} = -\int_\Omega \nabla\phi^i \cdot \left[\nabla\phi^j \frac{\hat{h}_1^2\hat{h}_2}{2}\right] d\Omega. \tag{3.44}$$

Jacobian of $\mathbf{R_F}$ residual:

$$\frac{\partial R_F^i}{\partial \hat{h}_1^j} = 0, \tag{3.45}$$

$$\frac{\partial R_F^i}{\partial \hat{h}_2^j} = C\sigma \int_\Omega \nabla\phi^i \cdot \nabla\phi^j \, d\Omega, \tag{3.46}$$

$$\frac{\partial R_F^i}{\partial F^j} = \int_\Omega \phi^i\phi^j \, d\Omega, \tag{3.47}$$

$$\frac{\partial R_F^i}{\partial G^j} = 0. \tag{3.48}$$

Jacobian of $\mathbf{R_G}$ residual:

$$\frac{\partial R_G^i}{\partial \hat{h}_1^j} = C\int_\Omega \nabla\phi^i \cdot \nabla\phi^j \, d\Omega, \tag{3.49}$$

$$\frac{\partial R_G^i}{\partial \hat{h}_2^j} = 0, \tag{3.50}$$

$$\frac{\partial R_G^i}{\partial F^j} = 0, \tag{3.51}$$

$$\frac{\partial R_G^i}{\partial G^j} = \int_\Omega \phi^i\phi^j \, d\Omega. \tag{3.52}$$

Each Newton iteration involves finding the solution of the equation:

$$\mathbf{J}.\boldsymbol{\Delta}\mathbf{x} = -\mathbf{R} \tag{3.53}$$

where, $\mathbf{\Delta x}$ is the vector used to update the solution vector $(\mathbf{x} + \mathbf{\Delta x})$ at the end of each iteration. $\mathbf{J}$ is the Jacobian matrix $\mathbf{J_{ij}} = \frac{\partial \mathbf{R^j}}{\partial \mathbf{x^i}}$ which is obtained analytically. The updated $\mathbf{x}$ value is used to calculate the $\mathbf{J}$ and $\mathbf{R}$ for the next iteration. This process is repeated until the L^2-norm of both the vector of residuals $(\mathbf{R})$ and the updates $(\mathbf{\Delta x})$ fall below the specified input tolerance (i.e., 10^{-6}).

The correctness of the Jacobian is demonstrated by the quadratic convergence of Newton's method. This algorithm for computing the transient surface profiles is programmed in FORTRAN which uses Hood's[84,85] frontal solver with Walter's modification[86] to solve the large system of algebraic equations at each Newton's iteration, efficiently.

3.2.3 Grid Convergence Study

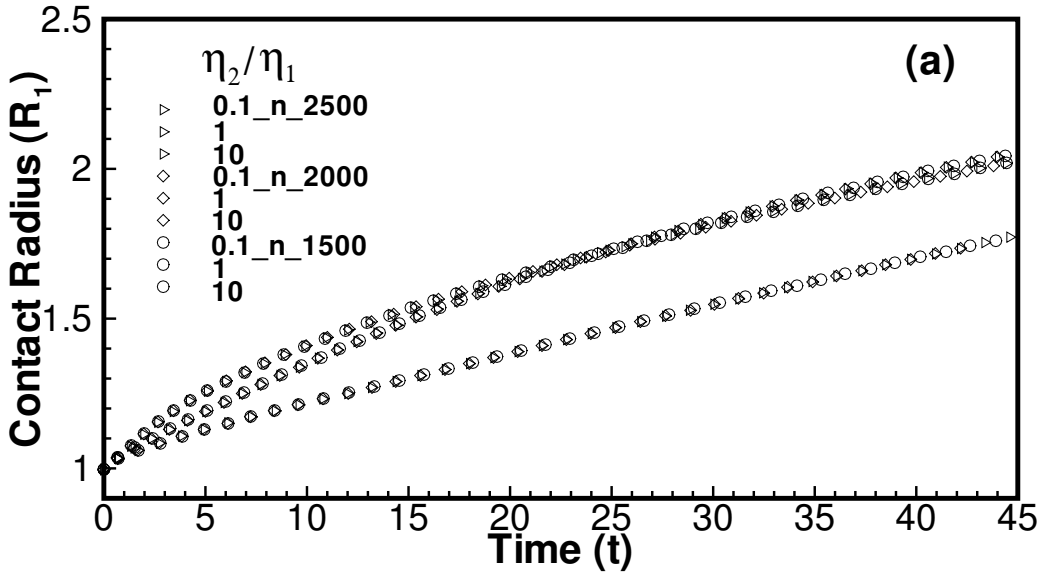

Figure 3.2: Grid convergence study showing the contact line evolution for the lower layer $(R_1(t))$ using three different number of elements $NE = 1500$, 2000 and 2500.

A grid convergence study was performed by running the numerical simulation for three different grid sizes i.e., for total number of elements as 1500, 2000 and 2500. The results for all the three cases are plotted in Fig. 3.2 and it shows that the curves for varying number of elements fall on top of each other and the relative error for the

time of crossover is ~ 0.02. This ensures that the results (observed crossovers) are independent of grid size (or number of elements), and are not any numerical artifacts.

3.2.4 Code Validation

The numerical scheme is validated for the single-layer spin coating process of Newtonian fluids with Wilson *et al.*[23] and for power law fluids with Charpin *et al.*[55]. The corresponding results for both the cases are presented in a previous work from our group[57]. The numerical procedure for the two-layer system considered here is validated with the results reported in McIntyre *et al.*[48]. The planar solution trajectories for the evolution of upper layer thickness, $h^{(2)} - h^{(1)}$, as a function of the lower layer thickness, $h^{(1)}$, reported by McIntyre and Brush[48] has been accurately reproduced in Fig. 3.3.

3.3 Results and Discussion

All the results reported in this section are obtained using a numerical procedure described in the previous section with 1500 equally spaced quadratic elements. If not mentioned, all the profiles are obtained using a density ratio $\rho_2/\rho_1 = 1$ and volume ratio $V_2/V_1 = 1$, where V_2 and V_1 are the volume of the fluid present in the upper and the lower layer, respectively. Appropriate values of dimensionless precursor layer thicknesses b_1 and b_2 are also specified. Results presented will include the effect of the fluid properties, and the process parameters on the the flow dynamics, uniformity of the layered films, and shape of capillary ridge for each layer. All the results are given in terms of dimensionless quantities.

3.3.1 Effect of initial condition

Fig. 3.4 illustrates the differences in the evolution of both the layers when subjected to different initial conditions. Each column corresponds to the spreading evolution for a particular initial condition while each row corresponds to the snapshots of spreading at

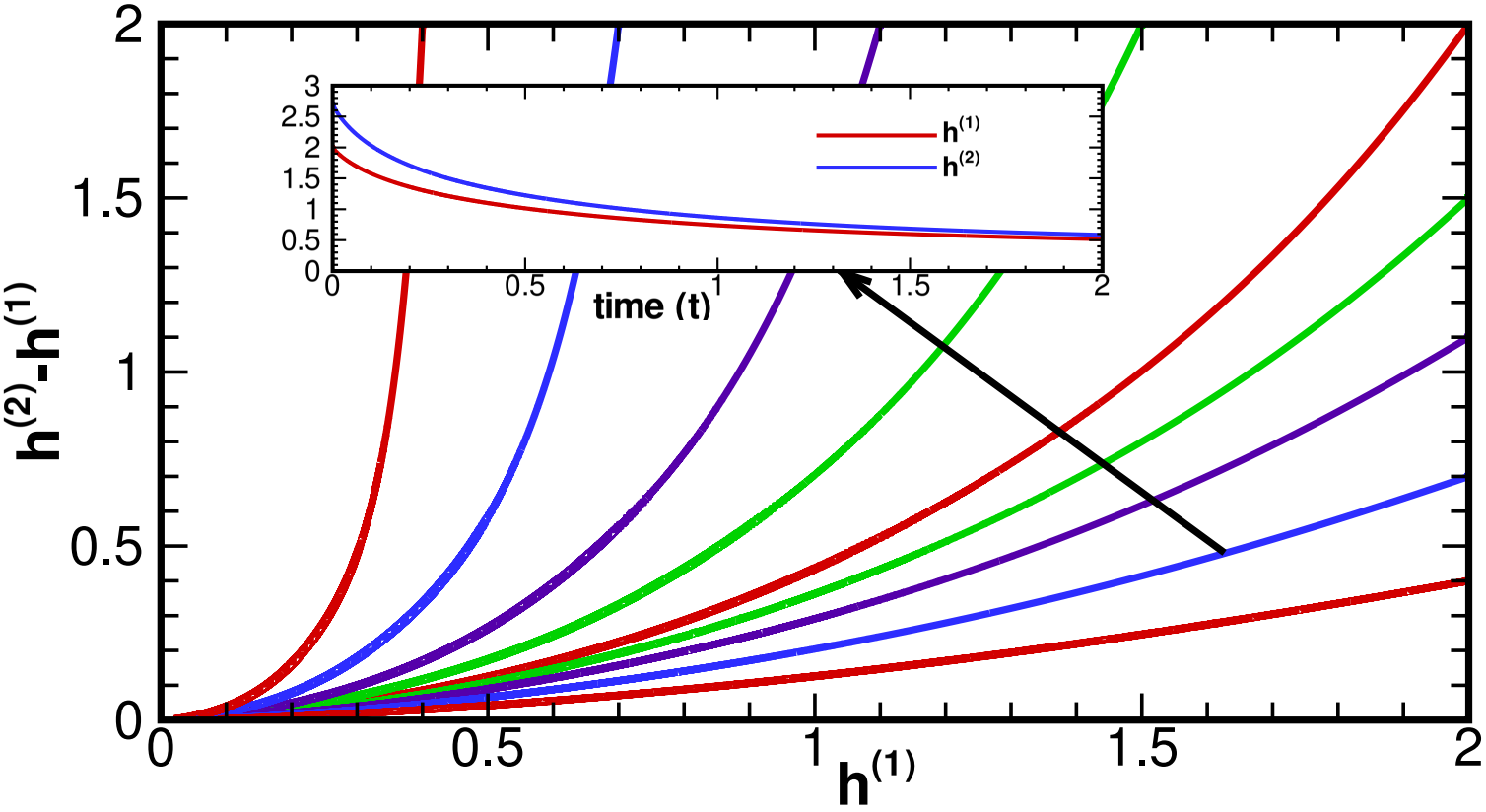

Figure 3.3: Validation of the numerical scheme by accurately reproducing the Fig. 2 of McIntyre *et al.*(J. Fluid Mech., 2010). Here, the planar solution trajectories are computed for $\eta_2/\eta_1 = 0.5$, $C = 2.7 \times 10^{-2}$ and $b_1 = b_2 = 0.01$, all the other fluid properties being same for both the layers.

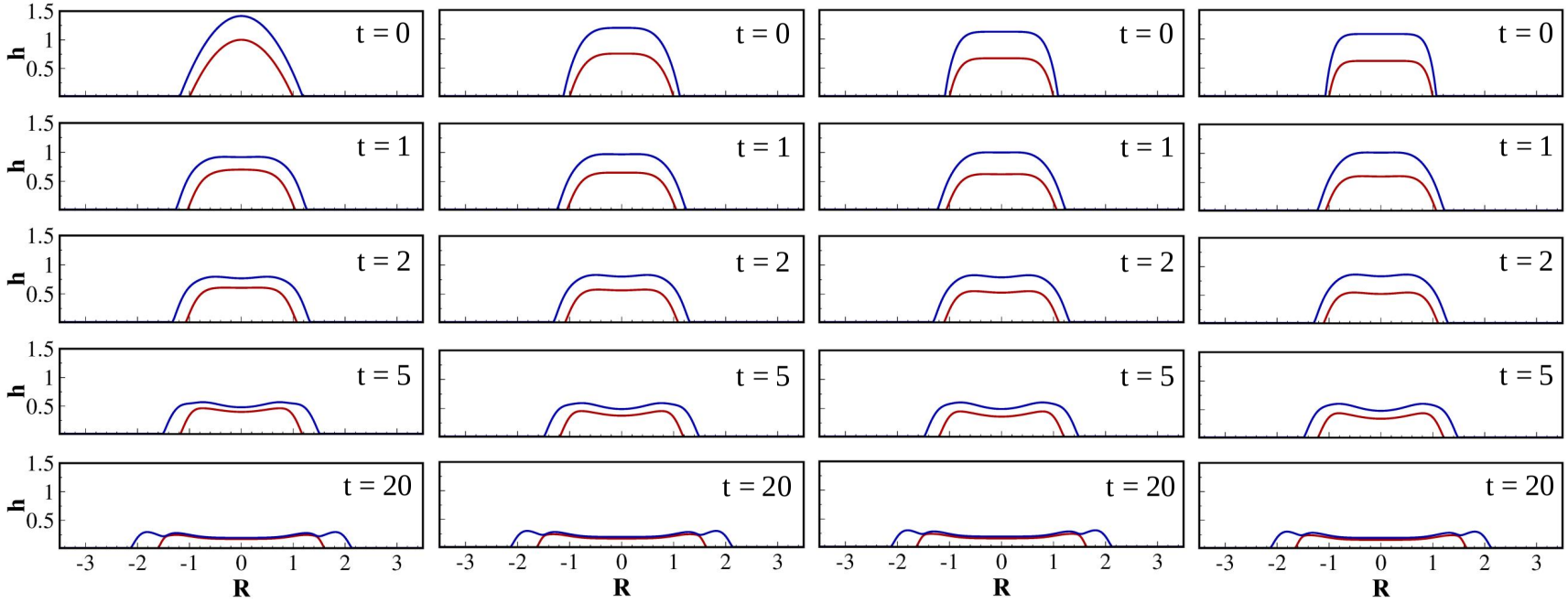

Figure 3.4: Snapshots of two-layer profiles with 4 different initial conditions, the shapes of which are provided in the text below. Each column represents the spreading evolution corresponding to a particular initial condition. Each row corresponds to the snapshots of spreading at a particular instant (embedded in each snapshot) during the spreading evolution. The profiles are computed for $C = 2.7\times10^{-2}$ and $b_1 = b_2 = 0.01$. Here, the fluids in both the layers have same physical properties.

a particular instant (embedded in each snapshot) during the spreading evolution. The initial shapes for both the drops are parabolic in column 1 and of the form $a(b-r^2)$. In column 2, 3, and 4, the shapes are of the form $a(b-r^4)$, $a(b-r^6)$ and $a(b-r^8)$, respectively. In order to compare the effect of initial condition on the evolution of both the layers, the volume of liquids in each of the layers are assumed to be the same as in column 1. The initial shapes (parameters a and b) are provided accordingly. The flatness of the initial shapes increases as we move towards right (column 2 to 4) (See row 1 of Fig. 3.4). Fig. 3.4 makes it plain that although the initial evolution looks slightly different for different initial conditions, the long time evolution (i.e., at $t = 20$) are pretty much the same for all cases considered here. Overall, it can be said that the initial shape of the layers affect the spreading for a very short initial period. However, the effect of initial shape plays a minor role in determining the spreading evolution and shape of the capillary ridges at long times. Hence, as reported in most of the previous studies on spinning disc flow,[23,28,32,55] in all the simulations reported in this chapter, parabolic drops are provided as initial shape for the two films. The shape of the parabola for the lower layer is: $\hat{h}_{10}(r) = 1 - r^2$, and for the upper layer is: $\hat{h}_{20}(r) = a - r^2 - \hat{h}_{10}(r)$, where $a = \sqrt{2}, \sqrt{3}$, and 2 for volume ratio $= 1, 2$ and 3, respectively.

3.3.2 Effect of viscosity ratio

3.3.2.1 Film thickness profiles

The effect of viscosity ratio on the time evolution of film profiles is explored by computing the profiles for three different values of the viscosity ratios, $\eta_2/\eta_1 = 0.1, 1,$ and 10, respectively. Figure 3.5 depicts the evolution of the film thickness profiles for the two layers separately for $0 \leq t \leq 100$. For all the three cases, the lower layer profiles are similar at long times ($t = 100$); i.e. flat, thin film at the center and capillary ridge at the periphery. However, their evolution is observed to be quite different. At $t = 15$, a comparison between the corresponding profiles in Figs. 3.5(a)-3.5(c) shows that the ridge becomes bulkier as the viscosity ratio increases. For

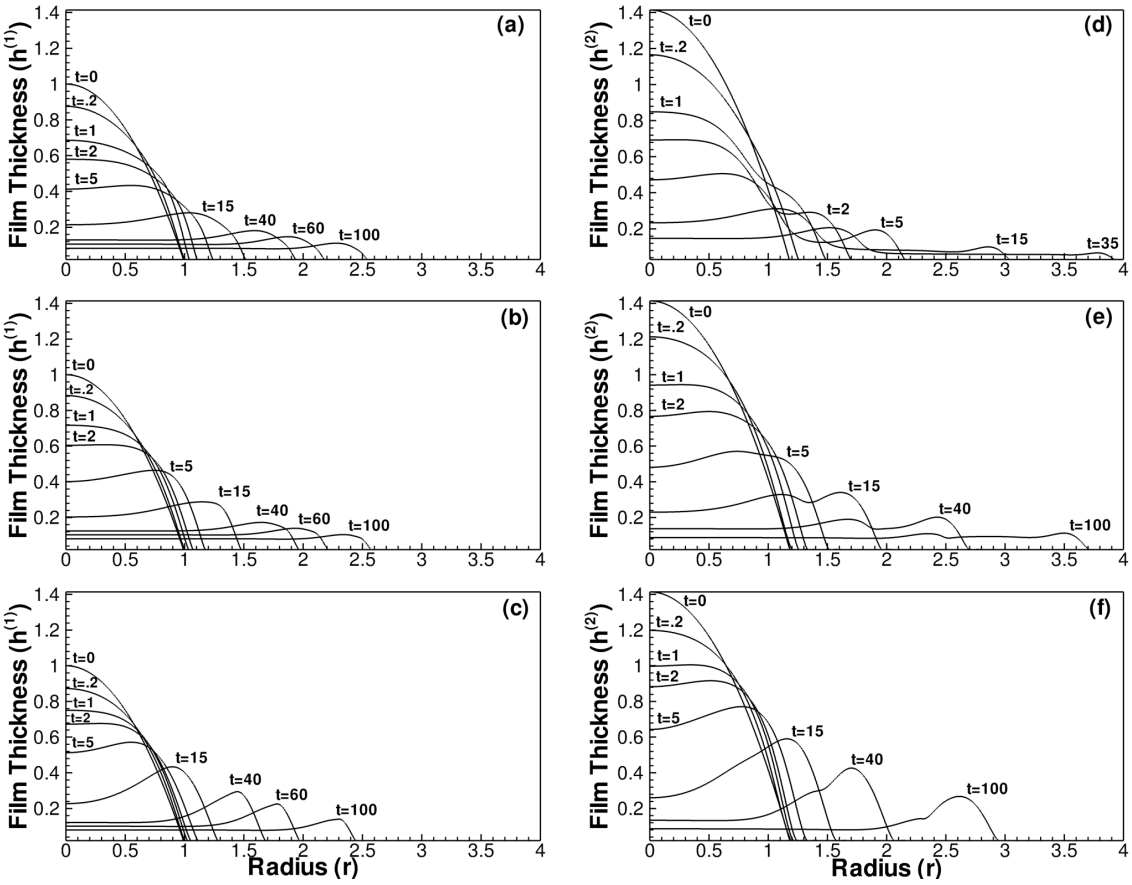

Figure 3.5: Film thickness profiles for three different viscosity ratios (a) 0.1, (b) 1, and (c) 10, for the lower layer (left) and upper layer (right). The profiles are computed for $\sigma_2/\sigma_1 = 1$, $C = 2.7 \times 10^{-2}$ and $b_1 = b_2 = 0.01$.

$\eta_2/\eta_1 = 10$, the viscous upper layer offers resistance to the flow of lower layer. Thus, the only way the fluid in the lower layer can flow is by pushing the liquid in the upper layer outwards, thereby forming a bulky capillary ridge.

Figures 3.5(d)-3.5(f) show the time evolution of the upper layer profiles for different viscosity ratios mentioned above. Similar to the lower layer, the upper layer profiles are also flat at the center, producing a thin film after a long time duration. However, the film evolution for the three cases proceeds in a different manner. For $\eta_2/\eta_1 = 0.1$ [see Fig. 3.5(d)], two distinct regions are clearly delineated. The upper layer fluid which resides on top of the lower layer is referred to as region A whereas the fluid residing beyond the inner contact line is referred to as region B. The dynamics of fluid in region A is primarily controlled by flow of fluid in the lower layer, resulting in slower rate of spreading and thinning. However, the fluid which resides in region B responds readily to the centrifugal force, resulting in faster spreading and thinning of the upper layer film in that region. The situation is reversed for $\eta_2/\eta_1 = 10$, as shown in Fig. 3.5(f). Here, the flow of fluid in the region A is still governed by the flow of fluid in the lower layer. But, most of the fluid flowing out from region A gets accumulated in region B. The lower layer fluid also flows outwards due to centrifugal force. However, the viscous fluid present in the region B is slow in its response to centrifugal force, thereby forming a bulky capillary ridge. From Figs. 3.5(d)-3.5(f), it is evident that the spreading of the upper layer decreases with the increase in viscosity ratio. Hence, ratio of the viscosity of two fluids has significant effect on the final two-layer film.

To re-emphasize the dynamics discussed above, snapshots of the two-layer profiles and the corresponding velocity streamline patterns at $t = 15$ are shown in Fig. 3.6. Since the flow is axisymmetric, the profiles in Fig. 3.6(a-c) are computed by creating mirror images of the corresponding profiles in Fig. 3.5. In Fig. 3.6(a), when $\eta_2/\eta_1 = 0.1$, a large single-layer film is formed surrounding a uniform two-layer film at the center. When both the fluids have same viscosity ($\eta_2/\eta_1 = 1$), a two-layer film is formed at the center surrounded by the capillary ridge of the upper layer as depicted in Fig. 3.6(b). When $\eta_2/\eta_1 = 10$, a small two-layer film at the center is formed which

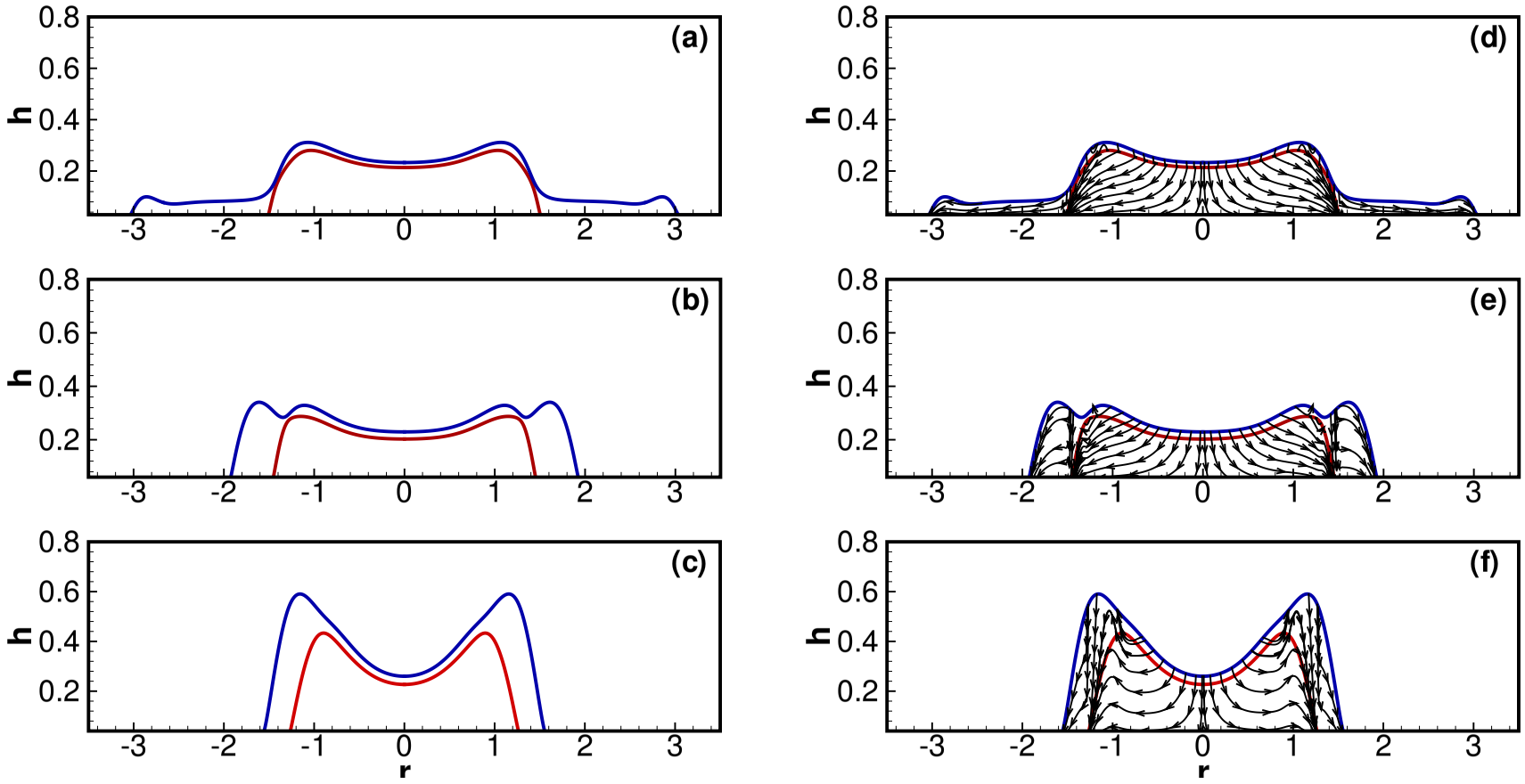

Figure 3.6: Film thickness profiles for three different viscosity ratios (a) 0.1, (b) 1, and (c) 10, respectively, computed at $t = 15$ and the corresponding streamline patterns (d)-(f). The profiles are computed for $\sigma_2/\sigma_1 = 1$, $C = 2.7 \times 10^{-2}$ and $b_1 = b_2 = 0.01$.

is surrounded by bulky capillary ridges at the contact line as described in the previous section. Moreover, the streamline patterns for both the layers are illustrated in Fig. 3.6(d-f), which explain the observed shape of the capillary ridges for both the layers. It shows that the lower layer fluid moves in the radially outward direction due to the applied driving force for all the viscosity ratios studied. However, the upper layer fluid shows interesting flow structures in the capillary ridge region. For $\eta_2/\eta_1 = 0.1$, the upper layer fluid surrounding the lower layer simply flows in radially outward direction. For $\eta_2/\eta_1 = 1$, the upper layer fluid just above the lower layer ridge, move in the upward direction, thereby accumulating the fluid in the ridge of the upper layer. This upward movement of the fluid in the upper layer becomes pronounced when $\eta_2/\eta_1 = 10$, leading to the formation of bulky capillary ridge. Figure 3.6 makes it plain that with increase in viscosity ratio bulkiness of the capillary ridge also increases.

3.3.2.2 Contact line evolution

Figure 3.7 shows the effect of viscosity ratio on the contact line evolution for both the layers. From Fig. 3.7(a), it is clear that for $t < 24.7$, the contact radius for the lower layer increases as the viscosity ratio goes down. This can be explained by the reason that the resistance offered by the upper layer fluid decreases as the viscosity ratio decreases. However, at a later time ($t > 24.7$), there is a crossover of the contact radii for viscosity ratios of 0.1 and 1.

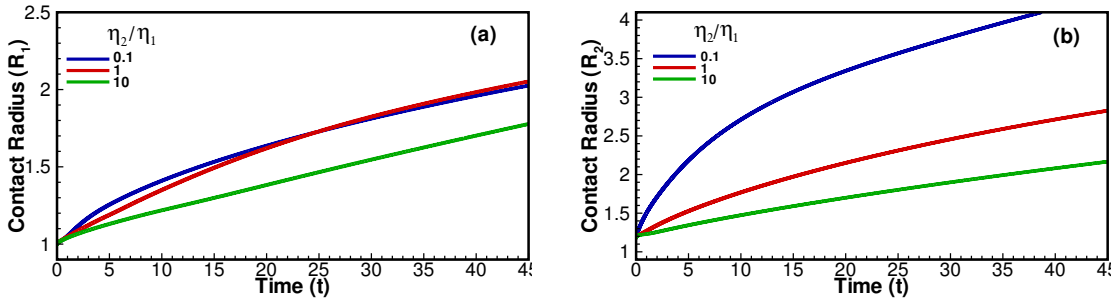

Figure 3.7: Numerically calculated values of (a) $R_1(t)$ and (b) $R_2(t)$ for lower and upper layer, respectively, plotted as a function of time, for three different viscosity ratios. Here, $\sigma_2/\sigma_1 = 1$, $b_1 = b_2 = 0.01$ and $C = 2.7 \times 10^{-2}$.

This crossover happens because the spreading rate of the lower layer fluid for $\eta_2/\eta_1 = 0.1$ is reduced due to the quick formation of large single-layer fluid surrounding it, while the lower layer fluid for $\eta_2/\eta_1 = 1$ continues to spread at the same rate. For even longer time they evolve almost at the same rate. Figure 3.7(b) shows the evolution of the outer contact radius, R_2. It is observed that spreading rate of the upper layer fluid increases with the decrease in viscosity ratio.

3.3.2.3 Film thickness at the center

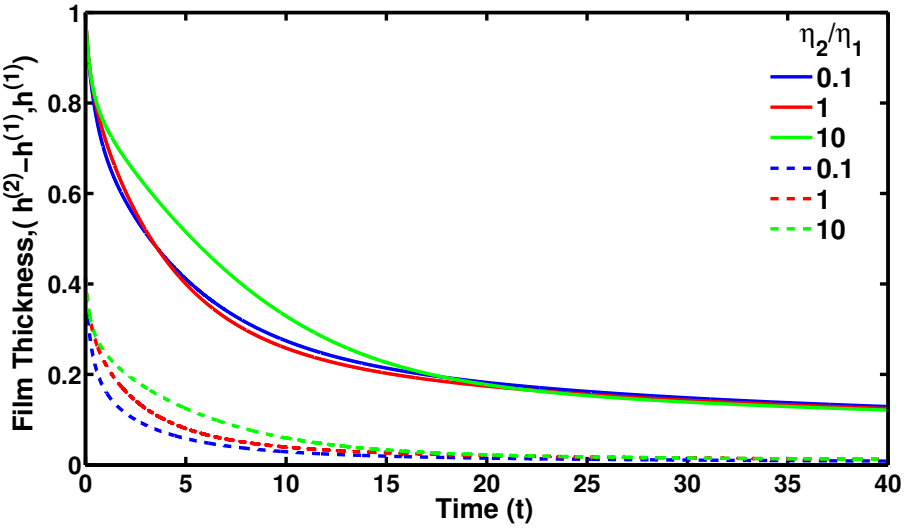

Figure 3.8: Numerically calculated values of the film thickness at the center $h^{(1)}$ and $h^{(2)} - h^{(1)}$ for the lower (solid lines) and upper layer (dotted lines), respectively, plotted as a function of time, for three different viscosity ratios. Here $\sigma_2/\sigma_1 = 1$, $b_1 = b_2 = 0.01$ and $C = 2.7 \times 10^{-2}$.

Figure 3.8 depicts the film thickness at the center versus time for both the layers. It is clear from the above figure that film thickness decreases monotonically with time for both the layers reaching the respective value of the precursor layer thickness at large time. Moreover, as the viscosity ratio decreases the film thickness for both the layers decreases. It is due to the ability of the upper layer fluid to spread faster as compared to the lower layer affecting the thinning rate of both the layers. However, there is a crossover in the film thickness in the lower layer at $t = 3.6$, for $\eta_2/\eta_1 = 0.1$ and 1. This effect occurs because the upper layer fluid for $\eta_2/\eta_1 = 0.1$ moves outward very fast. By the time the crossover happens, most of the liquid in the upper layer

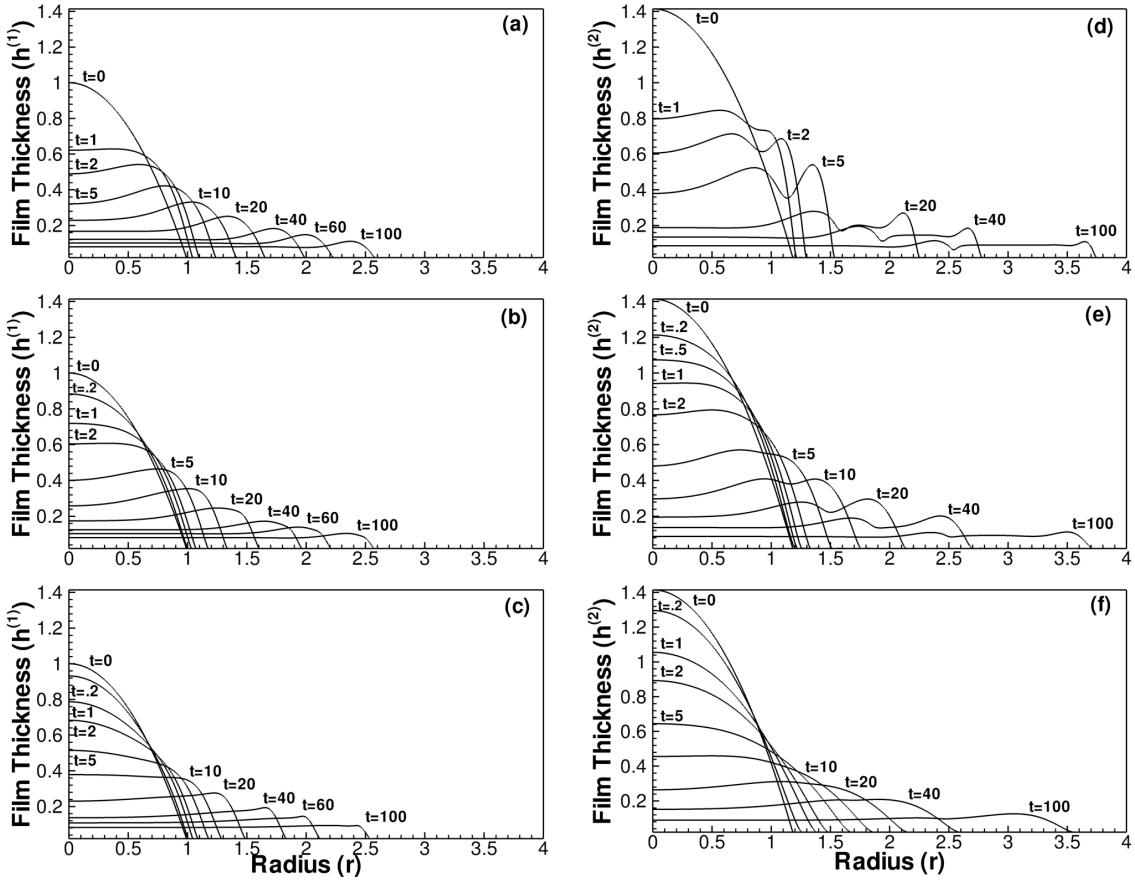

Figure 3.9: Film thickness profiles for three different ratios of interfacial tension $(a)0.1$, $(b)1$, and $(c)10$, respectively, for the lower (left) and upper layer (right). The profiles are computed for $\eta_2/\eta_1 = 1$, $C = 2.7 \times 10^{-2}$ and $b_1 = b_2 = 0.01$.

is drained out resulting in an almost planar film at the center which hardly allows any further thinning of the upper layer. Once the upper layer becomes thin enough, the viscous resistance in the thin upper layer becomes increasingly more important with the decreasing film thickness. Therefore, shear stress applied by the fluid in the upper layer slows down the evacuation of fluid from the lower layer resulting in the crossover. However, for $\eta_2/\eta_1 = 1$ both the liquids spread together due to equal viscosity and continue to thin at the same rate even after the crossover.

3.3.3 Effect of interfacial tension ratio

3.3.3.1 Film thickness profiles

The influence of interfacial tension ratio on the evolution of the two layers are investigated for three different ratios of interfacial tension, $\sigma_2/\sigma_1 = 0.1, 1$ and 10, respectively, for $0 \leq t \leq 100$. Figure 3.9 depicts the evolution of the film thickness profiles separately for the two layers. All the profiles are observed to be similar at later times even though their initial evolution is quite different. In Figure 3.9, a comparison of the corresponding profiles show that both the layers tend to become flat as the ratio of interfacial tension increases from 0.1 to 10. In other words, the sharpness of the capillary ridge decreases with the increase in interfacial tension with both the lower and upper layer films becoming almost flat for $\sigma_2/\sigma_1 = 10$. The flow dynamics in the capillary ridge region is determined by the balance between the surface tension force and centrifugal force. When the surface tension (σ) is small, the curvature term (h_{rr}) increases such that the surface tension force (σh_{rr}) balances the centrifugal force at the outer rim. Conversely, for a higher value of surface tension the curvature is small, and film is almost flat and smooth. It is also clear from the above figure that the spreading of fluid in both the layers increases as the ratio of interfacial tension decreases.

The above dynamics is further re-emphasized by taking snapshots of the two-layer film and the corresponding velocity streamline patterns formed at t=20 for three different interfacial tension ratios, as shown in Fig. 3.10. It is evident from Fig. 3.10 that the variation in the interfacial tension ratio significantly affects the upper layer profile while the lower layer remains almost unaffected. Moreover, Fig. 3.10(a) shows an interesting double ridge type profile. The liquid that drains out from the upper layer gets accumulated in the ridge region. However, the ridge becomes sharper in order to balance the centrifugal force. As the interfacial tension ratio increases, the film flattens out and the capillary ridge for the upper layer almost disappears producing a uniform two-layer film in the case of $\sigma_2/\sigma_1 = 10$ [see Fig. 3.10(c)]. Moreover, the streamline patterns for both the layers shown in Fig. 3.10(d-f) explain

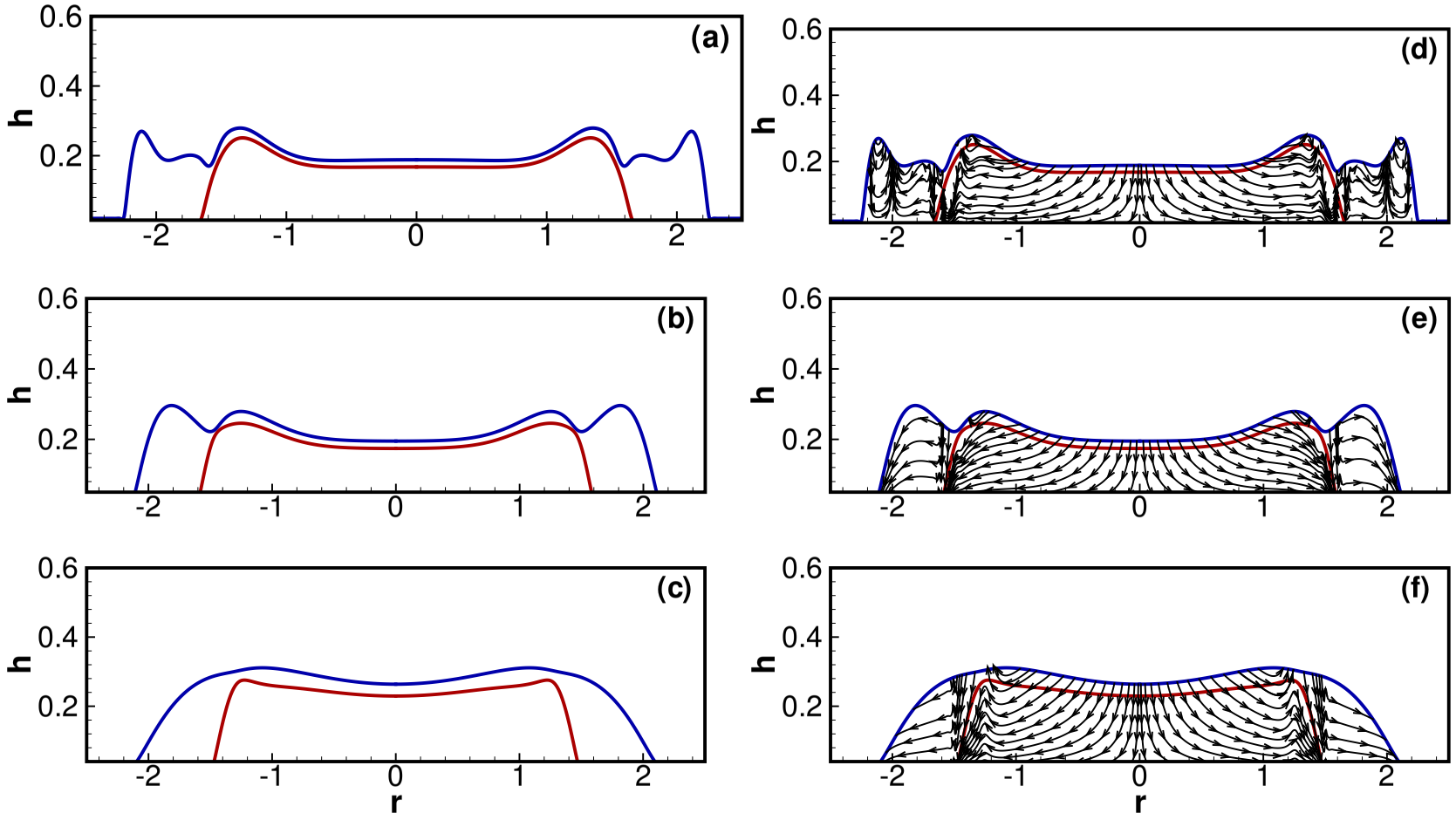

Figure 3.10: Film thickness profiles for three different ratios of interfacial tension $\sigma_2/\sigma_1 = (a)0.1$, $(b)1$, and $(c)10$, respectively, for both the layers computed at $t = 20$ and the corresponding streamlines (d)-(f). The profiles are computed for $\eta_2/\eta_1 = 1$, $C = 2.7 \times 10^{-2}$ and $b_1 = b_2 = 0.01$.

the observed shape of the capillary ridges. It shows that the fluid in both the layers move in the radially outward direction due to the applied driving force for all the interfacial tension ratios studied. However, the upper layer fluid for $\sigma_2/\sigma_1 = 0.1$ shows an interesting flow structure in the capillary ridge region [see Fig. 3.10(d)]. The fluid in the ridge near the contact line circulates back forming the second capillary ridge in between the two ridges formed in the upper layer.

3.3.3.2 Contact line evolution

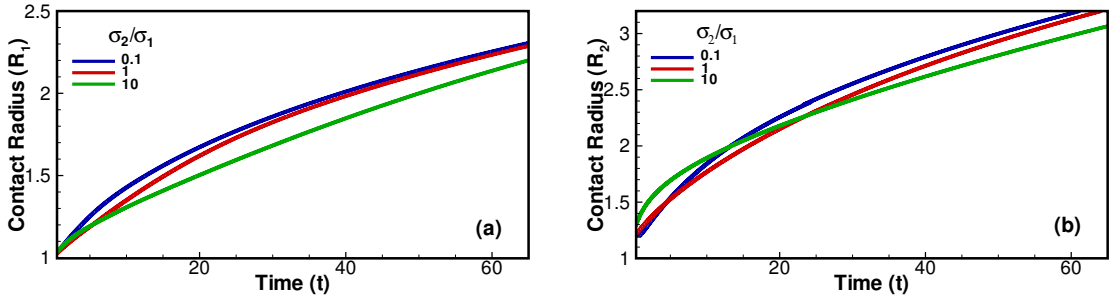

Figure 3.11: Numerically calculated values of (a) $R_1(t)$ and (b) $R_2(t)$ for lower and upper layer, respectively, plotted as a function of time, for three different ratios of interfacial tension. Here, $\eta_2/\eta_1 = 1$, $b_1 = b_2 = 0.01$ and $C = 2.7 \times 10^{-2}$.

Figure 3.11(a) clearly shows that the contact radius for the lower layer increases as the ratio of interfacial tension decreases. Figure 3.11(b) shows the evolution of contact radius for the upper layer. In contrast to the lower layer, evolution of contact radius for the upper layer is much more interesting with the occurrence of multiple crossovers. The first crossover occurs between the contact radii for $\sigma_2/\sigma_1 = 0.1$ and 1 at $t = 4.5$, and the reason for this crossover is explained as follows. Initially, for $\sigma_2/\sigma_1 = 0.1$ most of the fluid accumulate in the capillary ridge region and the contact line does not move significantly. The bulky capillary ridge then experiences a large centrifugal force pushing the contact line to move outward at a faster rate as compared to the case of $\sigma_2/\sigma_1 = 1$. There are two other crossovers at $t = 13$ and $t = 23.5$ between the contact radii for $\sigma_2/\sigma_1 = 0.1$ and 10, and $\sigma_2/\sigma_1 = 1$ and 10, respectively. Both these crossovers occur because the upper layer for $\sigma_2/\sigma_1 = 10$, does not form a sharp capillary ridge. Consequently, the liquid in the upper layer

drains out very slowly resulting in slow spreading of the film.

3.3.3.3 Film thickness at the center

The numerical simulation indicates that film thickness at the center decays monotonically with time for all the interfacial tension ratios studied [See Fig. 3.12]. For an initial period of time (i.e., $t < 30$), film thickness for both the layers decreases with a decrease in the interfacial tension ratio. At long times, it decays asymptotically to attain the corresponding value of the precursor layer thickness for both the layers.

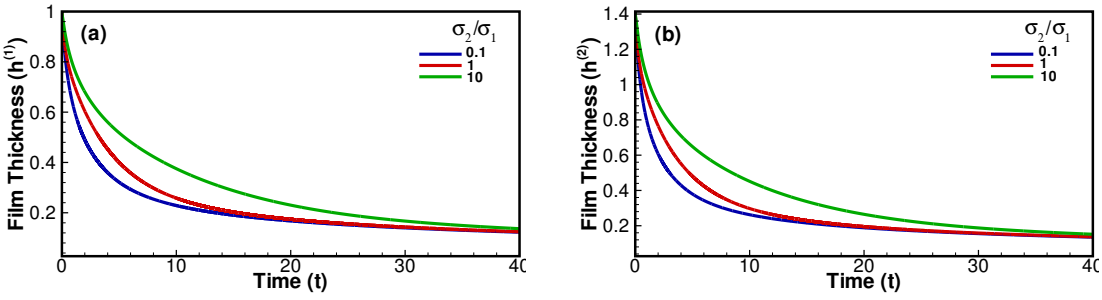

Figure 3.12: Numerically calculated values of the film thickness at the center (a) $h^{(1)}(t)$ and (b) $h^{(2)}(t)$ for lower and upper layer, respectively, plotted as a function of time, for three different ratios of interfacial tension. Here, $\eta_2/\eta_1 = 1$, $b_1 = b_2 = 0.01$ and $C = 2.7 \times 10^{-2}$.

3.3.4 Effect of precursor layer thickness

3.3.4.1 Film thickness profiles

The influence of dimensionless precursor layer thicknesses b_1 and b_2 on the final two-layer film formed is investigated for three different values of thicknesses $b_1 = b_2 =$ 0.001, 0.01 and 0.1, respectively, while the properties of the two fluids being the same. Figure 3.13 depicts the profile of two-layer film computed for the cases above. In a precursor layer model of contact line, it is assumed that the surface is already wetted with a small film of the same fluid. In essence, a high value of precursor layer thickness (b) implies high ability of the fluid to wet the surface. Figure 3.13 shows that the spreading rate of both the layers increases with the increase in the thicknesses b_1 and b_2. Figure 3.13(c) corresponding to $b_1 = b_2 = 0.1$ shows the maximum spreading

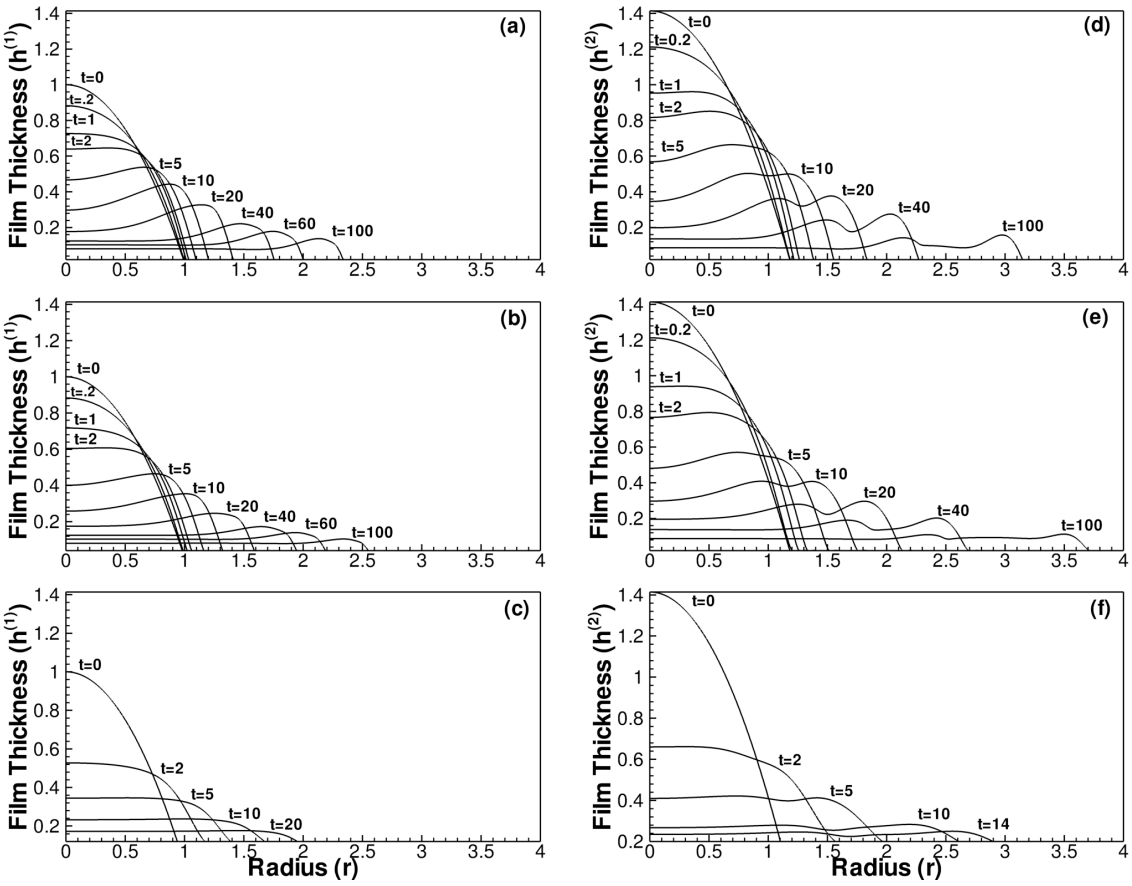

Figure 3.13: Film thickness profiles for three different values of dimensionless precursor layer thicknesses $b_1 = b_2 = 0.001(a), 0.01(b)$, and $0.1(c)$ for the lower layer(left) and upper layer(right). Here, $C = 2.7 \times 10^{-2}$ and fluids in both the layers have same physical properties.

while Fig. 3.13(a) with $b_1 = b_2 = 0.001$ shows the least spreading. The variation in the precursor thickness also affects the sharpness of capillary ridge. As shown in Fig. 3.13, the sharpness of capillary ridge decreases with the increase in precursor layer thicknesses b_1 and b_2 as the fluid has a tendency to spread more for a larger value of precursor layer thickness. The increase in the precursor layer thickness can be considered similar to increase in slip velocity, thus increasing the rate of spreading. The effect of change in the precursor layer thickness on the film profiles follows a trend similar to the one observed for single-layer coating of Newtonian fluids [22,59].

3.3.5 Effect of initial volume ratio

3.3.5.1 Film thickness profiles

Figure 3.14 shows the snapshots of the film profile at $t = 10$ for three different ratios of initial volume. It shows, when both the fluids have same initial volume $V_2 = V_1$, most of the liquid material is used in forming a two-layer film. If the initial volume of upper layer fluid increases $V_2 = 2V_1$, then the extra added fluid in upper layer is wasted in forming a large single-layered film and produces a small two-layer film. The trend is maintained on increasing the volume further $V_2 = 3V_1$, as shown in Fig. 3.14. The above analysis dictates that a proper balance of initial volume is required to form a large two-layer film with minimum loss of the material of fluids in either layer.

3.4 Conclusions

In this chapter, a systematic study of the two-layer spin coating process was carried out using numerical simulations. The study was focused on observing the effect of fluid property ratios and process parameters on the time evolution of film profile and capillary ridge formation. The axisymmetric 1D model equations governing the flow were developed and solved numerically using the G/FEM based approach. The singularity of the contact line was resolved using a precursor layer model. The results

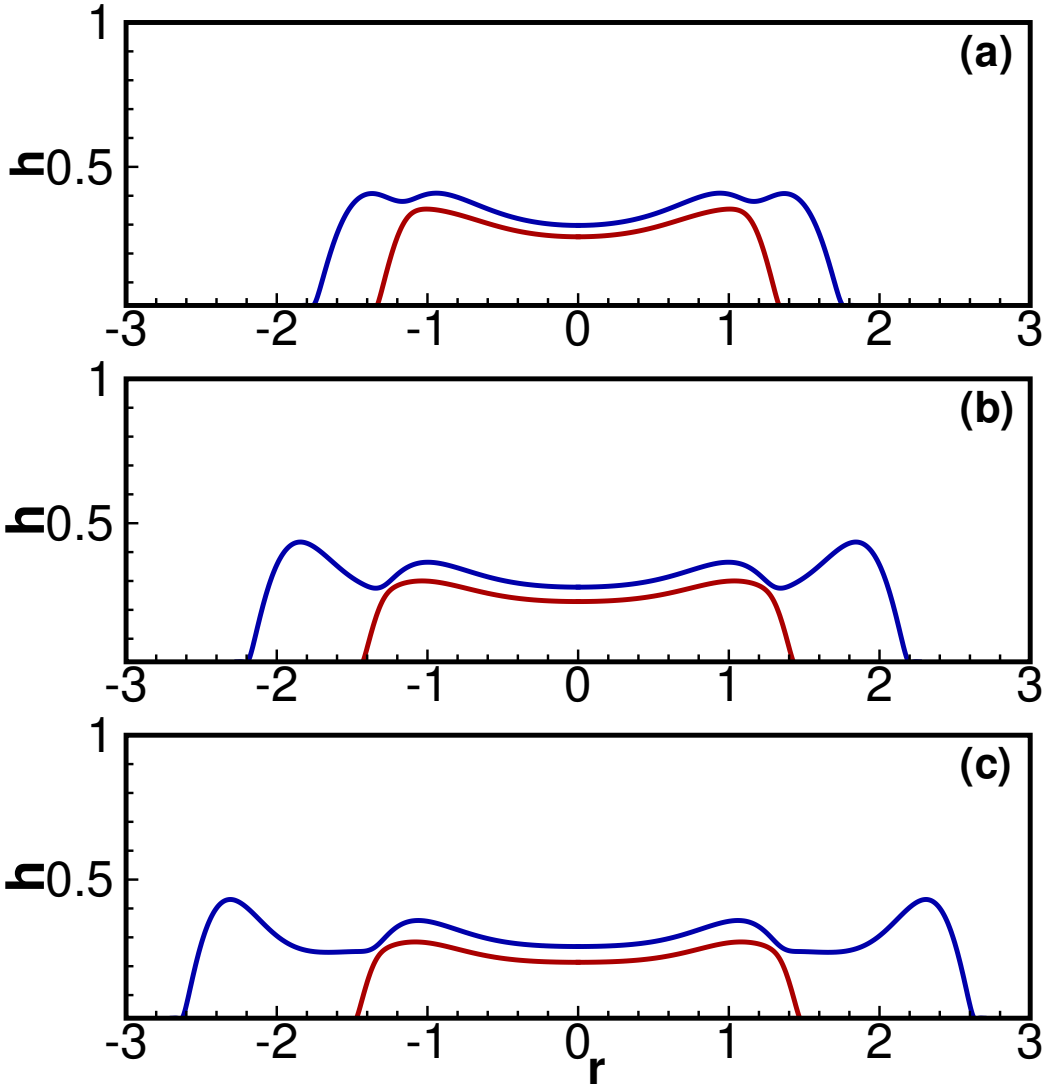

Figure 3.14: Film thickness profiles for three different volume ratios $V_2/V_1 = 1, 2$ and 3. The profiles are computed at a non-dimensional time $t = 10$. The profiles are computed for $C = 2.7 \times 10^{-2}$ and $b_1 = b_2 = 0.01$. Here, the fluids in both the layers have same physical properties.

reported include the effects of viscosity ratio, interfacial tension ratio, precursor-layer thicknesses and initial volume ratio of the fluids present in the two layers. All the ratios studied were defined as property of fluid II (upper layer) with respect to the property of fluid I (lower layer).

It was observed that bulkiness of the capillary ridge increases with an increase in the viscosity ratio. Also, the capillary ridge becomes sharper with the decrease in the interfacial tension ratio. However, the final two-layer film formed in the former case is small and non-uniform as compared to the later. Moreover, the sharp capillary ridges so formed could affect the uniformity of the two-layer film. Nevertheless, the results suggested that a uniform two-layer thin film can form when the fluid in the upper layer is less viscous or when the upper gas-liquid surface tension is more than the inner liquid-liquid interfacial tension.

In addition to the above parameters, precursor layer thickness and initial volume ratio were also found to have significant effect on the uniformity of the two-layer film. It was observed that the increase in the precursor layer thickness facilitated the film to become uniform. It is important to note that the increase in the volume ratio did not affect the uniformity of the film, rather the extra amount of fluid was used in forming either a bulky capillary ridge or a large single-layer film surrounding the two-layer film. Therefore, operating the process with an equal volume of the fluids in both the layers will produce a uniform two-layer coating film with minimal loss of the liquids.

Although this study was focused on Newtonian liquids, its procedure and results may serve as a basis for extending the present model to study the two-layer spin coating process of non-Newtonian fluids such as polymer melts, emulsions and suspensions. The future work in this field will aim to develop a numerical algorithm to study the stability of the capillary ridges to azimuthal perturbations.

Chapter 4

Instability in liquid-liquid thin film spreading on a spinning disc

4.1 Introduction

Simultaneous spreading of stratified layers of two thin liquid (Newtonian) films, on a horizontal spinning disc, has been the subject of recent investigations, as discussed in Chapter 3. The liquid layers considered in these studies were assumed to be infinite in extent. Very recently, McIntyre and Brush [48] modeled the evolution of film thickness in such a system by using lubrication theory. Their analysis revealed that the film thickness of both the layers is much more sensitive to minute changes or disturbances in the lower layer. Similar analysis was carried out to understand the effect of fluid property ratios on the thinning evolution of two fluid layers of uniform thicknesses at low and high Reynolds numbers [49,50]. However, all these studies have explored the effect of fluid properties and process parameters on film thinning and interface evolution, away from the two contact lines.

We, thus, incorporated the effect of capillary pressure in our 1D axisymmetric two-layer flow model, to understand the contact line evolution as well as shape of the capillary ridge in the above system. Our simulation results considering wetting Newtonian liquids, as reported in the previous chapter, revealed that, for small enough viscosity ratios, a two layered film is formed surrounded by a single layer film of outer

liquid while for higher viscosity ratios, a two layer film is formed surrounded by bulky capillary ridges. Also, decreasing the ratio of surface to interfacial tension resulted in an increase in the sharpness of the capillary ridge for both the liquids. Most importantly, varying the initial volume ratio of the fluids is found to have a negligible effect on the two-layer film. Our study is different form the previous study [48] which focuses on effect of initial disturbances on the evolution of interfacial instability in both the layers.

As evident from above discussion, all the previous studies lack in explaining the dynamics of contact line fingering instability in layered fluids, typically observed in thin films of single liquid. [46,62,63] The instability appears at the contact line of the spreading liquid, due to the formation of capillary ridge which is unstable to slight perturbation in the angular direction leading to formation of fingers. The onset and evolution of fingering instability in thin film flow of single liquids is observed to be dependent on physical properties of the liquid and operating variables. However, the effect of these variables on the instability is unknown for simultaneous spreading of superposed drops of two liquids. In particular, it is not clear whether introducing another liquid will suppress or enhance (control) the instability in such a system. Indeed, such controlling of liquid-liquid interfacial instability, but driven by viscosity differences, in a Hele-Shaw cell, has been reported recently [87] wherein, the instability behavior was found to alter dramatically while using a cell with varying cross-section (geometry) along the flow length instead of keeping it constant as in a typical Hele-Shaw flow. Apart from the fundamental understanding and control of the instability behavior for two fluid film flows, the flow dynamics observed in this work will significantly aid in the understanding of processes dealing with multi-layer coatings of surfaces. Such flow of layered films is also relevant for the processes involving bi-layered or vertically segregated thin films [88]. The droplet formation phenomena observed in this study will be of considerable interest for pharmaceutical processes making microspheres using centrifugal atomization technique [11]. It can be applied for the production of encapsulated microspheres of two different drug ingredients, thereby expanding the range of options available for combination therapy.

The objective of this Chapter is to experimentally investigate the spreading and instability behavior during the simultaneous spreading of a two-liquid system (drop on a drop) on a rotating substrate which will provide answers to some of the pertaining issues cited above. The primary focus here is to find out the effect of variation in the volume ratio of the two liquids on the instability behavior. This system also allows us to study the interaction between the contact lines of both the liquids by a simple variation in the volume ratio of the two liquids.

4.2 Experimental Details

4.2.1 Materials and Apparatus

The experimental system is shown in Fig. 4.1. It consists of a smooth, flat, aluminimum disc of diameter 15 cm rotated using a computer controlled DC stepper motor in the speed range $50 - 10000$ revolutions per minute (rpm). The disc attains the desired speed from rest in less than 0.5 s using an acceleration of 1000 rpm/s. The feedback controller mechanism ensures that the random fluctuations in the rotational speed are within 2% for 250 rpm while they are within 5% for 1000 rpm.

Two Newtonian liquids were used in the experiment, the properties of which are listed in Table 4.1. The two liquids were chosen to have the same viscosities and nearly same densities, but with significant difference in the surface tension (hence contact angle) values. This ensured that the observed behavior is primarily due to the differences in the surface tension values. The surface tension of the two liquids and their interfacial tension were measured using the well known pendant drop method. The static contact angles for both the liquids with the aluminium disc in presence of air was obtained by placing the drop of the liquid on the horizontal disc and imaging by a camera placed sideways and in the plane of the disc. The resulting image was analyzed using ImageJ software to obtain the static contact angle. The same imaging technique was, however, not accurate enough to obtain the static contact angle made by the liquid-liquid interface with the disc surface. The viscosity values for both the

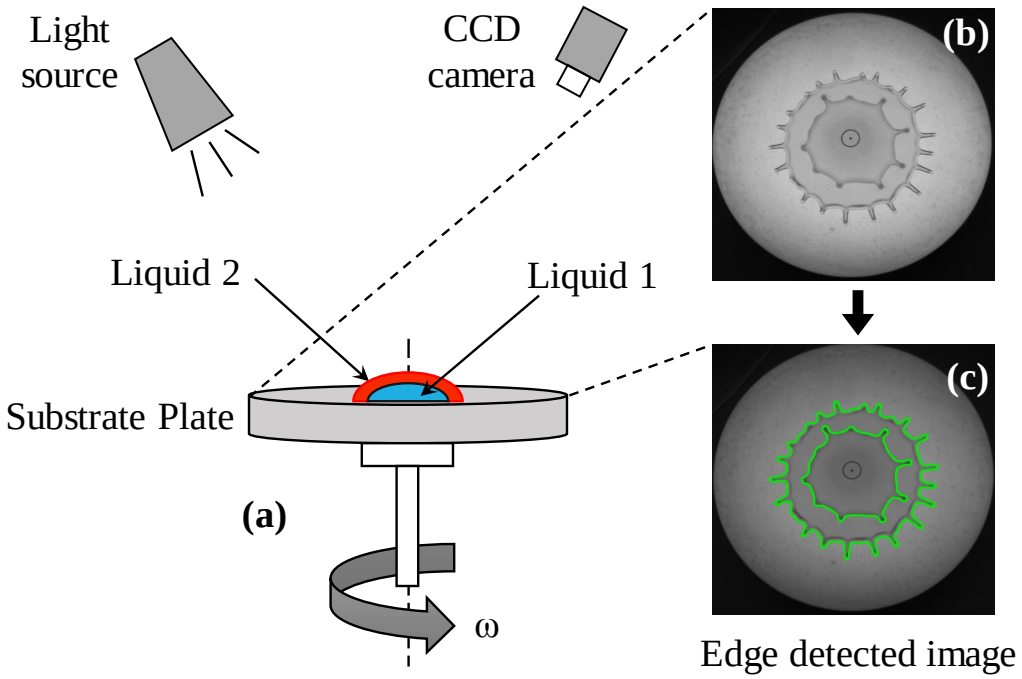

Figure 4.1: Schematic of the experimental set up. (a) Spinning disk assembly and image acquisition system. Area colored blue represents liquid 1 while that colored red represents liquid 2 (see Table 4.1). (b) Sample image taken at certain stage of spreading. (c) Same image as in (b) but superimposed with the edge detected coordinates for the inner as well as outer interfaces.

liquids were obtained using Brookfield digital viscometer employing a cone and plate geometry.

4.2.2 Experimental Procedure

As shown in Fig. 4.1, the initial state comprised of a drop of liquid uniformly covered by a drop of another liquid on top while confirming that their axes coincided with

Table 4.1: Physical properties of the liquids used in the spin-coating experiments and equilibrium contact angle of the drop on aluminium substrate. The interfacial tension for the castor oil-glycerol interface was measured to be 18.96 mN/m.

Liquids	Density (kg m^{-3})	Viscosity (Pa s)	Surface tension (mN/m)	Static contact angle (deg)
Glycerol (Liquid I)	1260	0.654	64.20	~ 64
Castor Oil (Liquid II)	960	0.670	32.74	~ 31

each other and also with that of the substrate plate. A drop of liquid 1 (inner liquid) of volume V_1 was put onto the plate through a hollow, cylindrical tube placed vertically and with its one end flushed with the substrate face and its axis coincident with that of the plate. The drop remained on the substrate plate with minimum contact with the tube edges. The tube was lifted very slowly using micrometer screw arrangement and the drop was allowed to spread to its equilibrium shape corresponding to its static contact angle, which took a few minutes. Following this, another tube, but with a larger diameter was similarly placed over the plate while enclosing the first drop. The second liquid of specified volume V_2 was then poured onto the plate in minute quantities near the inner edge of the tube so that all the liquid accumulates and encloses the inner drop completely and uniformly. The pouring near the edge was required to prevent the possible break-up of the inner drop of liquid when second liquid was poured directly over it. The tube was then lifted very slowly using the micrometer screw. This drop-on-drop conformation was allowed to reach their equilibrium position, which required a few minutes. The lifting of the tubes, however slowly, resulted in the adhering of small amounts of liquid to its edges which was accounted for carefully. A well-defined enclosed drop configuration required the inner liquid to have higher surface tension than that of the outer liquid (liquid 2). Reversing the positions was not possible as the outer liquid, with higher surface tension, cannot uniformly enclose the inner liquid drop. The final configuration resulted in an outer liquid-air-solid contact line and inner liquid-liquid-solid contact line.

The volume (V_1) of liquid 1 was kept constant at 0.5 ml, while volume (V_2) of liquid 2 was varied from 1 to 6 ml so as to have the value of V_2/V_1 in the range $2-12$. The primary reason behind varying volume ratio was to elucidate the effect of proximity of the two contact lines with respect to each other. Note that constant V_1 yields constant initial radius of inner liquid while increasing V_2 results in increasing initial radius of outer liquid and hence pushes the outer contact line further away. The lower limit of V_2 was fixed so as to prevent the merging of the two contact lines, if very close together, while upper limit was determined based on the fixed plate diameter which allows for obtaining reasonable amount of data before the spreading

liquid spills near the substrate edge.

The disc surface, before every experiment, was washed multiple times using soap solution and rinsed with DI water followed by acetone to remove any traces of liquid from previous experiments. This protocol ensured the reproducibility of the experimental results. All experiments were carried out at a fixed angular speed of 400 rpm. Each experiment was repeated 4 times and the results presented are averages over these experiments.

4.2.3 Imaging and Analysis

The spreading dynamics was imaged using a high speed (CCD) camera (Teledyne DALSA), interfaced to a computer which records images of the flow as it progresses at specified intervals. The camera exposure was adjusted to acquire sharp images. The disc surface was illuminated from above using a bright, halogen lamp. A small amount of blue colored ink was added to liquid 1 so as to identify its spreading boundary (i.e. interface between inner and outer liquid) very accurately (See Fig 4.1(b)). It was verified that the addition of the ink does not alter the surface tension of the liquid. The viscosity of liquid 1 was measured with ink added to it. The camera, as shown in Fig. 4.1(a), is placed slightly inclined to the vertical. This is to prevent the reflection of the camera from the optically flat substrate surface appearing in the images which can create difficulty in image analysis.

The oblique positioning of the camera with respect to the plate surface makes the drop and plate appear non-circular in the images due to unequal distance of different regions on the plate from the camera. This spatial variation was taken into account by imaging four concentric circles drawn on a similar plate, under similar camera, plate and light positioning, spanning the whole area and obtaining the coordinates along the circumference of each circle (See Fig. 4.2). The alternate positioning of white and black bands as shown in the figure makes the detection of the circles much easier. This procedure provided the ratio between the actual radius and the apparent radius obtained from the images at different spatial locations which was then applied to the fluid spreading images appropriately. Increasing more measurements (i.e. drawing

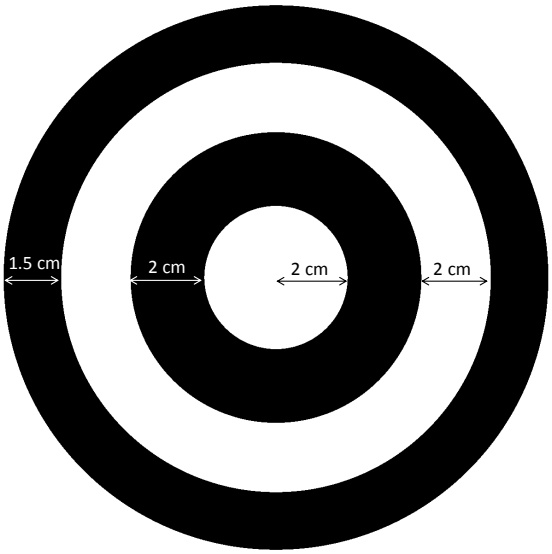

Figure 4.2: Scale used for image calibration.

several more concentric circles) improved the correction by a negligible amount.

The acquired images were analyzed in ImageJ and MATLAB® to track the position of the interface and extract its behavior. The sequence of steps involved in the edge detection process is shown in Fig. 4.3. First, the raw image is converted to a binary image. In the next step, the image is inverted and the connected component (drop) having only white pixels (the required object) is identified. Any noise in the required object image is then removed and finally, the edge is extracted using standard edge detection algorithm ('sobel' method) available in MATLAB's inbuilt image analysis tool. The edge detected coordinates were calibrated using the scale shown in Fig. 4.2. The algorithms use the polar and Cartesian coordinate systems with the origin at the center of the disc. The edges were detected to an accuracy of ± 0.15 mm (see Fig. 4.1(c)).

The edge detection data was used to calculate several quantities, viz., effective radius (r) at different radial locations (i.e., different times), critical radius, spreading rates, number of fingers, and evolution of the finger front position. The effective radius at different times before the onset of instability, was obtained by fitting a circle to the edge detected coordinates.

In order to find the finger front position as a function of time, the image data

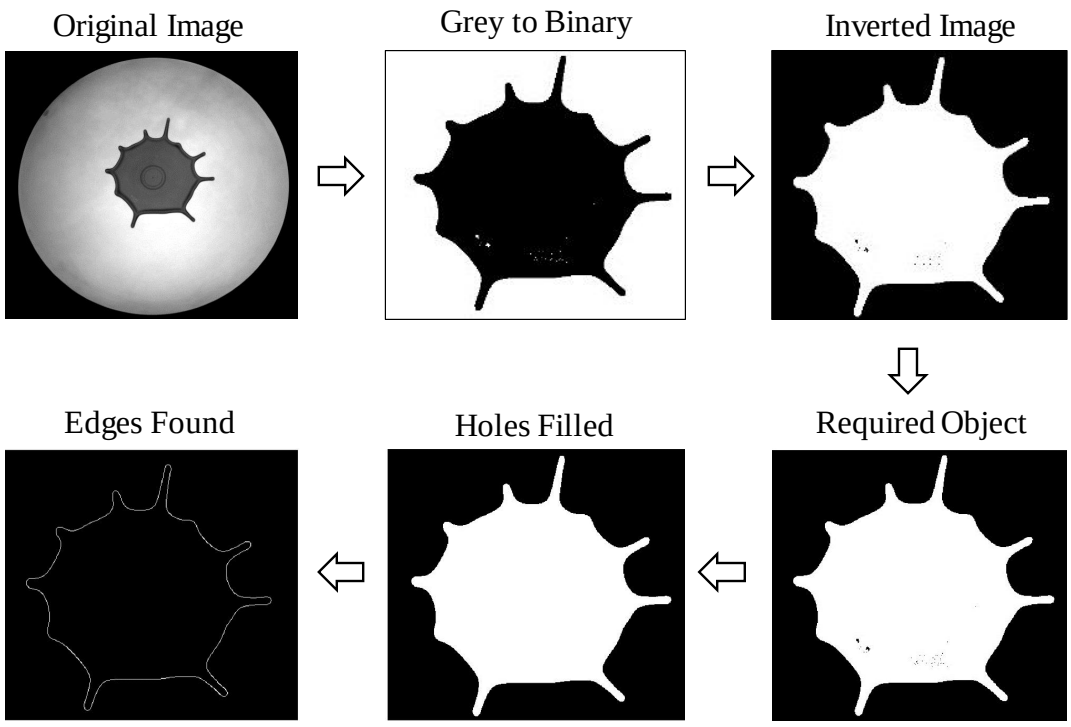

Figure 4.3: Sequence of operations involved in the processing of raw image to extract the edge of a spreading drop.

was first converted to polar coordinates $(r - \theta)$ and the local maxima (finger tips) in each image data was found out as shown in Fig. 4.5. Then, one particular finger tip position was tracked in subsequent images to find out the position of the finger front with time. Depending on the rotational frequency and the camera frame rate, the tip position of a particular finger in the next image was obtained by searching within a specified range of angular distance. After finding out the front position with time for several fingers in a particular experiment, it was observed that the trends were not much different for all the fingers as compared to the fastest growing finger. Therefore, the data is reported only for the fastest growing finger in all the experiments. In the following sections we will refer to liquid 1 and liquid 2 as inner and outer liquids, respectively.

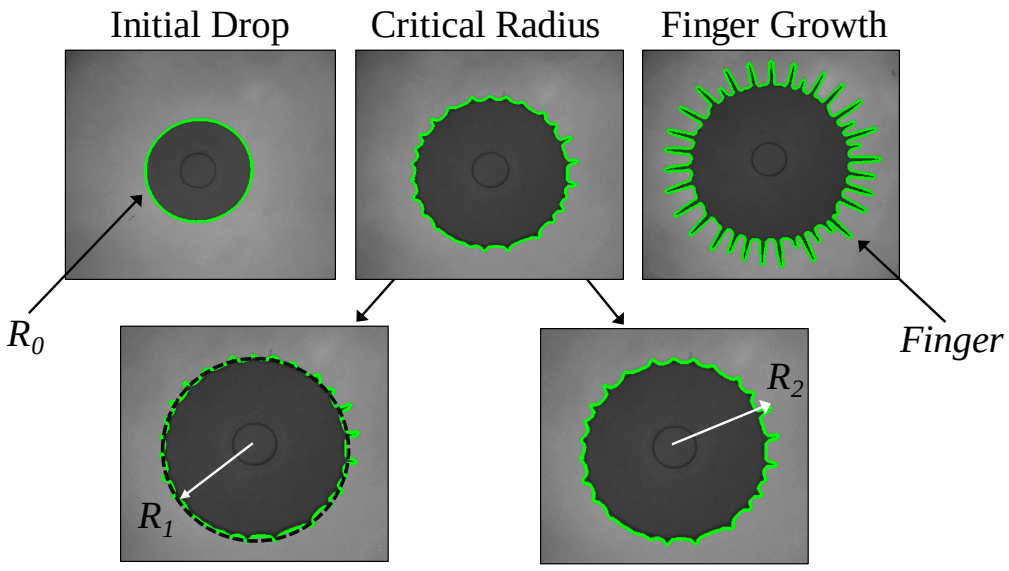

Figure 4.4: Images showing the definition of quantitative parameters obtained using image analysis.

4.3 Results and Discussion

In the following, the qualitative aspects of the spreading behavior for the system at all times are discussed at first, followed by quantitative estimates about axisymmetric spreading and fingering instability. Finally, some interesting early results on drop formation in two-liquid system are presented.

4.3.1 Spreading behavior

Figure 4.6 shows the experimental images of the liquid spreading at different times for an angular speed of 400 rpm. The first column represents spreading of the single liquid (glycerol) with a free air-liquid interface, while columns $2-6$ represent spreading of the same drop of liquid (glycerol), but now with the outer liquid (castor oil) enclosing it for varying volume ratios. The first row in each case represents the initial drop configuration when the disc is stationary. The outer liquid, with its lower surface tension and higher volume spreads to a larger extent. However, single fluid of glycerol with its higher surface tension and lower volume spreads to a lesser extent. The apparent size of the drop for glycerol (inner liquid), looks a bit larger

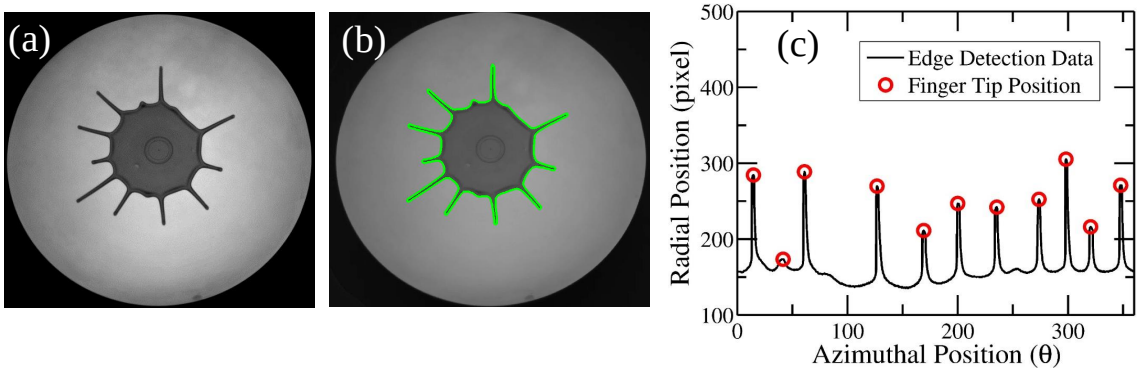

Figure 4.5: Steps involved in tracking the finger front position. (a) Original experimental image, (b) corresponding edge detected coordinates superimposed on the original image, and (c) finger tip positions in (b) plotted in polar coordinates $(r - \theta)$.

(1-3%) when enclosed by the outer liquid than without. This can be attributed to lower liquid-liquid interfacial tension, hence smaller contact angle (see caption of Table 4.1), resulting in initial spreading to a larger extent. Unfortunately, our imaging technique does not allow us to measure this interfacial contact angle accurately.

Once the disc starts to rotate, the liquids spread, form instabilities which eventually grow into fingers. The drop of glycerol spreading with an outer air-liquid free surface (column 1), spreads to a certain extent before instability ensues (second row), leading to the formation of fingers and further growth; through which the liquid flows out. This instability inception (or critical radius R_c as referred to in the literature) is captured in terms of the degree of deformation of the drop boundary of the liquid. The degree of deformation is defined as $[(R_1 - R_2)/R_2] \times 100$, where R_1 is the largest radius of the drop (distance of the farthest point from the axis of rotation) and R_2 is the radius of circle centered on the axis of rotation and having same area covered by the drop (See Fig. 4.4). The row 2 in Fig. 4.6 corresponds to a contact line deformation of 10%. This spreading, instability formation and finger growth for the spreading of a drop of glycerol (single liquid) depicted (in column 1) is very much in accordance with the linear stability theory predictions for single liquid spreading with air interface[46,62].

The spreading behavior of the same volume of the glycerol drop in presence of the outer liquid (castor oil) is, however, qualitatively different as shown in Fig. 4.6.

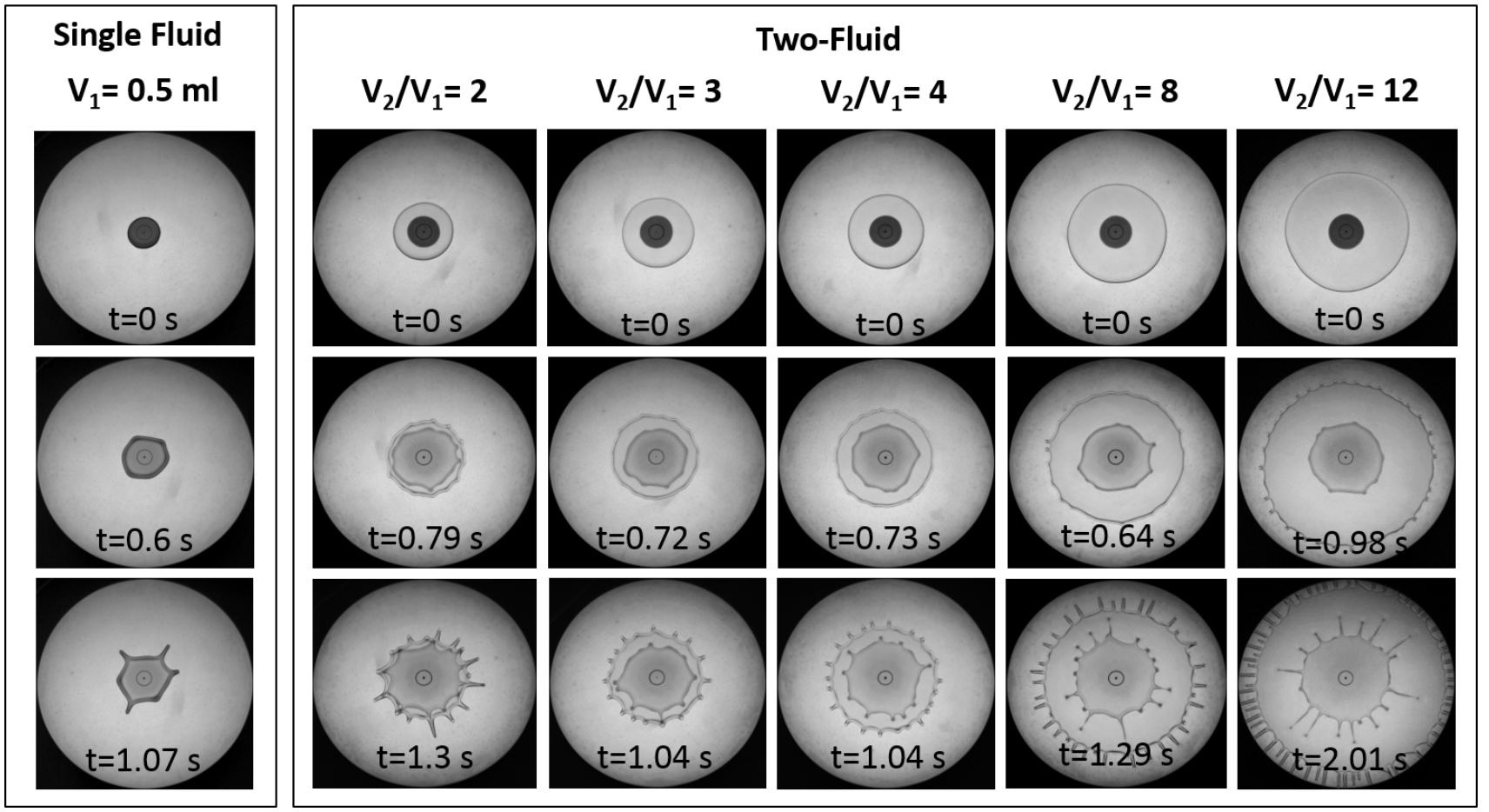

Figure 4.6: Images showing the various stages of spreading and fingering of a glycerol drop in the presence of the outer liquid (castor oil) on top, for a constant angular speed (ω) of the spinning disc (400 rpm). The central dark region and the transparent region in each image corresponds to inner and outer liquids, respectively. Each column corresponds to an experimental set for a particular combination of the two liquids. The rows correspond to the state of the liquid at a particular time (embedded in each image). Out of the two panels in the image, the left panel corresponds to the spreading of inner liquid while the panel on the right corresponds to two-liquid spreading experiments for varying volume ratio of the two liquids.

It spreads to a larger extent before instability ensues (second row). Further, the instability ensues at a delayed time (notice the time stamps provided in each image window in Fig. 4.6). These qualitative differences can be attributed to lower value of liquid-liquid interfacial tension, hence higher affinity for spreading before instability. This observed behavior is weakly dependent on the volume ratios V_2/V_1 studied, which can be expected given that the interfacial angle will be dependent on liquid-liquid interface. At later times (3^{rd} row), it can be observed that the enclosed inner liquid, breaks into more fingers as compared to that without, which also seems to be weakly dependent on the volume ratios studied. The base radius for the inner liquid, whether enclosed or otherwise, increases to a smaller extent post instability initiation for all the cases studied.

With increasing volume ratios, the outer liquid, with much lower surface tension and contact angle, spreads to a much larger extent and breaks into many more fingers. Note that the spreading behavior of outer liquid is unaltered with or without inner liquid (images not shown), for all volume ratios studied. This is expected as the thin film spreading and instability is predominantly governed by the contact line behavior, which for outer liquid will remain the same irrespective of the presence of inner liquid. The spreading behavior of outer liquid is in close agreement with the predictions of the linear stability theory[46] and previous experiments[62] for a single liquid spreading in air [See Fig. 4.14]. The primary observation in two-liquid system is, thus, the alteration of instability behavior of inner liquid by the outer liquid.

For the smallest volume ratio studied, with the outer contact line being closest to the inner liquid-liquid contact line, the fingers emanating from inner liquid seem to merge with those of the outer liquid, which we will show quantitatively later on. This is more clearly seen in the magnified image shown in Fig.4.7 for the case of V_1 =0.5 ml, $V_2/V_1 = 2$. The instability pattern of the inner liquid follows that of the outer liquid with slight phase shift in the angular direction.

Further, at largest volume ratio studied and particularly at long spreading times, the inner liquid starts to emit liquid droplets from the ensuing fingers. Both these phenomena do not have any analogues in case of single liquid spreading and do not

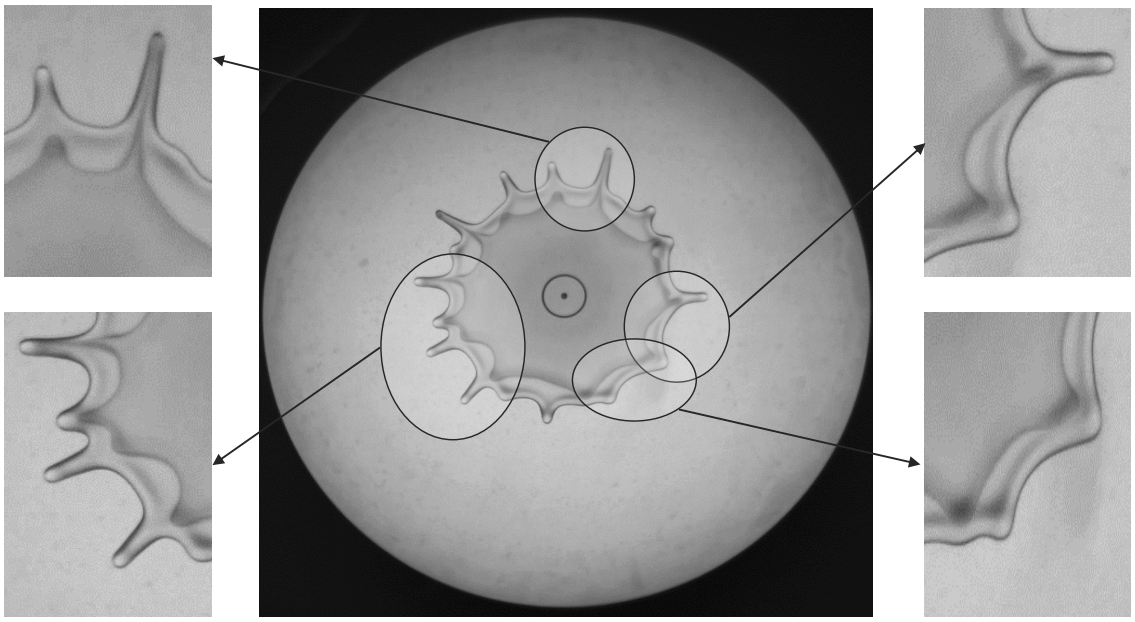

Figure 4.7: Magnified image at a particular instant of spreading for V_1 =0.5 ml, $V_2/V_1 = 2$. Here, the instability of inner liquid shows similar instability as the outer one with a minute phase shift in the azimuthal direction.

come within the purview of theories established for thin film spreading.

The quantitative data extracted from the analysis of images is discussed next. The evolution of drop radius for all cases, prior to instability initiation (i.e. traversing from row 1 to row 2 in Fig. 4.6), is shown in Fig. 4.8. The red symbol in each profile represents the time at which instability ensues. The drop radii (r_i), are non-dimensionalized by the corresponding initial radius, R_{0i} of stationary drops, while the spreading time t is non-dimensionalized using corresponding $T_{0i} = \mu_i/(H_{0i}^2\rho_i\omega^2)$ as used previously for single liquid spreading[46]. Here, the subscript, $i = 1, 2$, represents inner liquid (liquid 1) and outer liquid (liquid 2), respectively. The symbols μ_i , ρ_i, H_{0i} are, respectively, the viscosity, density, initial height of the corresponding liquid and ω is rotational speed of the plate. The initial height H_{0i} is calculated, by considering the drop to be of a flat disk (or cylindrical) shape whose volume is known and the radius is obtained by image analysis. The spreading rate is predominantly governed by the outer region (region away from the contact line), and the dimensionless parameters for the outer region are chosen accordingly, which has been used widely in the literature.

The length scale is chosen to be R_{0i}, which is the initial radius of the drop while the time scale, T_{0i}, is chosen as the ratio of the length and velocity scale for the outer region (i.e, R_{0i}/U_{0i}), where U_{0i} is the height-averaged radial velocity obtained by the balance between the centrifugal and the viscous force. The primary reason behind this non-dimensionlization was to compare the single and two-liquid spreading rate prior to the onset of instability. With this scaling, the dimensionless data (for both inner as well as outer liquid) is expected to collapse if they correspond to identical dimensionless initial conditions.

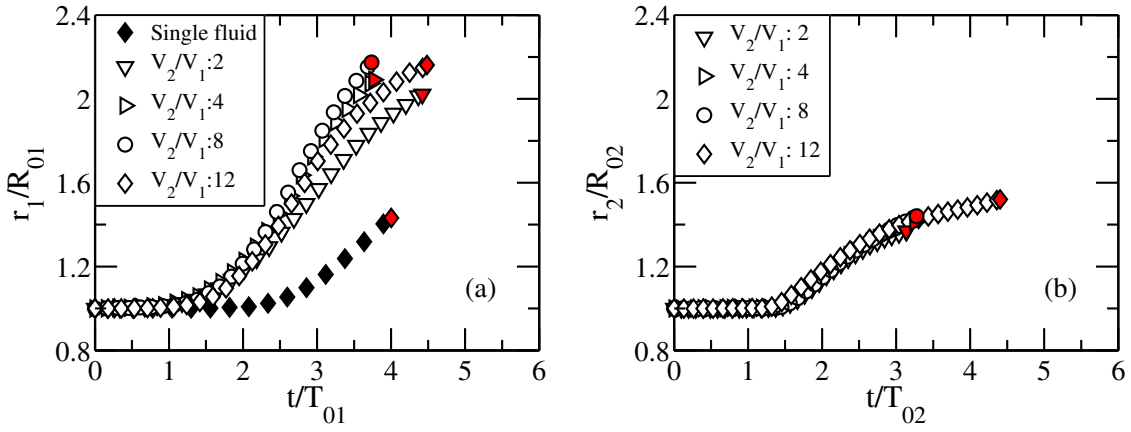

Figure 4.8: Dimensionless time evolution of the drop radius for (a) single and inner- liquid spreading for two-liquid case (for varying volume ratios of the two liquids keeping the inner liquid volume constant), and (b) corresponding outer liquid, at 400 rpm. Radius is scaled by the initial drop radius of the corresponding liquid (R_{01} or R_{02}). Time is scaled by using the corresponding characteristic time for the outer region (T_{01} or T_{02}) [used by Fraysse and Homsy (Phys. Fluids, 1994)]. The red symbol in each curve corresponds to the critical radius of the drop as shown in 2^{nd} row of each column in Fig. 4.6.

Figure 4.8(a) shows that the liquid 1 spreads to a larger extent before developing the instability (i.e. critical radius) when engulfed by liquid 2 on the outside than without. Further, the rate of increase in the spreading radius is also much higher for liquid 1, when within the outer liquid than without. While the spreading rate is nearly constant for the inner liquid for varying volume ratios, the extent of spreading marginally increases with increase in the volume ratio. Note that this increase in the rate of spreading for the inner liquid, cannot be solely attributed to the decrease in the interfacial tension. Because, the interfacial tension for the liquid-liquid interface

stays the same for all the experiments for varying volume ratio V_2/V_1. The fact that the inner liquid spreading data for varying volume ratio cases does not collapse in Fig. 4.8(a) suggests that there is some other parameter which plays a role in determining the spreading rate. Moreover, one interesting thing to notice here is that the spreading radius for the inner liquid starts to increase at an earlier time as compared to the single liquid case. The dimensionless time at which it starts to increase is close to that of the outer liquid (See Fig. 4.8(b)). This suggests that the spreading rate of the inner liquid is affected by the presence of the outer liquid. The increased spreading rate for the inner liquid can be attributed to two factors: (i) the lower value of the interfacial tension and (ii) the drag experienced by the inner liquid due to the faster moving outer liquid causing the inner liquid to move faster along with. The relative contribution of these two factors in the observed increase in the spreading rate is, however, not possible to estimate. This faster spreading rate of inner liquid as compared to outer liquid leads to merging of the contact lines, and therefore, the fingers, for the lowest volume ratio studied here (See Fig 4.7). On the other hand, the data collapse observed for outer liquid in Fig. 4.8(b) is in accordance with results observed for single liquid.[46]

The above experimental data was compared for the axisymmetric spreading of inner liquid for two different V_2/V_1 with the corresponding data obtained from our simulation (See Fig. 4.9). The fluid property ratios and rotational speed provided in the simulation are the same as our experiments. Parabolic initial shapes matching with our initial experimental condition are provided as initial condition for the simulation. Both qualitative and quantitative discrepancies are observed in the spreading rate. As stated earlier, our simulation assumes the liquids to be fully wetting which is incorporated using a precursor layer model. Both the liquids used in our experiments are, however, partially wetting resulting in the observed discrepancy.

Figure 4.10 shows the evolution of the width of the annular region between the two contact lines ΔR $(r_2(t) - r_1(t))$, which is non-dimensionalized using the cube root of the difference between the initial volumes of the two liquids. From Fig. 4.10, it is clear that dimensionless ΔR decreases with time for the lowest possible volume ratio

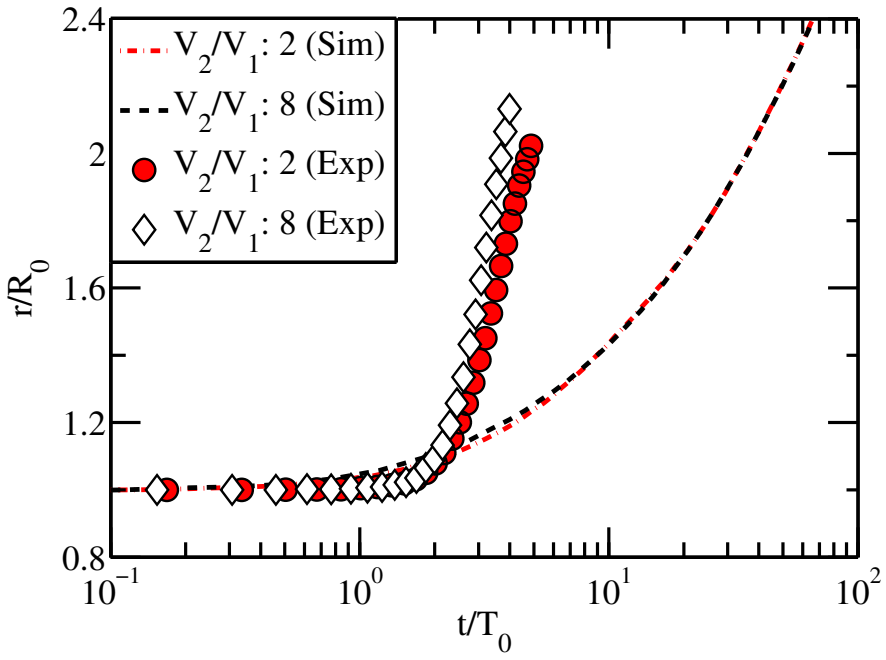

Figure 4.9: Comparison of axisymmetric spreading data obtained from experiments with our simulation. The fluid property ratios and rotational speed are taken to be the same as our experiments. Parabolic initial shapes matching with our initial experimental condition are provided as initial condition for the simulation.

studied ($V_2/V_1 = 2$). This suggests that the inner liquid spreads faster as compared to the outer liquid and eventually merges with the outer contact line, resulting in the decrease in ΔR. In addition, with increase in V_2/V_1, the rate of decrease gets slower till it becomes almost negligible for $V_2/V_1 = 8$. Furthermore, for the highest V_2/V_1, as the outer contact line is much further than the inner one, it simply seems to move away and the inner liquid cannot reach to that leading to the observed increase in the value of ΔR.

4.3.2 Instability characteristics

The instability behavior for all cases is discussed next. Figure 4.11 shows the variation of critical radius (R_{c1}), and the corresponding number of fingers (N_{f1}) (as counted from the images) formed at the onset of instability for different volume ratios studied. Also included is the data for inner liquid, but while spreading in air (red symbols in Fig. 4.11). It does not spread to a larger extent due to its higher surface tension

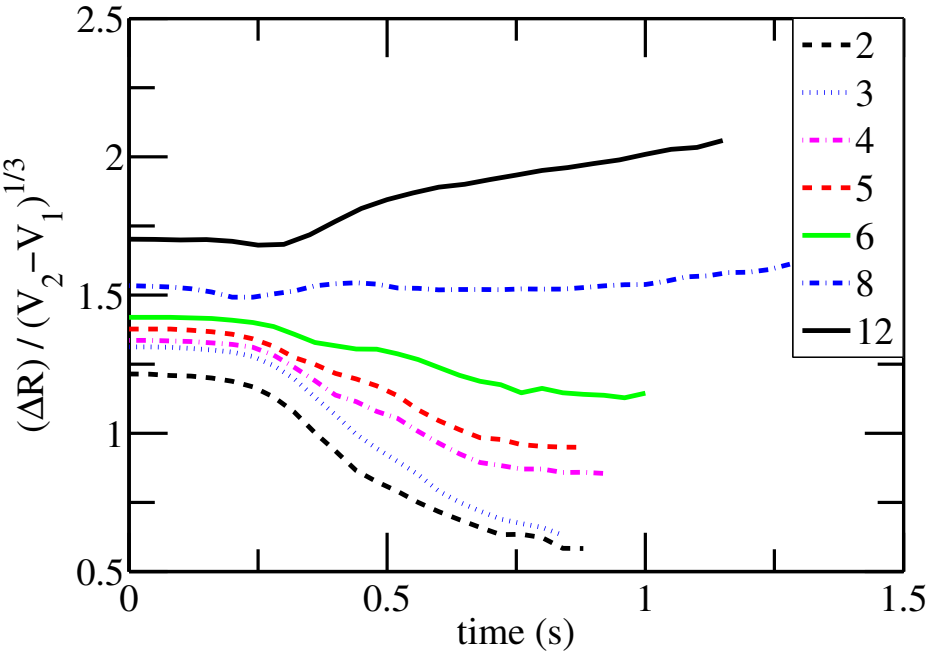

Figure 4.10: Dimensionless width of the annular region between the two contact lines, ΔR $(r_2(t) - r_1(t))$ as function of time. ΔR is non-dimensionalized using the cube root of the difference between the initial volumes of the two liquids. The data is presented for all V_2/V_1 studied.

and, thus, develops instabilities at much earlier times and at a lower R_{c1}, leading to the formation of very small number of fingers. The same liquid, when enclosed by outer liquid, due to its lower interfacial tension, spreads to a larger extent (R_{c1}) before developing instability and forms more number of fingers. Note that larger the perimeter of the spreading drop, higher the number of fingers formed. Further, the number of finger remain constant for all volume ratios, which is expected, given the constant interfacial tension. The spreading of outer liquid without the presence of inner liquid (not shown), yields identical behavior to that obtained with the presence of inner liquid suggestive that the behavior is governed solely by its air-liquid surface tension and not by the liquid it encloses.

We next discuss time evolution of fingers for different cases as shown in Fig. 4.12. The number of fingers for outer as well as inner liquid continue to increase with time, while keeping the base radius nearly constant (See images in Fig. 4.6, rows 2 to 3). This behavior has also been observed previously[46] and can be attributed to

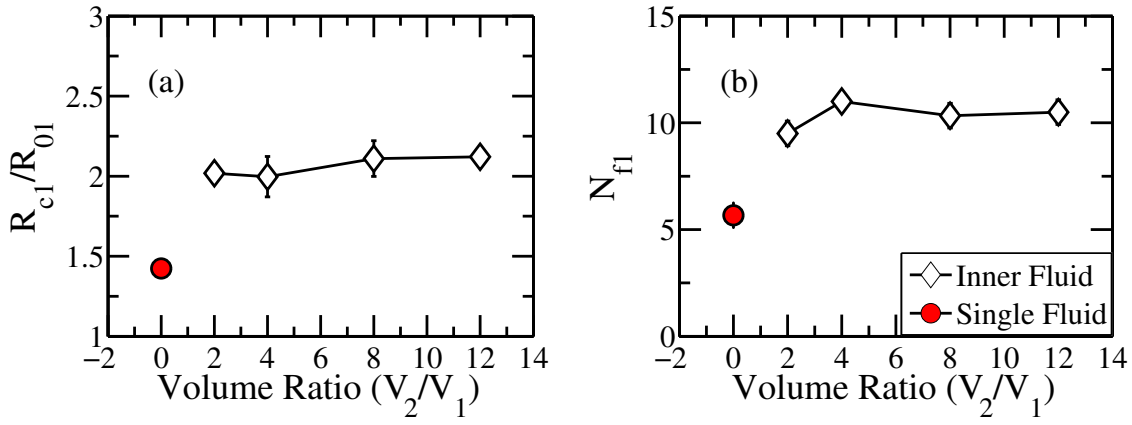

Figure 4.11: (a) Critical radius (R_{c1}), and (b) number of fingers (N_{f1}) of the inner liquid as a function of volume ratio of the two liquids (V_2/V_1). Red circle represents liquid 1 (glycerol) spreading in air, i.e. when $V_2 = 0$.

secondary fingers breaking from the liquid and growing eventually. For the lowest value of V_2/V_1 studied, given the faster spreading rate of inner liquid, it approaches the slowly spreading outer liquid and eventually its instability behavior follows that of outer liquid with the number of fingers same for both cases. Actually, the fingers from inner liquid protrude those of outer liquid with the two liquids now moving outwards through the fingers together.

This whole transformation is very well captured through the images shown in Fig. 4.13 taken at specific times for $V_2/V_1 = 2$ and represented, respectively, by red symbols in Fig. 4.12(a). The images have been slightly modified to remove the background plate so as to emphasize only on the moving contact lines. Note that the wavy nature of the inner liquid-liquid interface is nearly identical to the outer air-liquid interface as shown in Fig. 4.13(e). Note also, that this merging is not instantaneous, but very sequential with the instability behavior of inner liquid changing continuously so as to eventually approach that of the outer liquid. With increasing volume ratio this effect diminishes, that is the fingers of inner liquid keep on increasing, but the outer liquid moves progressively further away so as to have lesser and lesser influence on the instability of inner liquid. Eventually, the two liquids spread nearly independently of each other at the largest volume ratio studied. Curiously though, for large enough volume ratios, a very interesting behavior is observed which we discuss at the end of

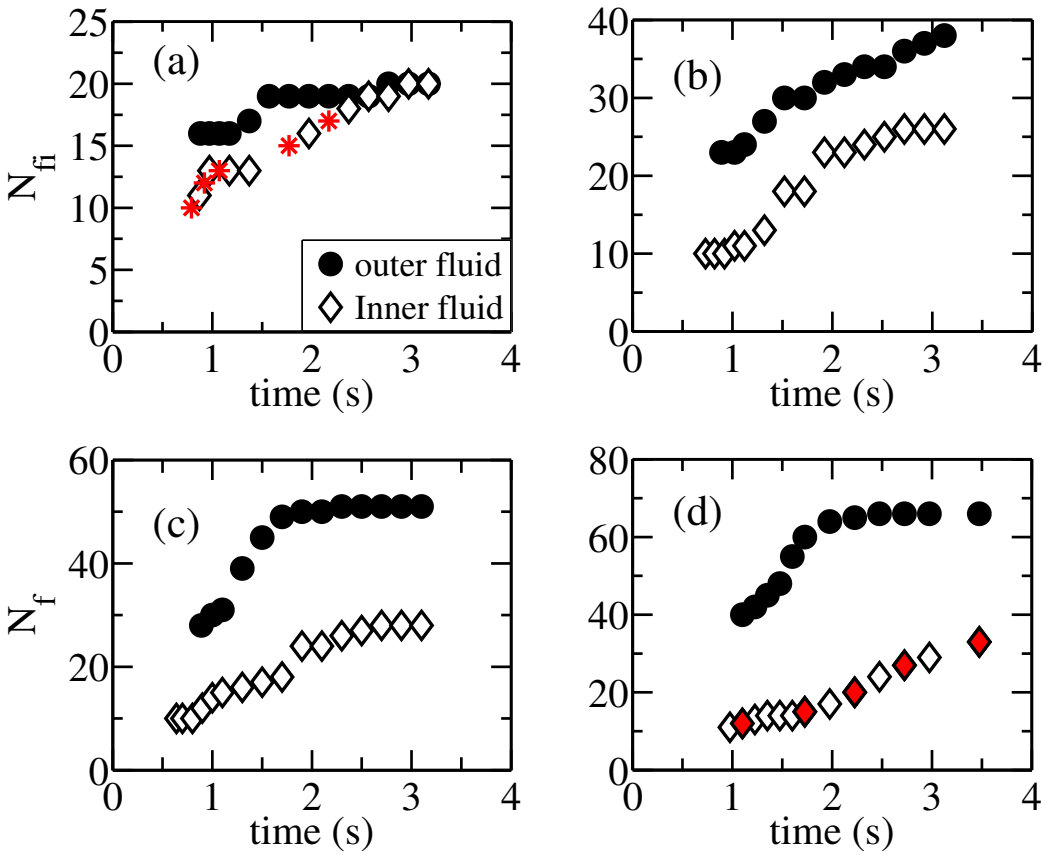

Figure 4.12: N_f as a function of time for V_2/V_1 = (a) 2, (b) 4, (c) 8, and (d) 12, respectively, keeping V_1 constant. Red symbols (*) in (a) represent the spreading state for $V_2/V_1 = 2$ captured in terms of images shown in Fig. 4.13.

this section.

We now compare the experimentally observed N_f with the theoretical prediction using the following expression based on linear stability analysis and which is well established in the literature[46]

$$N_f \approx \frac{\pi}{7} R_c^2 \left(\frac{\pi \rho \omega^2}{\gamma \Omega} \right)^{1/3} \tag{4.1}$$

where, ρ is the liquid density, ω is the disc angular speed, γ is the liquid surface tension and Ω is the liquid volume. The value of R_c is determined from the experimental data. The value of γ is taken to be the surface tension of the liquid when it is spreading in air and its interfacial tension when enclosed and spreading within another liquid. Figure 4.14 shows the comparison of the experimentally determined number of fingers

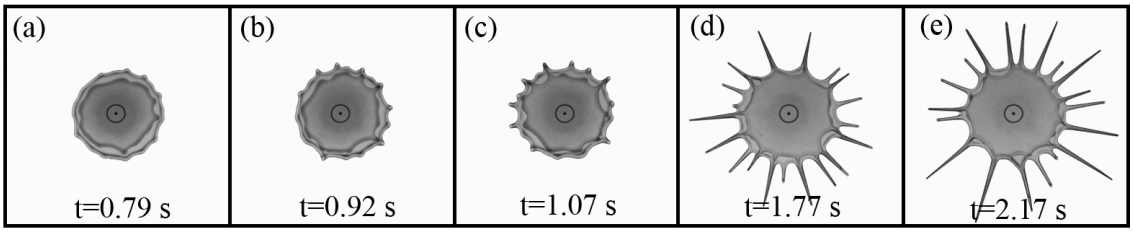

Figure 4.13: Snapshots showing the fingering in both the liquids for $V_2//V_1 = 2$. The time corresponding to each snapshot is also shown. The background (plate surface outside the spreading area) is filled with white color to precisely demonstrate the spreading of the two liquids.

(N_f) with those predicted using the above equation.

Glycerol (single fluid) while spreading in presence of air interface, develops fingers at the outer circumference. The wavelength of instability (λ) and the number of fingers (N_f) are purely governed by the surface tension of the liquid, which is accounted for in the linear stability theory (LSA). Therefore, the data for single liquid shows linear correlation with the predictions of LSA, however, with an offset. The same behavior is observed for the outer liquid (castor oil) which is spreading in presence of air, though enclosing the inner liquid. This can be expected, given that eq. 4.1, as obtained from linear stability analysis is valid only for completely wetting liquids, while the liquids used in this work are partially wetting. However, the theory overpredicts the number of fingers for the inner liquid (open symbols) when enclosed by the outer liquid (i.e. for the liquid-liquid-solid contact line). The number of fingers obtained from the experiments is equivalent to the wave number of instability. We provide a theoretical justification for the observed decrease in the experimentally observed number of fingers (i.e. lowering in the wave number) as compared to the theory, when a fluid spreads in presence of an outer liquid-liquid interface. We have performed a theoretical linear stability analysis to derive an expression for the wave number, and compare it with the wave number for single fluid instability, the analytical derivation and proof for which is provided in the next section.

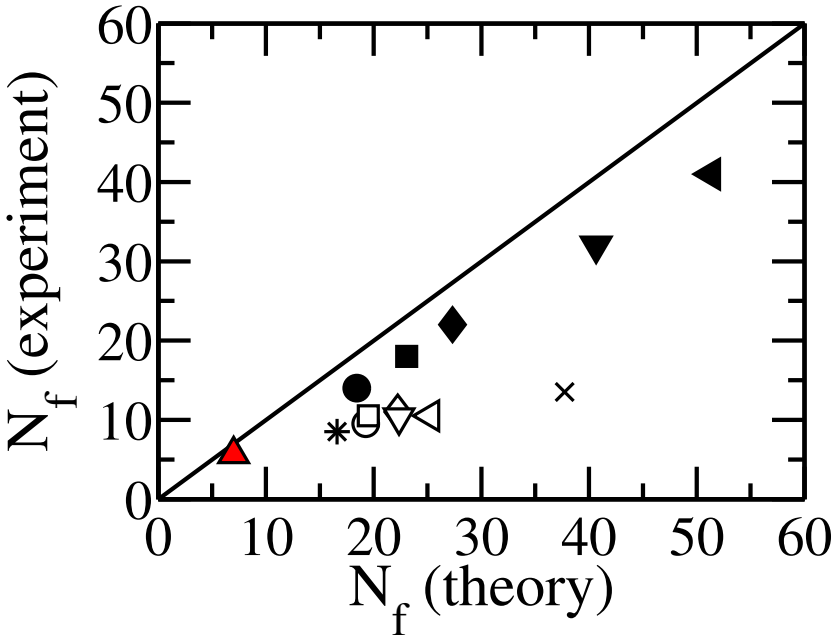

Figure 4.14: Comparison of N_f observed in experiments with that of N_f obtained using linear stability theory provided by Fraysse and Homsy (Phys. Fluids, 1994). The circle, square, diamond, downward-pointing triangle, and left pointing triangle correspond to $V_2/V_1 = 2, 3, 4$, 8, and 12 respectively, for $V_1 = 0.5mL$. Corresponding filled symbols represent the data for outer liquid. The filled red circle correspond to the data for inner liquid spreading in absence of the outer liquid. The star and the upward pointing triangle (open symbols) correspond to the inner liquid data for $V_2/V_1 = 12$ at 300 and 500 rpm, respectively.

4.3.3 Linear Stability Analysis (for small σ)

As discussed in Chapter 2, when a fluid flows on a spinning disc, it forms a small capillary ridge near the contact line and a flat thin film at the center. The region away from the contact line is called outer region and the region close to the contact line is called inner region. The contact line instability for the inner region for thin film flows involving single Newtonian liquids has been discussed in detail by several authors.[22,59,62] Here, we discuss the case of inner liquid which is moving in presence of another viscous liquid (not in air). A linear stability analysis is carried out to study the stability of the inner liquid capillary ridge in two-layer spin coating flow. The theory is valid under certain assumptions: (i) the surface to interfacial ratio ($\sigma = \sigma_2/\sigma_1$) is assumed to be small, (ii) the liquids are assumed to be fully wetting

and, thus, the contact line singularity is relieved by using a precursor layer model, (iii) the capillary ridges of both the inner and outer liquid lay on top of each other, and the contact line of the outer liquid and corresponding capillary ridge is assumed to be far away, and (iv) the thickness of the upper layer liquid is assumed to be small so that the capillary ridges of both the interfaces are close enough. Here, we have extended the analysis of Spaid and Homsy[22] for two-layer thin film flow corresponding to our experiments. The general equations governing the evolution of two layers on a spinning disk are provided in Chapter 3. As discussed by several authors, the flow in the inner region for thin film flow driven by centrifugal force is analogous to thin film flow driven by gravity. Therefore, for a simplicity in the derivation of linear stability equations, in the section below, evolution equations are presented for the two layers flowing down an inclined plane. These governing equations will, then, be used for the stability analysis.

4.3.3.1 Derivation of Two-layer Evolution Equations

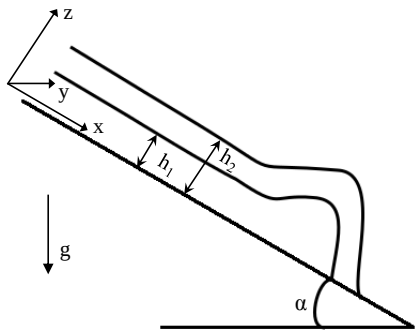

Figure 4.15: Schematic of two-layer thin-film flow on an inclined plane.

The system under consideration consists of two incompressible and immiscible Newtonian fluids; fluid 1 having density $\tilde{\rho}_1$, surface tension $\tilde{\sigma}_1$, and dynamic viscosity $\tilde{\eta}_1$, and fluid 2 having density $\tilde{\rho}_2$, liquid-liquid interfacial tension $\tilde{\sigma}_2$, and dynamic viscosity $\tilde{\eta}_2$, respectively. The layer of fluid 2 is placed on the layer of fluid I and both are placed on an inclined plane and allowed flow under gravity as shown in Fig. 4.15. The layer of fluid 2 is surrounded by air which is at a constant ambient pressure but

exerts no shear stress on the fluid-air interface. Throughout this chapter, the dimensional variables have tilde, $\tilde{(.)}$, over them whereas the corresponding dimensionless variables are denoted without tilde, (.) and vector quantities are represented in bold italics. Hereafter, the layer of fluid present in fluid 2 is referred to as upper layer, and fluid 1 is referred to as lower layer. For mathematical convenience, we use the Cartesian coordinate system $(\tilde{x}, \tilde{y}, \tilde{z})$ as shown in the Fig. 4.15. At any point along the radial direction, the shape of the liquid-liquid interface and the liquid-air interface are denoted by $\tilde{z} = \tilde{h}^{(1)}(\tilde{x}, \tilde{y}, \tilde{t})$, and $\tilde{z} = \tilde{h}^{(2)}(\tilde{x}, \tilde{y}, \tilde{t})$, respectively [see Fig. 4.15]. The isothermal flow of fluid in each of the layers is governed by Navier-Stokes equation and continuity equation:

$$\tilde{\rho_i}\left(\frac{\partial \tilde{\boldsymbol{u}}^{(i)}}{\partial \tilde{t}} + \tilde{\boldsymbol{u}}^{(i)}.\tilde{\nabla}\tilde{\boldsymbol{u}}^{(i)}\right) = -\tilde{\nabla}\tilde{P}^{(i)} + \tilde{\eta_i}\tilde{\nabla}^2\tilde{\boldsymbol{u}}^{(i)} + \tilde{\rho_i}\tilde{\boldsymbol{g}}, \tag{4.2}$$

$$\tilde{\nabla} \cdot \tilde{\boldsymbol{u}}^{(i)} = 0, \tag{4.3}$$

where $\tilde{\boldsymbol{u}}^{(i)} = (\tilde{u}^{(i)}, \tilde{v}^{(i)}, \tilde{w}^{(i)})$ is the velocity of the fluid in the i^{th} layer, and $\tilde{\boldsymbol{g}}$ is the gravity vector pointing downwards as shown in the Fig. 4.15. The above equations are non-dimensionalized with appropriate scales as follows: length of the inclined plane, L is the length scale in the flow direction; initial mean film thickness, H_0 is the length scale in the vertical direction; U_0 is the velocity scale in the flow direction; W_0 is the velocity scale in the vertical direction, and P_0 is the scale for pressure. The scale for density and viscosity are ρ_0 and η_0, respectively, which for convenience are taken to be the parameters of one of the layer fluids. The non-dimensional form of the above equations in the relevant directions are:

$$\epsilon \cdot Re\left(\frac{\partial u^{(i)}}{\partial t} + u^{(i)} \cdot \nabla u^{(i)}\right) = -\frac{\partial P^{(i)}}{\partial x} + \eta_i \frac{\partial^2 u^{(i)}}{\partial z^2} + 1 + O(\epsilon^2), \tag{4.4}$$

$$\epsilon \cdot Re\left(\frac{\partial v^{(i)}}{\partial t} + u^{(i)} \cdot \nabla v^{(i)}\right) = -\frac{\partial P^{(i)}}{\partial y} + \eta_i \frac{\partial^2 v^{(i)}}{\partial z^2} + O(\epsilon^2), \tag{4.5}$$

$$\epsilon^3 \cdot Re\left(\frac{\partial w^{(i)}}{\partial t} + u^{(i)} \cdot \nabla w^{(i)}\right) = -\frac{\partial P^{(i)}}{\partial z} - B + O(\epsilon^3), \tag{4.6}$$

$$\frac{\partial u^{(i)}}{\partial x} + \frac{\partial v^{(i)}}{\partial y} + \frac{\partial w^{(i)}}{\partial z} = 0, \tag{4.7}$$

where $\eta_i = \tilde{\eta}_i/\eta_0$, and $\rho_i = \tilde{\rho}_i/\rho_0$ are the dimensionless viscosity and density, respectively. The velocities in the flow and perpendicular directions are $\tilde{u}^{(i)}$ and $\tilde{v}^{(i)}$, respectively. $Re = \rho_0 U_0 L_0/\eta_0$ is the Reynolds number, $B = \rho_0 g H_0^3/\eta_0 L_0 U_0$ is the Bond number, and $\epsilon = H_0/L_0$ is the aspect ratio. In each of the layers, flow is governed by the balance between the centrifugal force and the viscous force that gives the radial velocity scale as $U_0 = \rho_0 \omega^2 L_0 H_0^2/\eta_0$, and the vertical velocity scale as $W_0 = U_0 H_0/L_0$. Here, $\nabla = L_0.\tilde{\nabla}$ is the dimensionless gradient operator. The pressure scale is $P_0 = \rho_0 \omega^2 L_0^2$, and the time scale is $T = L_0/U_0$.

The Reynolds number associated with the flow is assumed to be very small so that inertial effects are negligible. Moreover, we assume that the film height is small and the gravitational effects are negligible ($B \approx 0$). The spreading film is sufficiently thin that allows use of the standard lubrication assumptions: $\epsilon \ll 1$ and $Re.\epsilon \ll 1$. Using lubrication assumption, Eqs. (4.4)-(4.6) are simplified as:

$$0 = -\frac{\partial P^{(i)}}{\partial x} + \eta_i \frac{\partial^2 u^{(i)}}{\partial z^2} + 1, \tag{4.8}$$

$$0 = -\frac{\partial P^{(i)}}{\partial y} + \eta_i \frac{\partial^2 v^{(i)}}{\partial z^2}, \tag{4.9}$$

$$0 = -\frac{\partial P^{(i)}}{\partial z} - B, \tag{4.10}$$

$$0 = \frac{\partial u^{(i)}}{\partial x} + \frac{\partial v^{(i)}}{\partial y} + \frac{\partial w^{(i)}}{\partial z}. \tag{4.11}$$

These equations are subjected to the following boundary conditions:

$$u^{(1)} = v^{(1)} = w^{(1)} = 0 \quad \text{at } z = 0, \tag{4.12}$$

$$u^{(1)} = u^{(2)} \quad \text{and} \quad v^{(1)} = v^{(2)} \quad \text{at } z = h^{(1)}(x, y, t), \tag{4.13}$$

$$\eta_1 \frac{\partial u^{(1)}}{\partial z} = \eta_2 \frac{\partial u^{(2)}}{\partial z} \quad \text{and} \quad \eta_1 \frac{\partial v^{(1)}}{\partial z} = \eta_2 \frac{\partial v^{(2)}}{\partial z} \quad \text{at } z = h^{(1)}(x, y, t), \tag{4.14}$$

$$\eta^{(2)} \frac{\partial u^{(2)}}{\partial z} = 0 \quad \text{and} \quad \eta^{(2)} \frac{\partial v^{(2)}}{\partial z} = 0 \quad \text{at } z = h^{(2)}(x, y, t), \tag{4.15}$$

$$P^{(1)} = p_0 - C_1 \nabla^2 h^{(1)} - C_2 \nabla^2 h^{(2)} \quad \text{at } z = h^{(1)}(x, y, t), \tag{4.16}$$

$$P^{(2)} = p_0 - C_2 \nabla^2 h^{(2)} \quad \text{at } z = h^{(2)}(x, y, t), \tag{4.17}$$

where $C_i = \epsilon^3 \sigma_i / \eta_0 U_0$ is the inverse Capillary number, p_0 is the atmospheric pressure, and $\nabla^2 = \frac{\partial^2}{\partial x^2} + \frac{\partial^2}{\partial y^2} + \frac{\partial^2}{\partial z^2}$. Equation (4.12) represents the no-slip condition at the planar substrate. Equations (4.13) and (4.14) represent the continuity of velocity and tangential stress at liquid-liquid interface, respectively. Equation (4.15) represents the zero tangential stress at the liquid-air interface, and Eqs. (4.16) and (4.17) represent the normal stress condition that incorporates the surface tension force at the respective surface.

From here on wards, the scales $\rho_0 = \rho_1$, and $\eta_0 = \eta_1$ are chosen to be the properties of the lower layer fluid. The velocities in the flow direction $u^{(1)}$ and $u^{(2)}$ are obtained by integrating Eq. (4.8) for both the layers and applying boundary conditions given by Eqs. (4.12)-(4.17). Similarly, the velocities in the direction perpendicular to the flow $v^{(1)}$ and $v^{(2)}$ are obtained by integrating Eq. (4.9) for both the layers and applying boundary conditions given by Eqs.(4.12)-(4.17).

Integrating the continuity equation Eq. (4.11) for both the layers and using the kinematic condition gives the usual mass balance as

$$\frac{\partial h^{(1)}}{\partial t} + \nabla \cdot Q_1 = 0 \ , \tag{4.18}$$

$$\frac{\partial h^{(2)}}{\partial t} + \nabla \cdot Q_2 = 0 \ , \tag{4.19}$$

where, the flux vectors Q_1 and Q_2 are:

$$Q_1 = \int_0^{h^{(1)}} u^{(1)} dz \ \hat{i} + \int_0^{h^{(1)}} v^{(1)} dz \ \hat{j}, \tag{4.20}$$

$$Q_2 = \int_{h^{(1)}}^{h^{(2)}} u^{(2)} dz \; \hat{i} + \int_{h^{(1)}}^{h^{(2)}} v^{(2)} dz \; \hat{j} \; . \tag{4.21}$$

The quantities Q_1 and Q_2 are the total fluxes across the layer of fluid 1 and fluid 2 respectively. Using Eq. (4.42) and Eq. (4.43), the x and y components of the fluxes Q_1 and Q_2 are obtained as:

$$\begin{aligned} Q_{1x} =& \frac{h_1^3}{3}\left(C\frac{\partial}{\partial x}\left(\sigma\nabla^2 h_2 + \nabla^2 h_1\right) + 1\right) \\ &+ \frac{h_1^2(h_2 - h_1)}{2}\left(\sigma C\frac{\partial}{\partial x}\left(\nabla^2 h_2\right) + \rho\right), \end{aligned} \tag{4.22}$$

$$\begin{aligned} Q_{1y} =& \frac{h_1^3}{3}\left(C\frac{\partial}{\partial y}\left(\sigma\nabla^2 h_2 + \nabla^2 h_1\right)\right) \\ &+ \frac{h_1^2(h_2 - h_1)}{2}\left(\sigma C\frac{\partial}{\partial y}\left(\nabla^2 h_2\right)\right). \end{aligned} \tag{4.23}$$

$$\begin{aligned} Q_{2x} =& \frac{h_1^2(h_2 - h_1)}{2}\left(C\frac{\partial}{\partial x}\left(\sigma\nabla^2 h_2 + \nabla^2 h_1\right) + 1\right) \\ &+ \left(\frac{(h_2 - h_1)^3}{3\eta} + h_1(h_2 - h_1)^2\right)\left(\sigma C\frac{\partial}{\partial x}\left(\nabla^2 h_2\right) + \rho\right) \end{aligned} \tag{4.24}$$

$$\begin{aligned} Q_{2y} =& \frac{h_1^2(h_2 - h_1)}{2}\left(C\frac{\partial}{\partial y}\left(\sigma\nabla^2 h_2 + \nabla^2 h_1\right)\right) \\ &+ \left(\frac{(h_2 - h_1)^3}{3\eta} + h_1(h_2 - h_1)^2\right)\left(\sigma C\frac{\partial}{\partial y}\left(\nabla^2 h_2\right)\right). \end{aligned} \tag{4.25}$$

Now, the two equations describing the time evolution of the liquid-liquid interface and the free surface with respect to spatial coordinates x and y are obtained as:

$$\begin{aligned} &\frac{\partial h_1}{\partial t} + \frac{\partial}{\partial x}\left\{\frac{h_1^3}{3}\left(C\frac{\partial}{\partial x}\left(\sigma\nabla^2 h_2 + \nabla^2 h_1\right) + 1\right)\right. \\ &\qquad \left. + \frac{h_1^2(h_2 - h_1)}{2}\left(\sigma C\frac{\partial}{\partial x}\left(\nabla^2 h_2\right) + \rho\right)\right\} \end{aligned}$$

$$+\frac{\partial}{\partial y}\left\{\frac{h_1^3}{3}\left(C\frac{\partial}{\partial y}\left(\sigma\nabla^2 h_2+\nabla^2 h_1\right)\right)\right.$$
$$\left.+\frac{h_1^2(h_2-h_1)}{2}\left(\sigma C\frac{\partial}{\partial y}\left(\nabla^2 h_2\right)\right)\right\}=0, \tag{4.26}$$

$$\frac{\partial h_2}{\partial t}+\frac{\partial}{\partial x}\left\{\frac{h_1^2(h_2-h_1)}{2}\left(C\frac{\partial}{\partial x}\left(\sigma\nabla^2 h_2+\nabla^2 h_1\right)+1\right)\right.$$
$$\left.+\left(\frac{(h_2-h_1)^3}{3\eta}+h_1(h_2-h_1)^2\right)\left(\sigma C\frac{\partial}{\partial x}\left(\nabla^2 h_2\right)+\rho\right)\right\}$$
$$+\frac{\partial}{\partial y}\left\{\frac{h_1^2(h_2-h_1)}{2}\left(C\frac{\partial}{\partial y}\left(\sigma\nabla^2 h_2+\nabla^2 h_1\right)\right)\right.$$
$$\left.+\left(\frac{(h_2-h_1)^3}{3\eta}+h_1(h_2-h_1)^2\right)\left(\sigma C\frac{\partial}{\partial y}\left(\nabla^2 h_2\right)\right)\right\}=0. \tag{4.27}$$

where, $\eta=\eta_2/\eta_1$, $\sigma=\sigma_2/\sigma_1$, and $\rho=\rho_2/\rho_1$. The quantity $\epsilon=H_0/R_0$ is the aspect ratio, where, H_0, R_0, are the length scales in z and x directions, respectively. U_0 is the velocity scale in the x direction, which is defined as $U_0=\rho_1 g H_0^2/\eta_1$. The quantity, $C_i=\epsilon^3\sigma_i/\eta_1 U_0$, is the inverse Capillary number, and ∇^2 is the two-dimensional Laplacian operator in Cartesian coordinates.

Using equations 4.26 and 4.27, the equations for the evolution of inner liquid-liquid interface, and free surface, in the inner region are obtained as:

$$\text{Layer-1:}\qquad h_{1\tau}+\frac{\dot{R}_{1F}}{U_1}h_{1\xi}+\nabla.Q_1=0, \tag{4.28}$$

$$\text{Layer-2:}\qquad h_{2\tau}+\frac{\dot{R}_{2F}}{U_2}h_{2\xi}+\nabla.Q_2=0, \tag{4.29}$$

where, $h_i(\xi,y,\tau)$ is the non-dimensional height in the respective layers ($i=1,2$), and ξ is the transformed x coordinate. In the above formulation, the inner liquid contact line is set as the origin and the value of ξ increases as we move towards the center of the spreading inner liquid. The quantity Q_i is the flux in the inner region of respective layers, that is re-scaled in $\xi-y$ coordinate system. The factor $\dot{R}_{iF}/U_i$ represents speed at which the contact line moves relative to the average speed of the inner region, in respective layers, and therefore depends on the contact line model.

For a precursor layer model, it is given by:

$$\frac{\dot{R}_{1F}}{U_1} = \frac{1-b_1^3}{1-b_1}, \quad \text{and} \quad \frac{\dot{R}_{2F}}{U_2} = \frac{1-b_2^3}{1-b_2} \tag{4.30}$$

where, b_1 and b_2 are the precursor layer thicknesses of the inner and outer liquid, respectively. Setting the appropriate value of the factor $\dot{R}_{iF}/U$ for precursor layer condition from eq. 4.30, interface and free surface evolution equations, respectively, for the Newtonian liquids in the inner regions are:

$$\begin{aligned}
&h_{1\tau} + \frac{1-b_1^3}{1-b_1} h_{1\xi} \\
&\quad - \frac{\partial}{\partial \xi}\left\{ h_1^3 \left(\frac{1}{3} - \sigma\Big(h_{2\xi\xi\xi} + h_{2\xi yy}\Big) - h_{1\xi\xi\xi} - h_{1\xi yy} \right) \right. \\
&\qquad \left. + \frac{3h_1^2(h_2-h_1)}{2}\left(\frac{\rho}{3} - \sigma\Big(h_{2\xi\xi\xi} + h_{2\xi yy}\Big) \right) \right\} \\
&\quad + \frac{\partial}{\partial y}\left\{ h_1^3 \left(\sigma\Big(h_{2\xi\xi y} + h_{2yyy}\Big) + h_{1\xi\xi y} + h_{1yyy} \right) \right. \\
&\qquad \left. + \frac{3h_1^2(h_2-h_1)}{2}\left(\sigma\Big(h_{2\xi\xi y} + h_{2yyy}\Big) \right) \right\} = 0,
\end{aligned} \tag{4.31}$$

$$\begin{aligned}
&h_{2\tau} + \frac{1-b_2^3}{1-b_2} h_{2\xi} \\
&\quad - \frac{\partial}{\partial \xi}\left\{ \left(\frac{(h_2-h_1)^3}{\eta} + 3h_1(h_2-h_1)^2 \right)\left(\frac{\rho}{3} - \sigma\Big(h_{2\xi\xi\xi} + h_{2\xi yy}\Big) \right) \right. \\
&\qquad \left. + \frac{3h_1^2(h_2-h_1)}{2}\left(\frac{1}{3} - \sigma\Big(h_{2\xi\xi\xi} + h_{2\xi yy}\Big) - h_{1\xi\xi\xi} - h_{1\xi yy} \right) \right\} \\
&\quad + \frac{\partial}{\partial y}\left\{ \left(\frac{(h_2-h_1)^3}{\eta} + 3h_1(h_2-h_1)^2 \right)\left(\sigma\Big(h_{2\xi\xi y} + h_{2yyy}\Big) \right) \right. \\
&\qquad \left. + \frac{3h_1^2(h_2-h_1)}{2}\left(\sigma\Big(h_{2\xi\xi y} + h_{2yyy}\Big) + h_{1\xi\xi y} + h_{1yyy} \right) \right\} = 0.
\end{aligned} \tag{4.32}$$

Now, the heights of the inner surface and free surface, respectively, are expanded

as:

$$h_1(\xi, y, \tau) = h_{10}(\xi) + \epsilon G_1(\xi) e^{iq_1 y + \beta_1 \tau}$$
$$h_2(\xi, y, \tau) = h_{20}(\xi) + \epsilon G_2(\xi) e^{iq_1 y + \beta_1 \tau} \ . \tag{4.33}$$

Here, h_{10} and h_{20} are base state profiles, q_1 and β_1, respectively, are the azimuthal wave number and growth rate of the instability (i.e., eigen value, that is positive for unstable modes). G_1 and G_2 are respectively, the eigen functions corresponding to the amplitudes of perturbations in the respective layers. Now, substituting the above expanded functional forms of heights from eq. 4.33 in eq 4.31, and collecting terms of $O(\epsilon)$, we get linear stability equations for the capillary ridge in the inner liquid (See eq. 4.34). As we are interested in finding out the reason behind the discrepancies observed in the number of fingers obtained from theory and experiments, for the inner liquid (with and without presence of an outer liquid interface), we will discuss the stability equation only for the inner liquid.

$$\begin{aligned}
&\beta_1 G_1 + \frac{1-b_1^3}{1-b_1} G_{1\xi} \\
&\quad + \frac{\partial}{\partial \xi} \Bigg\{ \Big(G_{1\xi\xi\xi} - q_1^2 G_{1\xi} \Big) h_{10}^3 + \frac{\sigma}{2} \Big(3h_{10}^2 h_{20} - h_{10}^3 \Big) \Big(G_{2\xi\xi\xi} - q_1^2 G_{2\xi} \Big) \\
&\qquad + 3G_1 h_{10}^2 \Big(\sigma h_{20\xi\xi\xi} + h_{10\xi\xi\xi} - \frac{1}{3} \Big) \\
&\qquad + \frac{3}{2} \Big(\sigma h_{20\xi\xi\xi} - \frac{\rho}{3} \Big) \Big(2G_1 \big(h_{10} h_{20} - h_{10}^2 \big) + \frac{h_{10}^2}{2} (G_2 - G_1) \Big) \Bigg\} \\
&\quad + \Big(q_1^4 G_1 - q_1^2 G_{1\xi\xi} \Big) \Big(h_{10}^3 + \sigma \frac{3}{2} h_{10}^2 h_{20} \Big) + \sigma h_{10}^3 \Big(q_1^4 G_2 - q_1^2 G_{2\xi\xi} \Big) = 0.
\end{aligned} \tag{4.34}$$

For the single fluid, the stability equation is provided by[22]. We provide this equation below for an ease in the comparison.

$$\beta_0 G_0 + \frac{1-b^3}{1-b} G_{0\xi}$$

$$+\frac{\partial}{\partial\xi}\left\{\left(G_{0\xi\xi\xi}-q^2G_{0\xi}\right)h_0^3-3G_0\left[h_0^2\left(1-h_{0\xi\xi\xi}\right)\right]\right\}$$
$$+h_0^3\left(q^4G_0-q^2G_{0\xi\xi}\right)=0. \tag{4.35}$$

where, β_0, G_0, q and b are respectively, growth rate, eigen function corresponding to the amplitude of perturbation, wave number and precursor layer thickness for the single fluid spreading with a free surface.

From the governing linear stability equations, the dispersion relation can be obtained by plotting data for growth rate and wave number. The dispersion relation for single fluid case is provided by Spaid and Homsy [22]. Here, we intend to compare the wave number corresponding to the most unstable mode in case of single liquid spreading with a free surface and the same liquid spreading with an outer liquid-liquid interface. This can achieved by finding the slope of the dispersion curve and equating it to zero to find the wave number corresponding to maximum growth rate (β). In order to obtain the slope of this curve, we, find the derivative of the stability equation, with respect to the wave number.

Now, for the single liquid case, taking the derivative of stability equation (eq. 4.35) with respect to the wave number (q) gives:

$$\frac{\mathrm{d}\beta_0}{\mathrm{d}q}=\frac{1}{G_0}\left[\frac{\partial}{\partial\xi}\left(2qh_0^3G_{0\xi}\right)+h_0^3\left(2qG_{0\xi\xi}-4q^3G_0\right)\right]. \tag{4.36}$$

For the inner layer fluid taking the derivative of equation 4.34 with respect to q_1 will give:

$$\frac{\mathrm{d}\beta_1}{\mathrm{d}q_1}=\frac{1}{G_1}\left\{\frac{\partial}{\partial\xi}\left(2q_1G_{1\xi}h_{10}^3+\sigma q_1G_{2\xi}\left(3h_{10}^2h_{20}-h_{10}^3\right)\right)\right.$$
$$+\sigma h_{10}^3\left(2qG_{2\xi\xi}-4q^3G_2\right)$$
$$\left.+\left(h_{10}^3+\frac{3\sigma h_{10}^2h_{20}}{2}\right)\left(2qG_{1\xi\xi}-4q_1^3G_1\right)\right\}. \tag{4.37}$$

To deduce the slope of the maxima point in the dispersion curve, we set the right hand of eq. 4.36 and eq. 4.37 to zero and integrate the resulting equations over the

entire domain (i.e from $-\infty$ to $+\infty$), for single-fluid and inner-fluid, respectively. The resulting expression for wave number of instability for both single- and inner-fluid are presented below.

For single fluid, the wave number (q) is found to be :

$$q^2 = \frac{1}{2} \frac{\int_{-\infty}^{+\infty} h_0^3 G_{0\xi\xi} \, \mathrm{d}\xi}{\int_{-\infty}^{+\infty} h_0^3 G_0 \, \mathrm{d}\xi} \quad \sim \quad \frac{1}{4} \tag{4.38}$$

The above expression implies that:

$$\frac{\int_{-\infty}^{+\infty} h_0^3 G_{0\xi\xi} \, \mathrm{d}\xi}{\int_{-\infty}^{+\infty} h_0^3 G_0 \, \mathrm{d}\xi} \quad \sim \quad \frac{1}{2} \quad \text{or} \quad \int_{-\infty}^{+\infty} h_0^3 G_{0\xi\xi} \, \mathrm{d}\xi \quad \sim \quad 2 \int_{-\infty}^{+\infty} h_0^3 G_0 \, \mathrm{d}\xi \tag{4.39}$$

Equation 4.38 is equated to 1/4 because, the most unstable wave number for single fluid case has been reported to be ~ 0.5 (See FIG. 4 of Spaid and Homsy).[22]

For inner layer fluid, the expression for wave number is found to be:

$$q_1^2 = \frac{1}{2} \frac{\int_{-\infty}^{+\infty} h_{10}^3 G_{1\xi\xi} \, \mathrm{d}\xi + \sigma \int_{-\infty}^{+\infty} \left(\frac{3}{2} h_{10}^2 h_{20} G_{1\xi\xi} + h_{10}^3 G_{2\xi\xi} \right) \mathrm{d}\xi}{\int_{-\infty}^{+\infty} h_{10}^3 G_1 \, \mathrm{d}\xi + \sigma \int_{-\infty}^{+\infty} \left(\frac{3}{2} h_{10}^2 h_{20} G_1 + h_{10}^3 G_2 \right) \mathrm{d}\xi} \tag{4.40}$$

For small but finite surface tension ratio (σ), we expand the the base state and eigen function of the perturbation for the inner layer liquid as:

$$\begin{aligned} h_{10} &= h_0 + \sigma h_{11} + \sigma^2 h_{12} + \ldots \\ G_1 &= G_0 + \sigma G_{11} + \sigma^2 G_{12} + \ldots \end{aligned} \tag{4.41}$$

where, h_0 and G_0 are, respectively, the base state profile and amplitude of perturbation (eigen function) for the stability analysis of single fluid,[22] and h_{11}, h_{12}, G_{11} and G_{12} are arbitrary positive functions.

Inserting eq. 4.41 in eq. 4.40 and collecting terms of $O(\sigma)$ and neglecting higher order terms of $O(\sigma^2)$ and above, we get:

$$q_1^2 = \frac{1}{2}\frac{\int_{-\infty}^{+\infty} h_0^3 G_{0\xi\xi}\mathrm{d}\xi + \sigma \int_{-\infty}^{+\infty}\left[\left(\frac{3}{2}h_0^2 h_{20} + 3h_0^2 h_{11}\right)G_{0\xi\xi} + h_0^3 G_{2\xi\xi}\right]\mathrm{d}\xi}{\int_{-\infty}^{+\infty} h_0^3 G_0 \mathrm{d}\xi + \sigma \int_{-\infty}^{+\infty}\left[\left(\frac{3}{2}h_0^2 h_{20} + 3h_0^2 h_{11}\right)G_0 + h_0^3 G_2\right]\mathrm{d}\xi} \tag{4.42}$$

The best check for the correctness is that as $\sigma \to 0$, the expression (See eq. 4.42) for the wave number of inner liquid (two-fluid case) reduces to the expression for q (See eq. 4.38) for single fluid (liquid spreading in air), i.e.

$$\text{As } \sigma \to 0, \quad q_1^2 \to q^2$$

Now, we expand the base state as well as eigen function of the outer liquid in the form as below:

$$\begin{aligned} h_{20} &= h_{10} + f(\xi) \\ &= h_0 + \sigma h_{11} + \sigma^2 h_{12} + \cdots + f(\xi) \\ G_2 &= G_1 + g(\xi) \\ &= G_0 + \sigma G_{11} + \sigma^2 G_{12} + \cdots + g(\xi) \end{aligned} \tag{4.43}$$

where, f and g are arbitrary positive functions.

Now, the final expression for the wave number of instability for the inner liquid corresponding to the maximum growth rate (the most unstable mode), is given by:

$$q_1^2 = \frac{1}{2}\frac{\int_{-\infty}^{+\infty} G_{0\xi\xi} h_0^3 \mathrm{d}\xi + \sigma \int_{-\infty}^{+\infty}\left[\left(\frac{5}{2}h_0^3 + \frac{3}{2}h_0^2 f + 3h_0^2 h_{11}\right)G_{0\xi\xi} + h_0^3 G_{11\xi\xi} + h_0^3 g_{\xi\xi}\right]\mathrm{d}\xi}{\int_{-\infty}^{+\infty} G_0 h_0^3 \mathrm{d}\xi + \sigma \int_{-\infty}^{+\infty}\left[\left(\frac{5}{2}h_0^3 + \frac{3}{2}h_0^2 f + 3h_0^2 h_{11}\right)G_0 + h_0^3 G_{11} + h_0^3 g\right]\mathrm{d}\xi} \tag{4.44}$$

In the above equation for wave number of instability, we have shown that the

increase in the the additional terms present in the numerator (coefficient of σ) will always be lesser than the increase in the additional terms present in the denominator. Note that, the coefficients of all these terms being equal in the numerator and denominator and given the fact that the numerator contains derivative of the positive functions present in the denominator (which will have a positive part and a negative part), q_1^2 for inner liquid in two-fluid spreading will be lesser than that of q^2 for single fluid (See eq. 4.38), i.e.

$$q_1(\text{inner liquid}) \; < \; q(\text{single liquid}) \tag{4.45}$$

In other words, this reduction in the wave number of most unstable mode of the instability for two-fluid indicates a decrease in the value of N_f which is exactly what we observe in our experiments as shown in Fig. 4.14. Having analyzed the incipience of fingering instability, we will now discuss the growth rate of fingers post instability formation.

Figure 4.16 depicts the growth of the fastest moving finger for the inner liquid with the presence of the outer liquid for $V_2/V_1 = 12$ and for the single inner liquid spreading in air (no outer liquid). It is clear that the growth rate of the finger for the inner liquid in presence of outer liquid is slower as compared to the single inner liquid with a free surface (spreading in air interface). This happens because the single fluid (glycerol) is a partially wetting liquid and it likes to spread less and breaks into less number of fingers. The liquid from the central drop, thus, move outward through those fingers at a faster rate. However, for the case of inner fluid in presence of the outer liquid, it spreads more and forms more number of fingers owing to the low interfacial tension. Therefore, the liquid from the central drop of the inner liquid move outward through those fingers, at a slower rate.

As mentioned earlier, for all volume ratios (especially large enough volume ratios) at longer times, a very interesting behavior is observed. Figure 4.17 shows the snapshots of the two-liquid spreading for the largest volume ratio $V_2/V_1 = 12$ studied. At intermediate times (second and third box), the tip of the fingers shows formation of

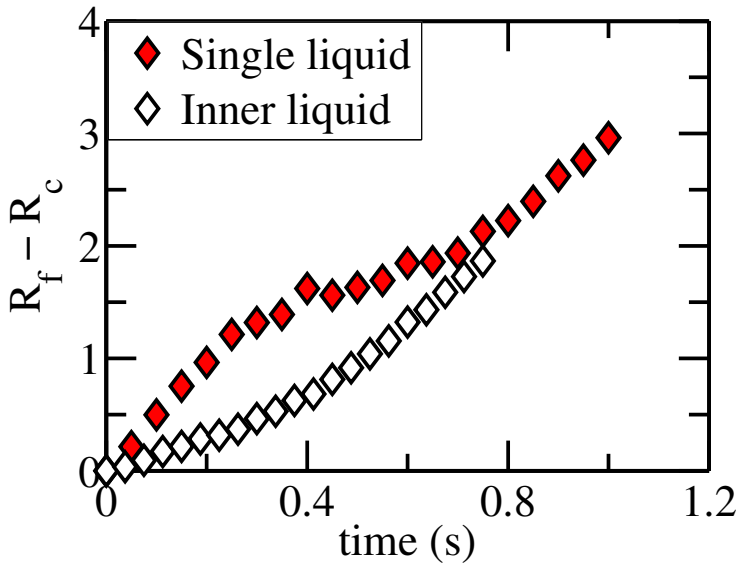

Figure 4.16: Growth of the fastest moving finger as function of time. Open symbols denote data inner liquid spreading in presence of outer viscous liquid for $V_2/V_1 = 12$. Filled symbols correspond to the finger growth for the same inner liquid spreading in presence of air interface.

drop like structures. At even further times (fourth and fifth box), these structures, break away from the fingers, particularly secondary smaller fingers, to move radially as droplets. A more clear picture of this finger break up and droplet formation in case of is shown in Fig. 4.18.

This phenomenon is generally not observed in single liquid spreading and fingering, and thus, seems to be a manifestation of two liquid system studied over here. As noted in previous paragraph, the outer liquid contact line for larger volume ratios is far away from the inner liquid. This allows for the inner liquid film and the emanating fingers (primary as well as secondary) to spread to a significant distance which eventually leads to drop break-up. This drop formation can be linked to the outer co-flowing liquid shearing, pinching and finally squeezing out a drop from the continuously thinning inner liquid or a finger. Such formation of drops with an outer co-flowing liquid squeezing a drop from the inner liquid coming out of the nozzle is well known in the literature and has been studied to a significant extent [89–93] which has led towards analytical expressions for estimating the drop size distribution depending on the liquid flow rates and physical properties. Quantitative estimates about droplet

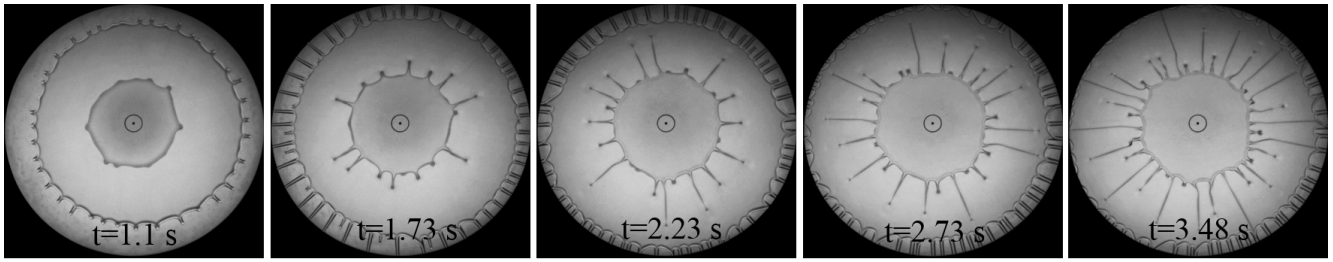

Figure 4.17: Snapshots showing the drop formation from the inner liquid for $V_2/V_1 = 12$. The time corresponding to each snapshot is also shown.

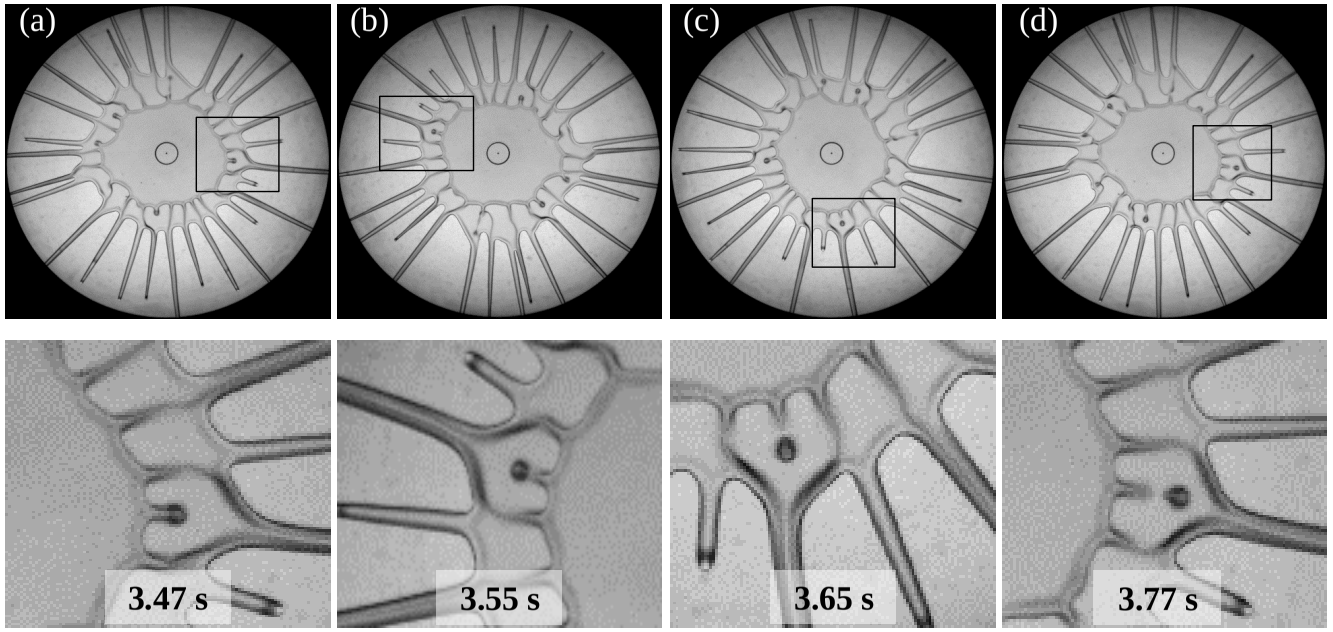

Figure 4.18: Series of images showing finger break up and droplet formation in two-liquid spreading for (V_1 =0.5 ml, $V_2/V_1 = 3$) (row 1, (a)-(d)). The 2nd row shows zoomed in image of a particular finger break up corresponding to each image in first row. The time corresponding to each image is embedded in each image block in 2nd row.

size distribution and their comparison with theoretical expressions is not possible in our current set-up and will form the focus of future work. Comparison of the images shown in Fig. 4.13 and Fig. 4.17 is suggestive of the interplay between two distinct phenomena, viz. instability alignment and drop formation, both unique to a two-liquid spreading system with one of them being dominant depending on the volume ratios of the two liquids, i.e. the proximity between the outer and inner contact lines.

4.4 Conclusions

Simultaneous spreading and ensuing instability behavior of superposed drops of two liquids with different surface tensions is studied experimentally and the results are presented for varying volume ratios of the two liquids. Both qualitative as well as quantitative differences in instability behavior for the single and two-liquids has been observed for the experimental conditions considered here. It is found that the number of fingers which form in case of the two-liquid spreading process for the inner liquid is comparatively higher than the single liquid. Also, the spreading dynamics and onset of instability are significantly altered by the presence of a liquid-liquid interface. After comparison of the experimental results of the liquid spreading in presence of another liquid with the available linear stability theory for predicting the N_f for single liquid spreading, it is found that the the inner liquid data for two-fluid case does not agree with the theory. In fact, the theory overpredicts the number of fingers observed in experiments. A new theory has been derived by using linear stability analysis for small but finite surface to interfacial tension ratio, and it has been found that the presence of outer interface results in lowering in the value of most unstable wave number as compared to single fluid case. This is equivalent to the observed decrease in the number of fingers in our experiments. Furthermore, a newer effect of finger break up and drop formation is also observed experimentally and is not reported elsewhere.

The future work will include analysis of the size distribution of the droplets for varying experimental parameters. However, the results obtained offer a better physi-

cal insight into the phenomenon of two-phase thin film flow instability on a spinning disc and may help to improve the modeling of such flow systems, which are usually based on the simplified 1D axisymmetric transient two-liquid models.

Chapter 5

Fingering instability of a suspension film spreading on a spinning disc

5.1 Introduction

The spreading of a suspension film on a solid surface under an external forcing plays an important role in diverse applications, such as preparation of thin microporous films, polymeric crystals, and micro-spheres for drug delivery etc.[11,94,95] The spreading dynamics of such a film may vary depending on the driving force, viscosity and wetting behavior of the suspending liquid, size of the particles present (colloidal, non-Brownian suspension etc.), density of the particles (settling, buoyant and neutrally buoyant), and concentration of particles present (dilute, semi-dilute, dense suspension). Depending on the particle concentration and the employed driving force, free surface of the spreading film can either get deformed[71] or result in modification of the shape of capillary ridge at the advancing front.[64] Furthermore, the presence of particles in the suspending liquid can exhibit several complexities during spreading and ensuing instability patterns.[64,72,96]

The emergence of a particle-rich ridge on an inclined plane flow of a non-buoyant

particle suspension is investigated using theory as well as experiments.[64,65] The particle-rich ridge is observed to suppress the finger formation in the experiments. The occurrence of this instability can be understood based on the balance between particle settling through gravity and re-suspension through shear induced migration.[66,67] Similarly, for suspensions which exhibit yield stress behavior, the capillary ridge gets stabilized by the innate yield strength of the fluid allowing the film to spread to a larger extent before the instability ensues.[72,74] Linear stability analysis of the thin film equations for such yield stress fluids, incorporating a suitable stress constitutive equation, correctly predicts the observed behavior.[74] In certain cases, however, the instability can be simply due to local yielding of the suspension[96] and not the usual contact line instability along the advancing film front. An enhancement in the fingering instability, compared to the base suspending liquid, is predicted using linear stability analysis of thin film equations for hard sphere, non-Brownian, well-mixed suspensions.[75] The dynamic heterogeneity in the particle concentration observed in the spreading film is modeled using the thin film equations as for liquids, but with appropriate contributions through particle settling and shear induced diffusion and most importantly, spatially varying particle concentration dependent viscosity.

Despite the ubiquity and abundance of suspensions in several practical applications, the studies on particle-laden thin film flow are limited to inclined plane geometry. Systematic study of dependence of the instability and finger formation on the particle volume fraction during the spreading of neutrally buoyant non-Brownian suspensions on a spinning disc, which allows variations of the driving force amplitude over a much wider range than gravity, is absent. Therefore, specific flow features which are affected by the presence of particles are unknown. This information is essential to understand the role which particles play in the onset and evolution of instability as well as the overall spreading dynamics. Further, all of the previous studies have been carried out with the suspending liquid of high wettability whose spreading is shown to be inhibited by the presence of particles.

In this chapter, spreading of thin film of a suspension under centrifugal forcing is investigated in detail using flow visualization experiments. Suspension drops of neu-

trally buoyant non-Brownian hard sphere particles suspended in a partially wetting liquid are used for the study. The objective is to investigate the effect of variation of particle volume fraction (ϕ_p) and rotational speed on the overall spreading behavior and instability characteristics. The results are also compared with the spreading behavior of two Newtonian liquids of varying viscosity and wettability.

5.2 Experimental details [1]

5.2.1 Materials and apparatus

The experimental assembly shown in Fig. 5.1 is the same as used for the two-fluid experiments described in Chapter 4. It consists of a flat, aluminium disc of diameter 15 cm driven by a computer controlled DC stepper motor. The disc can be rotated in the range $50 - 10000$ revolutions per minute (rpm). The desired speed is achieved from rest using an acceleration of 1000 rpm/s. The feedback controller mechanism ensures that the random fluctuations in the rotational speed are within 2% for 250 rpm while they are within 5% for 1000 rpm.

Three different fluids, two Newtonian liquids and a suspension, were used in the experiments, the properties of which are given in Table 5.1. The suspension was prepared by immersing glass beads (of an approximate normal size distribution with mean diameter $d = 52$ μm and standard deviation 11 μm, and density 2.45 g/cc as procured from Potters, Inc.) in a liquid of matching density prepared from a mixture of LST liquid (density 2.85 g/cc) and glycerol (density 1.26 g/cc). The density matching between particles and liquid is attained to the accuracy of three decimal places. LST (Lithium heteropolytungstates) is a water soluble heavy mineral liquid, typically used for particle separations. Suspensions of varying ϕ_p $(0.1 - 0.55)$ were prepared by mixing different amounts of glass beads in the glycerol-LST mixture. The viscosities of all the fluids, including suspensions, were obtained using the steady

[1] The experimental set-up, the streamlining of the entire experimental procedure and the experimental data acquisition is credited to Mr. Mayuresh Kulkarni while the suspension rheology data acquisition is credited to Mr. Sameer Huprikar, who were my labmates during the PhD duration.

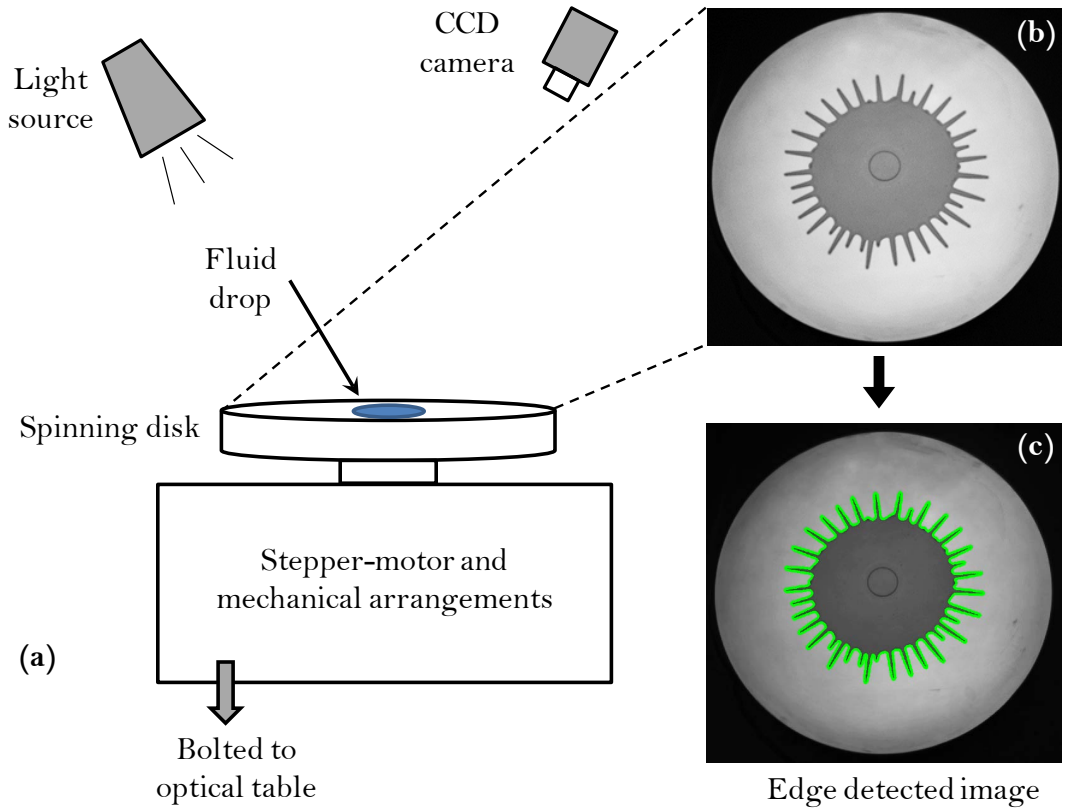

Figure 5.1: Schematic of the experimental set up. (a) Spinning disc assembly and image acquisition system (b) Sample image (for PDMS) taken at certain stage of spreading (c) Same image as in (b) but superimposed with the edge detected coordinates.

state rheology measurements carried out in a stress controlled rheometer. For all values of ϕ_p studied, the suspensions exhibit a Newtonian behavior for shear rates upto 10^3 s^{-1} (which are much more than those encountered in experiments). The stress-strain curves for the suspensions of varying particle volume fractions are shown in Fig. 5.2. Viscosity value for a particular fluid was calculated by fitting straight line (power-law correlation for n=1, i.e., Newtonian fluid) to the data points shown in Fig. 5.2 and obtaining the slope. The measured values of viscosity obey the well known Krieger-Dougherty model[97] for hard sphere suspensions:

$$\eta_r = \left[1 - \frac{\phi_p}{\phi_{max}}\right]^{-[\eta_{int}]\phi_{max}} \tag{5.1}$$

where, η_r, ϕ_p, ϕ_{max}, and $[\eta_{int}]$ are the relative viscosity (η/η_0, i.e., ratio of the viscosity

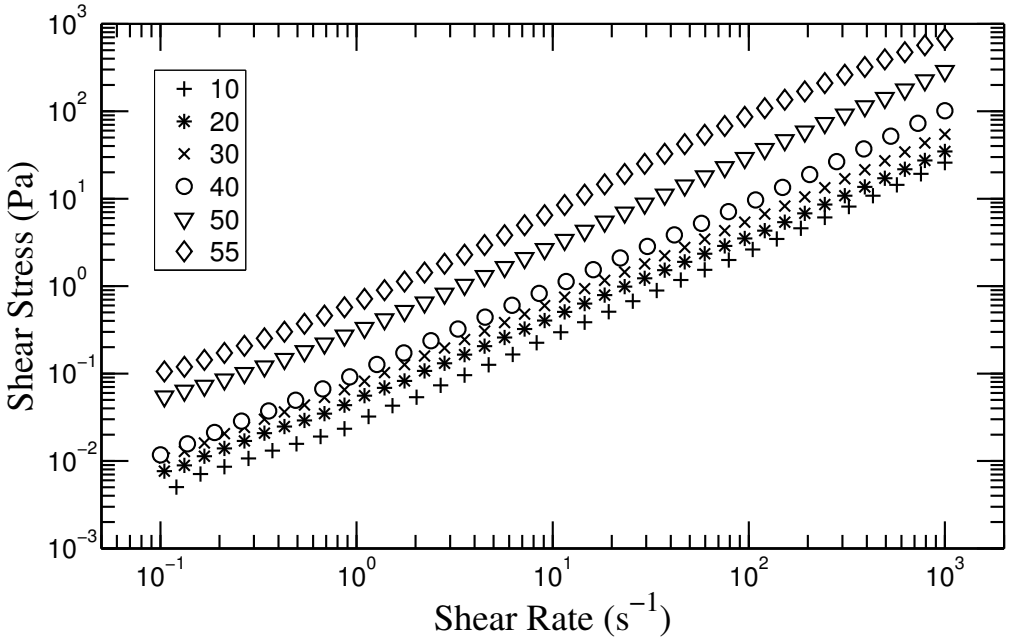

Figure 5.2: Stress-strain curves for the varying volume fraction of suspensions studied.

of the suspension to the base suspending medium) of the suspension, volume fraction of the particles, maximum packing fraction (taken as 0.64), and intrinsic viscosity (usually taken as 2.5 for hard sphere particles). A comparison of the experimentally measured viscosity of the suspension and the corresponding data fitting using Krieger-Dougherty model is shown in Fig. 5.3.

To measure the static contact angle, a drop of fluid was placed on the horizontal substrate. The drop was imaged by a camera placed sideways and in the plane of the substrate. The image was analyzed using ImageJ software to obtain the static contact angle. The values and corresponding errors reported in Table 5.1 represent average over 20 independent measurements. The surface tension values of the liquids used were measured using pendant-drop method. The surface tensions of PDMS, Glycerol and suspending liquid (LST+glycerol) are, respectively, 19.2 dyn cm^{-1}, 64.2 dyn cm^{-1} and 70 dyn cm^{-1}. Unlike that for pure liquids, the surface tension value for suspensions with $\phi_p \geq 0.2$ decreases continuously with time and never reaches a steady value. This continuously decrease is, perhaps, due to particle rearrangement causing the continuous deformation of the surface. This behavior gets accentuated

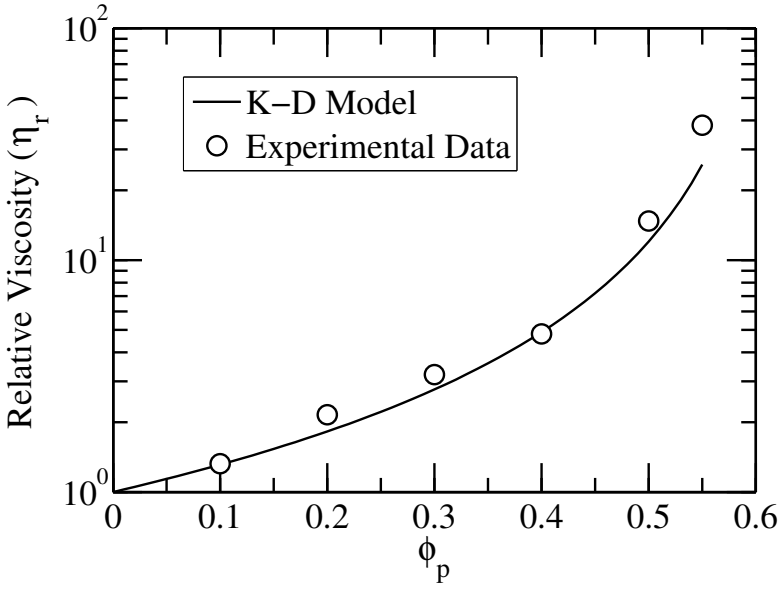

Figure 5.3: Experimentally measured relative viscosity as a function of the particle volume fraction. The solid line is the prediction of Krieger−Dougherty model.

for higher particle volume fraction, precluding us from reporting the surface tension values for suspensions. We simple report the static contact angle which has same values as that for the suspending liquid.

5.2.2 Experimental procedure

In every experiment, a small drop of Polydimethylsiloxane (PDMS) (0.8 ml) or glycerol (1.1 ml) or suspension (1.1 ml) of particular value of ϕ_p was placed at the center of the disc. While micro-liter syringes operated using a mechanical and micrometer assembly can be used to dispense exact volume of liquid precisely at the disk center, the same method cannot be used for suspensions. The suspension was found to cling significantly to the walls of the pipette tip resulting in the inaccuracy of 5% in the added volume and about 5% in the volume fraction of the drop on the disk surface. To overcome this issue as much as possible, a cylindrical hollow tube ($3 - 4$ cm long and 1 cm in diameter) was used, which was placed vertically at the center and flushed parallel to the aluminium disc surface. Suspension was poured in a hemispherical cavity of known volume. This cavity was emptied out very slowly in the hollow tube so

Table 5.1: Physical properties of the fluids used in the experiments.

Fluids	Density (g cm^{-3})	Viscosity (Pa s)	Volume (cm^3)	Static contact angle (deg)
Glycerol	1.26	0.896	1.1	68 ± 3
PDMS	0.91	0.173	0.8	7 ± 3
LST+Glycerol ($\phi_p = 0.0$)	2.45	0.022	1.1	65 ± 3
Suspension ($\phi_p = 0.100$)	2.45	0.027	1.1	65 ± 3
Suspension ($\phi_p = 0.200$)	2.45	0.043	1.1	65 ± 3
Suspension ($\phi_p = 0.300$)	2.45	0.064	1.1	65 ± 3
Suspension ($\phi_p = 0.400$)	2.45	0.096	1.1	65 ± 3
Suspension ($\phi_p = 0.425$)	2.45	0.132	1.1	65 ± 3
Suspension ($\phi_p = 0.450$)	2.45	0.162	1.1	65 ± 3
Suspension ($\phi_p = 0.475$)	2.45	0.220	1.1	65 ± 3
Suspension ($\phi_p = 0.500$)	2.45	0.295	1.1	65 ± 3
Suspension ($\phi_p = 0.525$)	2.45	0.350	1.1	65 ± 3
Suspension ($\phi_p = 0.550$)	2.45	0.763	1.1	65 ± 3

that suspension remained on the disk surface as a drop with minimum contact with the enclosing tube surface. The tube, using micrometer screw arrangement, was then lifted very slowly which eventually leaves behind a nearly circular drop of suspension. The slow lifting of the tube minimizes the splashing when the tube loses contact with the liquid. Even using this method, some amount of suspension always clings to the wall of the cavity and some to the walls of the vertical tube, but the surface area over which the material clings is very small leading to an accuracy of 1% in the volume added as well as 1% in the volume fraction of the suspension drop added to the disc.

The disc surface, before every experiment, was washed multiple times using soap solution and rinsed with DI water followed by acetone to remove any traces of fluid used from the previous experiments. It was then mounted exactly horizontally on the spinning assembly. This protocol ensured the reproducibility of the experimental results. Experiments were carried out for four different rotational speeds of the disc: 250, 500, 750, and 1000 rpm. Each experiment was repeated 5 times and the results presented are averages over these experiments.

5.2.3 Imaging and analysis

The surface of the disc is illuminated from above using a bright halogen lamp. A diffuser plate placed in front of the light generates an uniform light distribution across the plate surface. The motion of fluid on the surface of the aluminium disc is captured from above using a high-speed camera with an exposure of 150 μs to acquire sharp images. A small amount of fluorescent dye (Rhodamine B) was added to the transparent fluid for ease in the flow visualization and image analysis using better contrast (see inset of Fig. 5.1(b) showing a fluid, appearing in dark color, which has spread to a certain extent). The addition of the fluorescent dye changes the surface tensions of PDMS, glycerol, and LST-glycerol mixture by 0.05%, 0.3%, and 3.3%, respectively, which is small enough to induce any qualitative changes in the observed behavior. The camera, as shown in Fig. 5.1(a), is placed slightly inclined to the vertical. This is to prevent the reflection of the camera from the optically flat substrate surface appearing in the images which can create difficulty in image analysis. The oblique positioning of the camera with respect to the plate surface makes the drop and plate appear non-circular in the images due to unequal distance of different regions on the plate from the camera. This spatial variation was taken into account by imaging four concentric circles drawn on a similar plate, under similar camera, plate and light positioning, spanning the whole area and obtaining the coordinates along the circumference of each circle (See Fig. 5.4). The alternate positioning of the white and black bands as shown in the figure makes the detection of the circles much easier. This procedure provided the ratio between the actual radius and the apparent radius obtained from the images at different spatial locations which was then applied to the fluid spreading images appropriately. Increasing more measurements (i.e. drawing several more concentric circles) improved the correction by a negligible amount.

The image analysis procedure and quantities determined are nearly the same for two-fluid experiments from Chapter 4. We reproduce the details again for ease of reading. The acquired images were analysed in ImageJ and MATLAB® to track the position of the interface and extract its behavior. The sequence of steps involved in

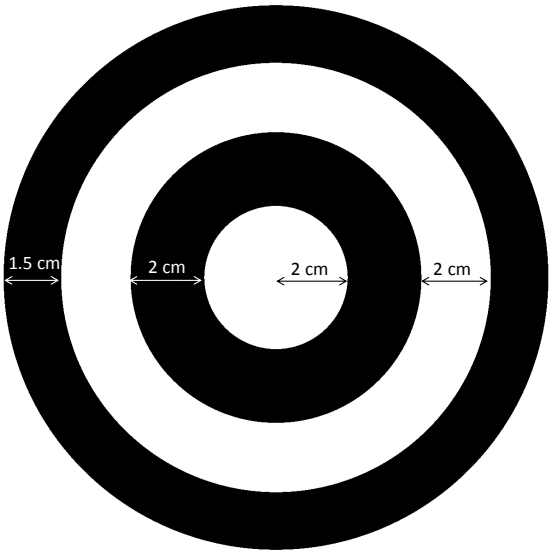

Figure 5.4: Scale used for image calibration.

the edge detection process is shown in Fig. 5.6. First, the raw image is converted to a binary image. In the next step, the image is inverted and the connected component (drop) having only white pixels (the required object) is identified. Any noise in the required object image is then removed and finally, the edge is extracted using standard edge detection algorithm ('sobel' method) available in MATLAB's inbuilt image analysis tool. The edge detected coordinates were calibrated using the scale shown in Fig. 5.4. The algorithms use the polar and Cartesian coordinate systems with the origin at the center of the disc. The edges were detected to an accuracy of ± 0.15 mm (see Fig. 5.1(c)). The edge detection data was used to calculate several quantities, viz., effective radius (R) at different radial locations (i.e., different times), spreading rates, instability wavelengths, and number of fingers. The effective radius at different times before the onset of instability, was obtained by fitting a circle to the edge detected coordinates. In order to find the finger front position as a function of time, the image data was first converted to polar coordinates (r-θ) and the local maxima (finger tips) in each image data was found out as shown in Fig. 5.5. Then, one particular finger tip position was tracked in subsequent images to find out the position of the finger front with time. Depending on the rotational frequency and the camera frame rate, the tip position of a particular finger in the next image was

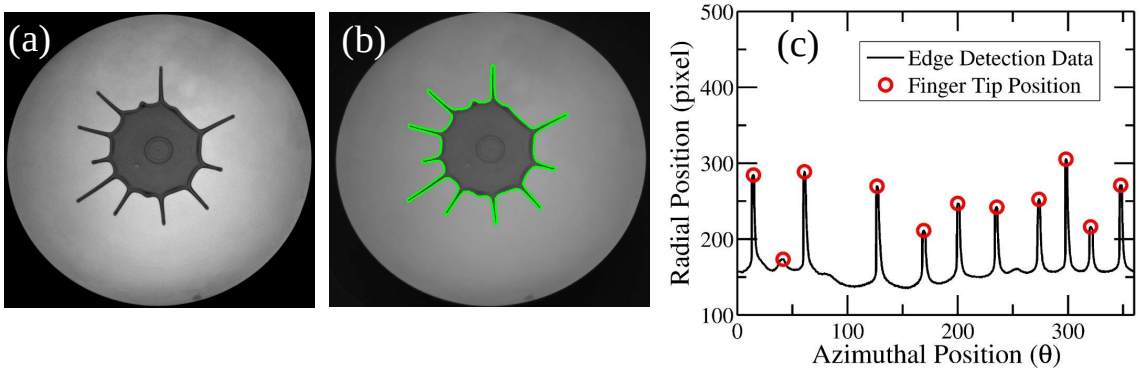

Figure 5.5: Steps involved in tracking the finger front position. (a) Original experimental image, (b) corresponding edge detected coordinates superimposed on the original image, and (c) finger tip positions in (b) plotted in polar coordinates $(r - \theta)$.

obtained by searching within a specified range of angular distance. After finding out the front position with time for several fingers in a particular experiment, it was observed that the trends were not much different for all the fingers as compared to the fastest growing finger. Therefore, the data is reported only for the fastest growing finger in all the experiments.

5.3 Results and discussion

5.3.1 Spreading behavior

Figure 5.8 shows the spreading of partially wetting glycerol, completely wetting PDMS and suspensions ($\phi_p = 0.45, 0.475, 0.525, 0.55$) at a rotational speed of 500 rpm. Each column corresponds to the spreading of a particular fluid at different times. Each row corresponds to the same degree of deformation of the drop boundary for all the fluids. The degree of deformation is defined as $[(R_1 - R_2)/R_2] \times 100$, where R_1 is the largest radius for the drop (distance of the farthest point from the axis of rotation) and R_2 is the radius of a circle centered on the axis of rotation and having same area as that covered by the drop (See Fig. 5.7). The rows 2, 3,and 4 thus, correspond to a deformation of 10% and 20%, and 30% respectively, for all fluids.

The drop of PDMS, when placed on the disc, occupies a larger area compared

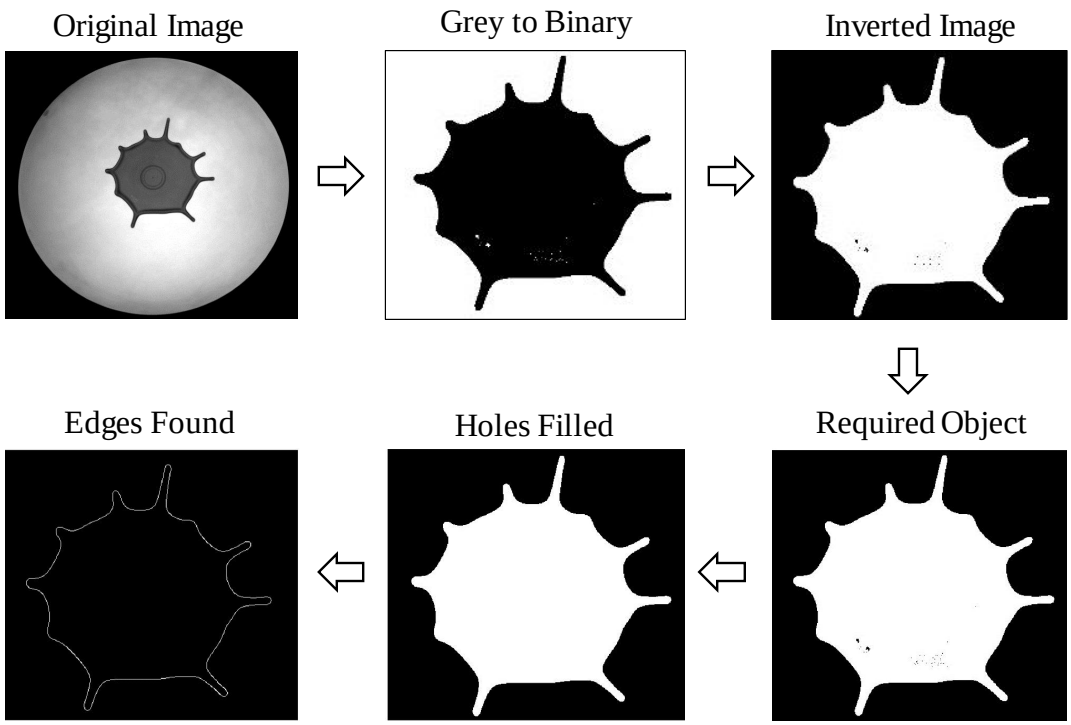

Figure 5.6: Sequence of operations involved in the processing of raw image to extract the edge of a spreading drop.

to the drop of glycerol and suspensions even if the volume used is smaller (row 1 in Fig. 5.8). This is due to high wettability of PDMS (small contact angle) with respect to the disc surface, which spreads to occupy a larger area. The suspension drop (for all ϕ_p) occupies nearly the same area of the disc as the glycerol drop. This suggests that the suspending liquid, which has the same wettability as glycerol (nearly same contact angles as shown in Table 5.1) primarily determines the final static configuration and the particles have relatively lesser influence. The finer details of the approach to this final static state,[98,99] and the possible particle influence therein, are not within the scope of this work and hence was not studied.

Once the rotation of the disc is started (500 rpm as shown in Fig. 5.8), the drops of glycerol (first column) and PDMS (sixth column) start to spread leading towards the formation of instability along the circumference (second row) and its further growth into fingers at later times (3rd row). The radius of the base circular region of the drop at which instability first appears, does not seem to increase significantly with

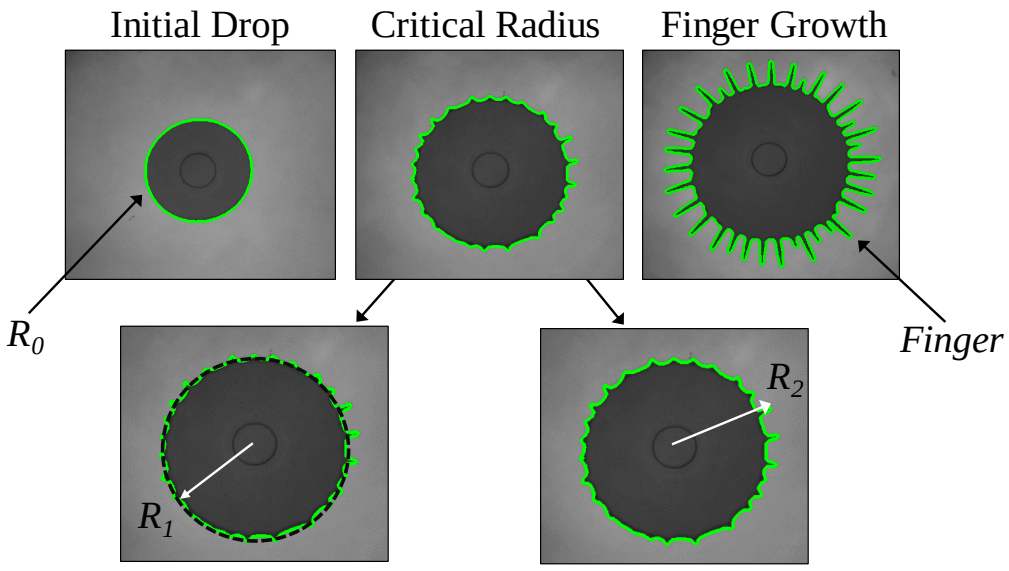

Figure 5.7: Images showing the definition of quantitative parameters obtained using image analysis.

the fluid continuously flowing outward through the fingers which eventually reach the periphery. This overall behavior, inclusive of the instability wavelength (or number of fingers formed), is very much in agreement with the analytical expression (See eq. 4.1) provided by Fraysse and Homsy[46].

The suspension, for all values of ϕ_p, spreads to a larger area before the instability is initiated compared to the spreading of a partially wetting liquid when the disc is rotated. Note that the suspending liquid is partially wetting, like glycerol. The extent of spreading, before the initiation of instability, increases gradually up to $\phi_p = 0.525$ and then decreases slightly at the highest particle volume fraction ($\phi_p = 0.55$). This indicates stabilization of the contact line due to the increasing presence of particles which is qualitatively similar to that observed during the spreading of a viscoelastic fluid[47] and clay suspensions which exhibit a finite yield stress.[72,74] For the values of ϕ_p studied over here, the suspensions, however, do not exhibit a yield stress or show a viscoelastic behavior as ascertained from the bulk rheology measurements. Further, when compared to pure liquids, the base circular region of suspension (for any particular ϕ_p) continues to spread significantly post the instability initiation. Increasing the rotational speed beyond 500 rpm does not qualitatively change the

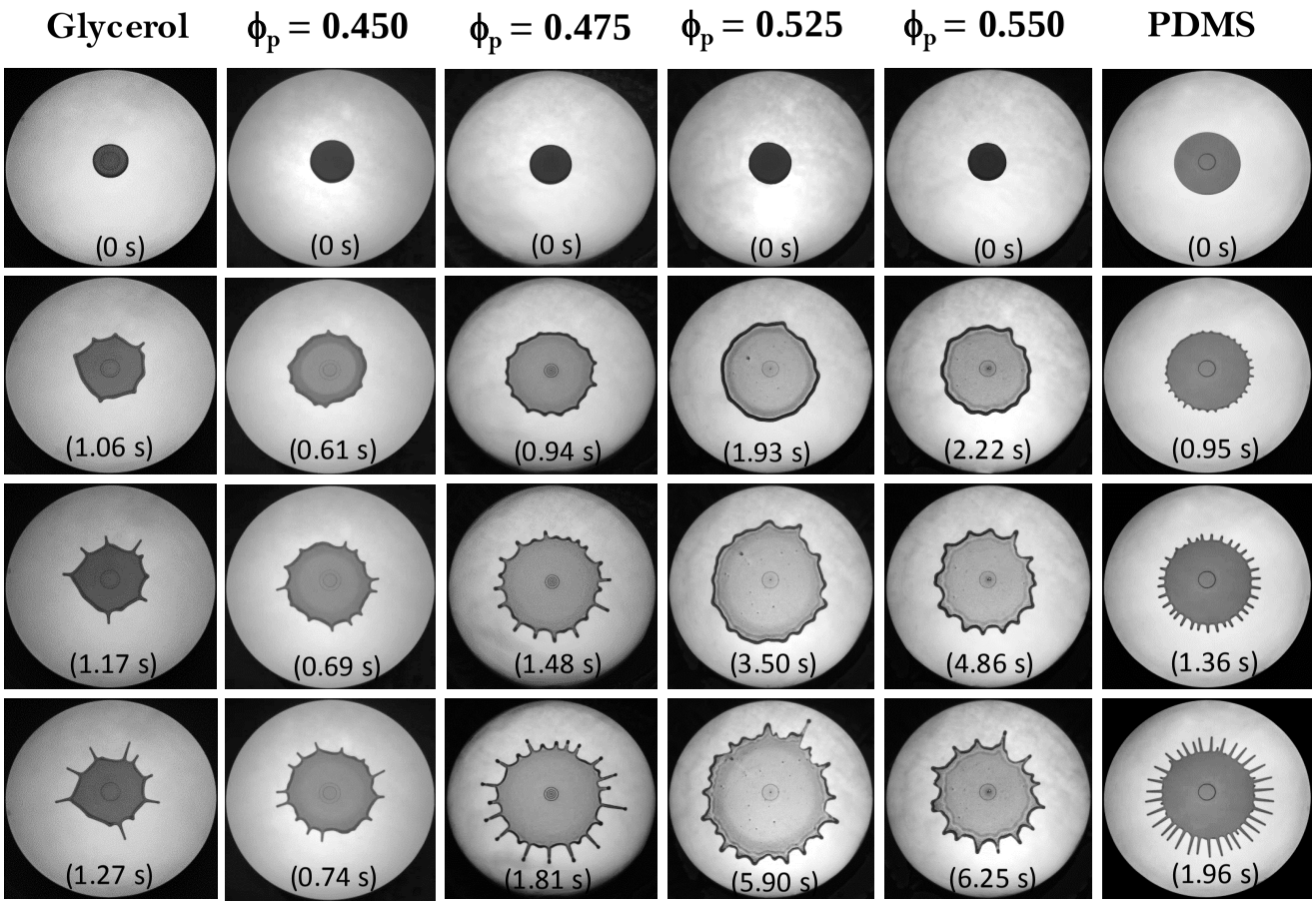

Figure 5.8: Static images for a few fluids obtained at different times (or different radial positions) for a rotational speed of 500 rpm. Each column corresponds to a particular fluid while each row corresponds to the state of the fluid at a particular time (embedded in each image). The suspension images are flanked in the middle by images for partially wetting glycerol as first column and that for the completely wetting PDMS as the last column. Initial volume is 1.1 ml for all fluids except PDMS for which 0.8 ml was used.

spreading behavior, however, lowering the rotational speed reduces the spreading tendency significantly. The qualitative behavior of the fingering instability, however, remains the same for different rotational speeds as shown next.

Figure 5.9 illustrates the relative influence of the driving force (rotational speed employed) and particle volume fraction on the spreadability of the suspensions for 5 different volume fractions. All images are shown at the same percentage (10%) of deformation of the contact line (corresponding to onset of instability). Clearly, there is a big increase in the spreading tendency when rotational speed is increased from 250 to 500 rpm, for all ϕ_p. However, any further increase in the rotational speed does not qualitatively change the spreading behavior, suggesting a critical rotational speed demarcating different spreading behaviors. For rotational speeds 500 rpm and above, the behavior is nearly independent of ϕ_p (each row of Fig. 5.9). It is also observed that the time to attain the onset of instability decreases with increase in rotational speed decreasing spreading of a particular volume faction of suspension (each column of Fig. 5.9). A distinct behavior is observed for the highest ϕ_p studied for the case of 750 and 1000 rpm, where the extent of spreading seems to decrease as compared to 500 rpm. The reason for this could be the higher driving force which does not allow the drops to spread more once the instability is formed as compared to the case of 500 rpm. In fact, with further increase in time of spreading, the capillary ridge for the drops of $\phi_p = 0.55$, at 750 and 1000 rpm breaks and the material gets thrown off the disc.

The time evolution of the drops of suspension from their initial state up to the critical radius is shown in Fig. 5.10(a) for the rotational speed of 500 rpm along with the evolution of the drop of PDMS and glycerol. The results for the spreading/growth post-instability are shown later. The extent of spreading $(R(t) - R_0)$ is normalized by the cube root of initial volume (V_0) which is not the same for all fluids as mentioned earlier. Here, $R(t)$ is the radius of the spreading drop and R_0 is the radius of the drop in its initial state. The final point in each profile corresponds to critical radius (i.e., images in the second row shown in Fig. 5.8). The rate of spreading of the suspension drop decreases with increase in the particle volume fraction which can be expected [65]

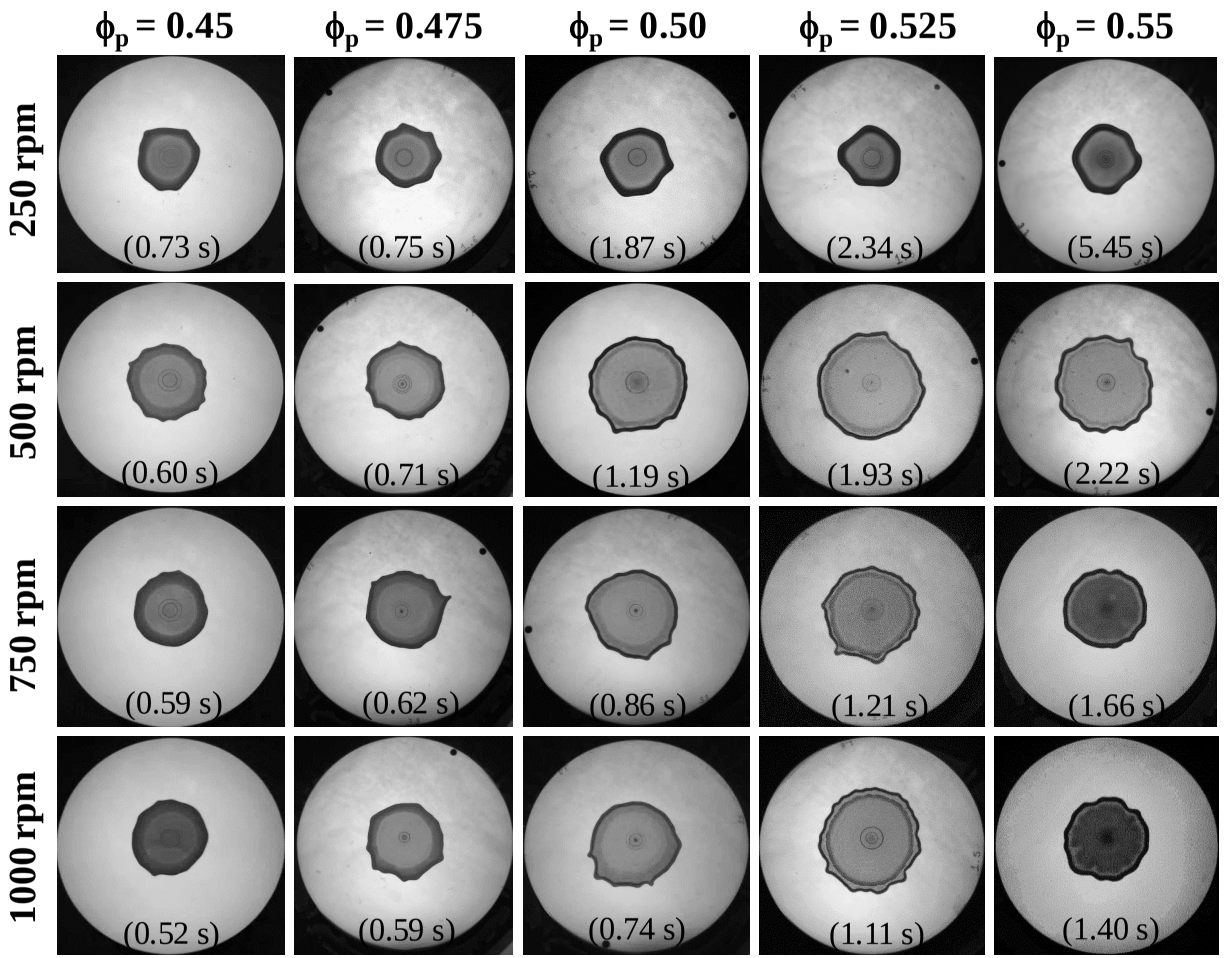

Figure 5.9: Static images showing relative importance of particle faction and rotational speed on the suspension spreadability. Every image represents the state of spreading corresponding to the contact line deformation of 10%. The time to achieve this state is embedded in each image block (cell).

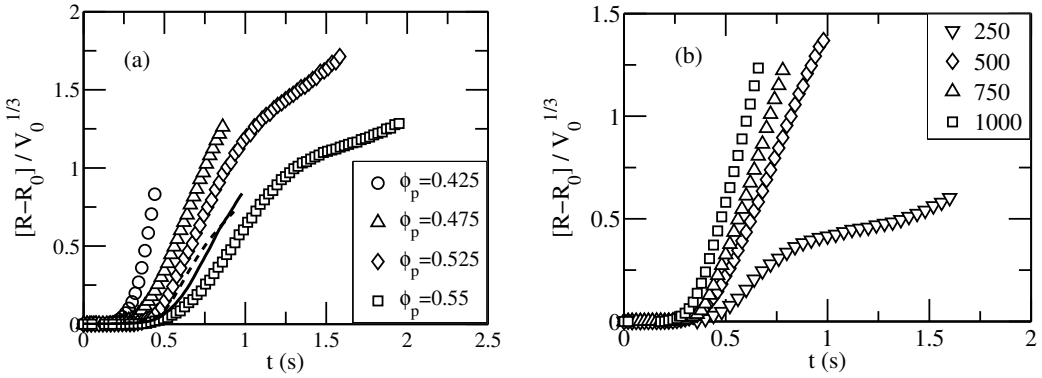

Figure 5.10: Spreading of a drop from its initial position upto the onset of instability for (a) varying particle ϕ_p at 500 rpm, and (b) 4 different rotational speeds for $\phi_p = 0.5$. The profiles in (a) represent the drop evolution from its initial position (row 1 in Fig. 5.8) upto the critical radius (row 2 in Fig. 5.8). Solid line in (a) denotes the spreading of glycerol while the dashed line denotes the spreading of PDMS.

given the increase in the viscosity (see Table 5.1). For the highest particle volume fraction ($\phi_p = 0.55$) studied, the spreading rate is even lower than that observed for the two liquids. The extent of spreading $(R(t) - R_0)$ for the suspension drop, however, increases continuously with ϕ_p before decreasing slightly at $\phi_p = 0.55$. Further, the time to attain the critical radius increases monotonically with increase in ϕ_p. The overall behavior seems to arise due to combined effect of viscosity as well as the ability of a fluid to spread. For instance, the viscosities of PDMS and suspension ($\phi_p = 0.45$) are nearly the same and both possess very different static contact angles, but the extent of spreading for same degree of deformation seems to be similar. Similarly, the viscosities of glycerol and suspension ($\phi_p = 0.55$) are nearly the same and both are partially wetting (large static contact angles), but still the suspension spreads to a larger extent. Finally, the spreading rates and extent of spreading for PDMS and glycerol, which have quite different viscosities and wettabilities, are nearly the same.

Fig. 5.10(b) shows the effect of driving force on the time evolution of the suspension drop from its initial state up to the critical radius for a particular volume fraction ($\phi_p = 0.5$). A sudden increase in the spreading rate is observed for increasing rotational speed from 250 to 500 rpm beyond which the increase is quite slower. Clearly, there is a critical rotational speed demarcating the spreading rate, the exact reasons for the origin of which are not clear at the moment.

5.3.2 Instability and finger growth

The characteristics of the contact line instability accompanying the spreading of the film are discussed. The reason for the occurrence of this instability in case of pure liquids has been discussed in detail in Chapter 4.[46,58,59,62,100] The parameters used for quantifying the instability are the critical radius (R_c), wavelength of instability (λ), number of fingers (N_f), and the growth rate of the fingers. The procedure for the measurement of the above parameters are the same as discussed in Chapter 4. The R_c value is normalized using the cube root of the initial drop volume (V_0) which is not the same for all fluids.

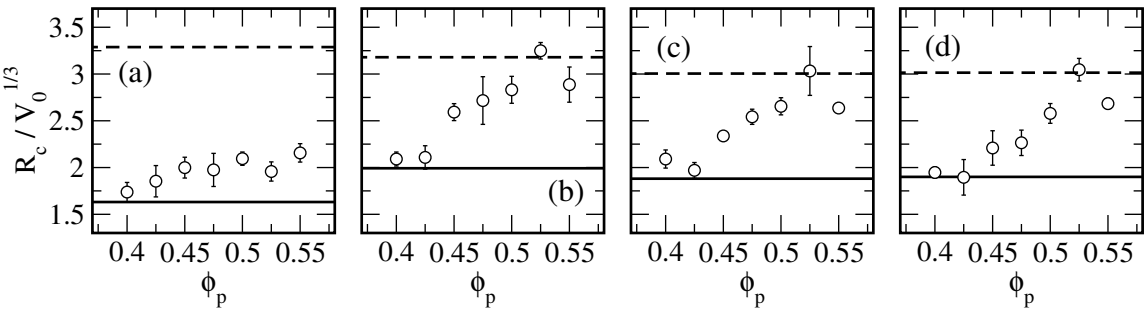

Figure 5.11: Normalized critical radius (R_c) at (a) 250 rpm, (b) 500 rpm, (c) 750 rpm and (d) 1000 rpm. Open circles denote the data for suspension. Error bars denote deviations obtained by averaging over five independent data sets. Values of R_c for glycerol and PDMS are shown, respectively, as solid and dashed lines.

Figure 5.11 shows the variation of the normalized critical radius with ϕ_p for all the rotational speeds studied. The critical radius for PDMS decreases slightly over the range of rotational speeds employed, which is in accordance with previously observed behavior.[46] For all other fluids, the critical radius increases with increase in rotational speed from 250 rpm to 500 rpm, beyond which it remains nearly constant (also observed in Fig. 5.9). Further, the critical radius for glycerol (shown as a solid line) is much lower than PDMS (shown as a dashed line) for all the rotational speeds which is expected given that PDMS is far more wetting than glycerol and hence can spread to a larger area before developing instabilities (compare first and sixth column in Fig. 5.8). The value of R_c at $\phi_p = 0.4$ and lower (not shown) is quite close to that for the partially wetting glycerol for all the rotational speeds which suggests that the

presence of particles has a negligible influence on the instability behavior for these values of ϕ_p. For these cases, the instability is, then, initiated due to the usual contact line instability of the partially wetting suspending liquid. Beyond $\phi_p = 0.4$, the value of R_c increases steadily (except at $\phi_p = 0.425$ for some rotational speeds which is not clear) towards that for PDMS, with a slight decrease at the highest ϕ_p for rotational speeds of 500 rpm and above. The rate of increase is smaller for 250 rpm compared to that for higher rotational speeds (evident from Fig 5.9).

The wavelength (λ) of the instability is related to the experimentally determined critical radius (R_c) and number of ensuing fingers (N_f) as counted from the images, by the geometric relation [46] $\lambda = (2\pi R_c)/N_f$. All the measurements are carried out at a radial location where the degree of deformation is 10%. The secondary fingers which form at later times (larger degree of deformation or spreading) between the existing fingers are not included over here. Fig. 5.12 depicts the wavelength of instability obtained using the above procedure for different fluids for all the four rotational speeds employed. PDMS has lower surface tension and breaks into several fingers associated with smaller instability wavelength. Glycerol, on the other hand, has higher surface tension and breaks into lesser fingers associated with larger instability wavelength to minimize the surface energy. This behavior is very well known in the literature and the values of the wavelength for both the liquids are in accordance with the predictions obtained through the linear stability analysis of thin film equations as discussed in Chapter 2.

The data for suspension exhibits a very interesting non-monotonic dependence on increasing ϕ_p for all the rotational speeds. There is no existing model available for thin film flow of a suspension on a spinning disc which can explain this non-monotonic behavior. Also, there are no theoretical equations available which are valid for pure liquids and can be easily translated to suspensions to account for this peculiar behavior. The decreasing and increasing behavior can, however, be independently understood based on the theoretical works done previously, as discussed next.

The decrease in the wavelength observed in Fig. 5.12, is in qualitative agreement with the linear stability analysis of thin film equations by Cook *et al.* [75] These authors

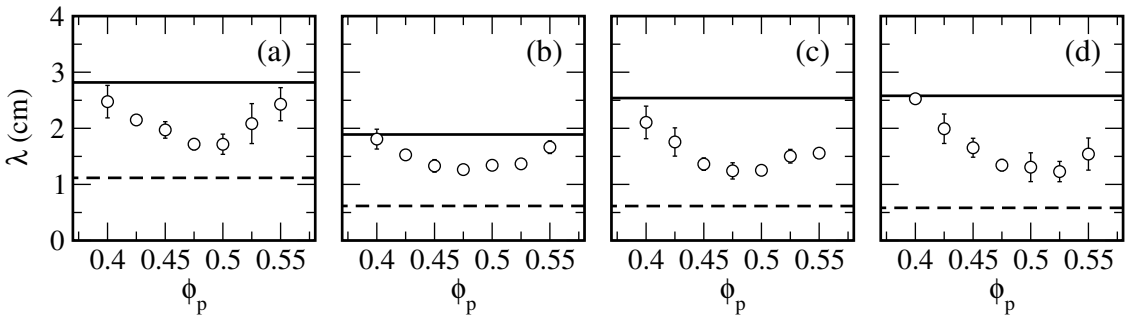

Figure 5.12: Wavelength of the instability (λ) for (a) 250 rpm, (b) 500 rpm, (c) 750 rpm and (d) 1000 rpm. Open circles denote the data for suspension. Error bars denote deviations obtained by averaging over five independent data sets. Values of λ for glycerol and PDMS are shown, respectively, as solid and dashed lines.

have numerically studied the fingering instability in case of particle-laden thin film flowing down an inclined plane (not on a spinning disc), and for a suspension in a wetting liquid medium. They have developed a continuum two-phase (separate momentum equations for the mixture phase and the particle phase) model for a non-buoyant suspension, including the effect of shear induced diffusion[101] (i.e., diffusion in the horizontal direction resulting from the horizontal concentration gradient of ϕ_p). The depth averaged velocity term in the thin film equation[59] (for pure liquid) provided in Chapter 2 (eq. 2.2) is replaced with volume averaged velocity term which involves the velocity contributions from both particle as well as liquid phase. A linear stability analysis is performed on this model by perturbing the time-dependent base state in both space and time. Note that the base state in case of thin film flow of a pure liquid is quasi-static and hence easy to model as compared to the time-dependent base state for the case of suspension. The numerical stability analysis is able to capture the decrease in the instability wavelength for a suspension film compared to that for the film of the suspending liquid.[22] In our experiments, this raises the possibility of the presence of particle concentration gradients within the capillary ridge which can cause diffusion of particles and consequently lower wavelengths. The primary reason behind the formation of such a concentration gradient in the system, if at all present, is however not clear and needs to be investigated further. However, this model cannot explain the increase in the wavelength observed beyond a certain ϕ_p.

The higher wavelengths observed in Fig. 5.12 at higher values of ϕ_p seem to be in qualitative agreement with the predictions of linear stability analysis of thin film equations for yield stress (viscoplastic) suspension by Balmforth *et al.*[74] Again, their model is for inclined plane flow of a suspension and wetting suspending liquid. The model, incorporates a suitable Bingham stress constitutive equation to obtain the thin film equation and solve for the corresponding base state profile. A stability analysis performed on the above system captures an increase in the wavelength for a suspension film compared to the film of the suspending liquid, through the increasing yield stress, which is also observed in their experiments. For the higher concentrations studied in our experiments, this raises the possibility of particle crowding within the capillary ridge, which will ensue a contact network and impart a yield stress, leading to the observed higher wavelengths. Again, the exact mechanism behind the crowding of the particles in the ridge, if at all present, needs further investigation.

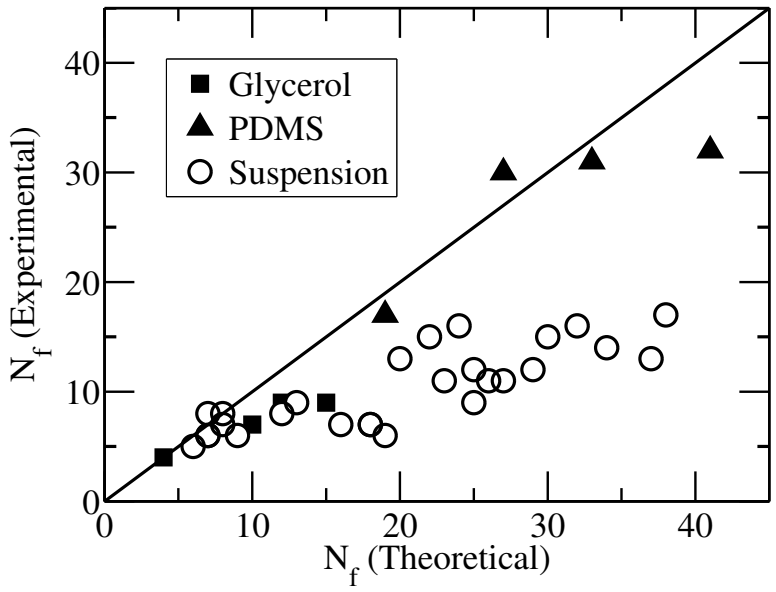

Figure 5.13: Comparison of the experimentally determined values for N_f with that predicted by linear stability theory. Symbols denote data for PDMS, glycerol and suspensions (all ϕ_p) obtained at all four rotational speeds studied. Solid line shows $y = x$

The linear stability analysis for viscous, wetting, Newtonian liquid[46] which provides the expression for predicting the value of N_f using the properties of the fluid and the measured value of R_c is provided in eq. 4.1 in Chapter 4. This equation

predicts the value of N_f quite well for PDMS and glycerol as shown in Fig. 5.13. The theory, however, over-predicts the N_f for the suspension data including all ϕ_p and rotational speeds. The reason for such an over-prediction is not quite clear at the moment. Nevertheless, it is interesting that the data for varying ϕ_p and wide range of rotational speed clutter around a straight line with a different slope in spite of a very varied spreading behavior exhibited by suspensions as described in this work which definitely is not controlled by the value of γ for a static drop. Curiously enough, Eq. (4.1), is able to predict the value of N_f for viscoelastic fluids quite well[47].

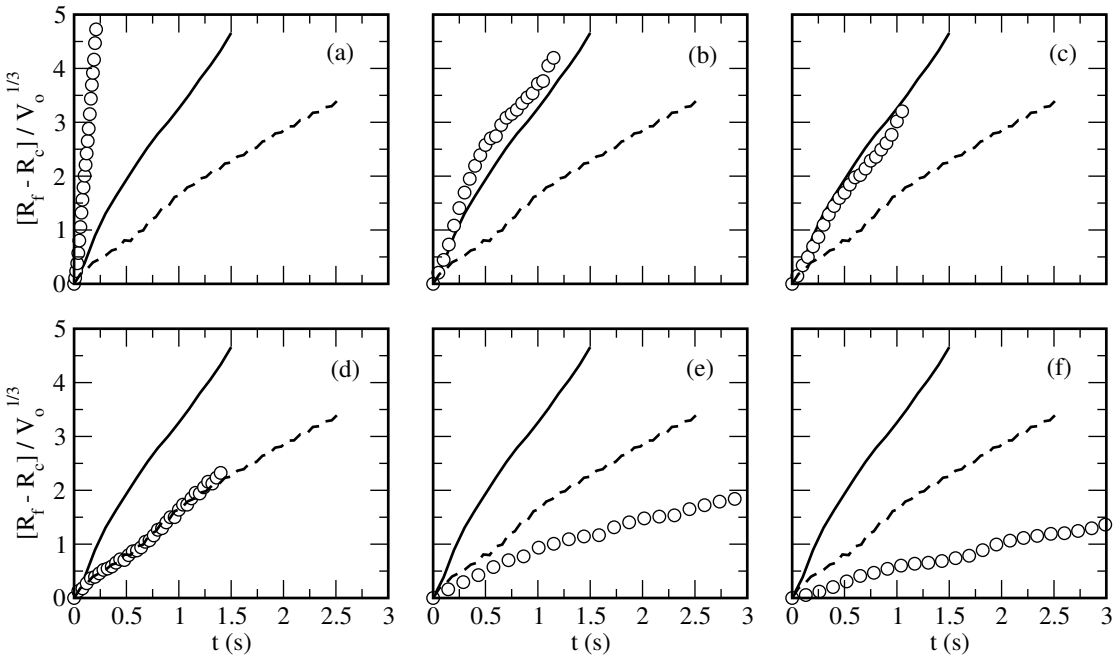

Figure 5.14: Normalized growth of the fastest moving finger for 500 rpm. Open circles denote data of suspension (a) $\phi_p = 0.4$, (b) $\phi_p = 0.45$, (c) $\phi_p = 0.475$, (d) $\phi_p = 0.5$, (e) $\phi_p = 0.525$ and (f) $\phi_p = 0.55$. Solid line denote finger growth for glycerol while dashed line denotes finger growth for PDMS.

Finally, the growth of the fingers post-instability formation is discussed. Here, only the fastest growing finger is considered, though the behavior is more or less the same for other fingers. Figure 5.14 shows the growth of the fastest growing finger $(R_f - R_c)$ normalized by the cube root of the initial volume (V_0) at 500 rpm. Here, R_f is the distance of the finger front from the axis of rotation and R_c is the critical radius. Glycerol forms less number of fingers and all the fluid passes outwards from the

existing fingers leading to a faster growth rate (solid line in Fig. 5.14). In contrast, PDMS forms more fingers and the liquid flows outward through fingers as well as during the slow spreading of the central drop causing an overall lower rate in the finger growth (dashed line in Fig. 5.14). With increasing particle volume fraction, the suspension data show a monotonic decrease in the rate at which the fingers grow in time. The rate, is faster at lower values of ϕ_p, decreases and is nearly identical to that for glycerol at $\phi_p = 0.475$, decreases further to be similar to that for PDMS at $\phi_p = 0.5$ and falls further for highest values of ϕ_p studied. This overall behavior is a combination of varying viscosity and the particle influence on finger growth with increasing ϕ_p. The observed trend for 500 rpm for the evolution of finger front position remains valid for all the rotational speeds studied.

5.4 Conclusions

In summary, a unique and curious effect of the particle volume fraction on the spreading behavior of a film of suspension is shown, through flow visualization experiments. The critical radius for the onset of instability is found to increase gradually with increase in the particle volume fraction with a slight drop off at the highest particle volume fraction studied, while the instability wavelength decreases and then increases again while going through a minimum for the same range of particle volume fractions. The decrease and increase in the wavelength are, respectively, attributed to the possible particle concentration variations in the capillary ridge at lower ϕ_p and particle crowding at higher ϕ_p. The supporting arguments provided on the basis of previous theoretical studies[74,75] are qualitative, but the results presented are, nevertheless, quite significant. They should provide strong impetus towards developing a theoretical framework capable of encompassing the existence of seemingly different spreading characteristics of a suspension film within a small concentration range.

Some interesting avenues within the scope of future work are (i) actual visualization of particle motion within the capillary ridge, (ii) changes in the contact line instability for a mixture of particles differing in size, for non-neutrally buoyant parti-

cles and for non-Newtonian suspending liquids, and (iii) altering the particle surface properties to change its affinity with respect to liquid. The results also suggest possible mechanism of altering the spreading behavior of a thin film of liquid by addition of non-interacting particles which should be of interest to industrial applications.

Chapter 6

Conclusions and Future Directions

6.1 Conclusions

We have carried out a systematic study to investigate the spreading and instability behavior of a thin film of liquid on a spinning disc, the contact line behavior of which is altered using an externally located immiscible liquid and internally suspended solid particles. Both theoretical and experimental studies are carried out for the flow, of a Newtonian liquid spreading in presence of another liquid on its top and of suspensions, on a spinning disc. A summary of the results and conclusions of the work are provided below.

A systematic study of the axisymmetric two-layer spin coating process is carried out using numerical simulations. The fluids used are assumed to be Newtonian and fully wetting. A precursor layer model is used to relieve the singularity of the contact line. The effects of the ratios of the physical properties of the liquids, and process parameters on the uniformity of the two-layer film and spreading behavior are investigated. Our results demonstrate that bulkiness of the capillary ridge increases with an increase in the viscosity ratio. Also, the capillary ridge becomes sharper with the decrease in the interfacial tension ratio. The formation of the sharp capillary ridges could affect the uniformity of the two-layer film. Nevertheless, our results suggested that a uniform two-layer thin film can form when the fluid in the upper layer is less viscous or when the upper gas-liquid surface tension is more than the

inner liquid-liquid interfacial tension. Furthermore, it is observed that increase in the precursor layer thickness facilitated the film to become uniform. An important finding is that the increase in the volume ratio did not affect the uniformity of the film. Therefore, the simulation results implicate that operating the process with an equal volume of the fluids in both the layers will produce a uniform two-layer coating film with minimal loss of the liquids.

Majority of the previous studies in this field have looked at the film thinning behavior and interfacial instability for stratified two-layer flow of thin liquid films. Our results, are the first ever results which demonstrate the effect of ratio of fluid properties and process parameters on the shape of the capillary ridge close to the two contact lines, and their corresponding evolution. The results of our study are useful in determining the optimum parameter space for a given two-layer coating application. Nevertheless, this study has certain practical limitations. Due to the axisymmetric nature of the simulation, it cannot explain the instability that occurs in these type of flows. Furthermore, the simulation results are applicable only to fully wetting liquids. In other words, it cannot predict the behavior for partially wetting liquids. The major practical issue is associated with the Newtonian fluid assumption, which limits the applicability of the model for predicting flow behavior in case of non-Newtonian liquids such as polymeric liquids and suspensions which are widely used in industrial applications.

Fingering instability in case of simultaneous centrifugal spreading of a drop of Newtonian liquid spread on a top of another drop of Newtonian liquid is studied experimentally and the results are presented for varying volume ratios of the two liquids. Both qualitative as well as quantitative differences in instability behavior for the single and two-liquids has been observed for the experimental conditions considered in our study. It is found that the number of fingers which form in case of the two-liquid spreading process is comparatively higher than the single liquid case. Also, the spreading dynamics and onset of instability are significantly altered by the presence of a liquid-liquid interface. After comparison of the experimental results of the liquid spreading in presence of another liquid with the available linear stability theory for

predicting the N_f for single liquid spreading, it is found that the the inner liquid data for two-fluid case does not agree with the theory. In fact, the theory overpredicts the number of fingers observed in experiments. A new theory has been derived by using linear stability analysis for small but finite surface to interfacial tension ratio, and it has been found that the presence of outer interface brings down the value of most unstable wave number as compared to single fluid case. This is equivalent to the observed decrease in the number of finger in our experiments. Furthermore, a newer effect of finger break up and drop formation is also observed experimentally and is not reported elsewhere.

Finally, a unique and interesting effect of the particle fraction on the spreading behavior of a film of suspension is shown, through flow visualization experiments. The critical radius for the onset of instability is found to increase gradually with increase in the particle fraction with a slight decrease at the highest particle fraction studied, while the instability wavelength decreases and then increases again while going through a minimum for the same range of particle fractions. The decrease and increase in the wavelength are, respectively, attributed to the possible particle concentration variations in the capillary ridge at lower ϕ_p and particle crowding at higher ϕ_p. The supporting arguments provided on the basis of previous theoretical studies [74,75] are qualitative, but the results presented are, nevertheless, quite significant. They should provide strong impetus towards developing a theoretical framework capable of encompassing the existence of seemingly different spreading characteristics of a suspension film within a small concentration range. The results also suggest possible mechanism of altering the spreading behavior of a thin film of liquid by addition of non-interacting particles which should be of interest to industrial applications.

6.2 Future Directions

The results of our research poses some open questions which can be addressed through future work. The future studies may include:

- Extending the two-layer axisymmetric code to include the partially wetting

behavior of liquids to understand the capillary ridge formation and its stability subjected to azimuthal perturbations.

- Modification of the mathematical model to study the two-layer spin coating process of non-Newtonian fluids such as polymer melts, emulsions and suspensions.

- Analysis of the size distribution of the droplets obtained in two-liquid experiments for varying experimental parameters.

- Experimental visualization of particle motion within the capillary ridge for spreading of suspensions which will provide us with the mechanism behind the observed spreading and instability characteristics.

- Investigation of the contact line instability for a variety of cases such as: for bimodal and multimodal suspensions, for non-neutrally buoyant particles and for non-Newtonian suspending liquids, and for particles with modified surface affinity with respect to the suspending liquid.

- Finally, mathematical models for the spreading of thin film of suspensions on a spinning disc could also be developed in future to find out the concentration variation in the capillary ridge region. We believe that the demonstrated approach will be valuable in theoretical studies of thin film flow of suspensions suitable for practical applications.

Bibliography

[1] Alexander Oron, Stephen H Davis, and S George Bankoff. Long-scale evolution of thin liquid films. *Rev. Mod. Phys.*, 69(3):931, 1997.

[2] RV Craster and OK Matar. Dynamics and stability of thin liquid films. *Rev. Mod. Phys.*, 81(3):1131, 2009.

[3] L. E. Scriven. Physics and applications of dip coating and spin coating. In *MRS proceedings*, volume 121, page 717, 1988.

[4] F. A. Denis, P. Hanarp, D. S. Sutherland, and Y. F. Dufrêne. Fabrication of nanostructured polymer surfaces using colloidal lithography and spin-coating. *Nano Lett.*, 2:1419, 2002.

[5] U. Mennicke and T. Salditt. Preparation of solid-supported lipid bilayers by spin-coating. *Langmuir*, 18:8172, 2002.

[6] D. B. Mitzi, L. L. Kosbar, C. E. Murray, M. Copel, and A. Afzali. High-mobility ultrathin semiconducting films prepared by spin coating. *Nature*, 428:299, 2004.

[7] P. Jasinski, S. Molin, M. Gazda, and H. U. Petrovsky, V.and Anderson. Applications of spin coating of polymer precursor and slurry suspensions for solid oxide fuel cell fabrication. *J. Power Sources*, 194:10, 2009.

[8] H. Hauser, B. Michl, S. Schwarzkopf, V. Kubler, C. Muller, M. Hermle, and B. Blasi. Honeycomb texturing of silicon via nanoimprint lithography for solar cell applications. *IEEE J. Photovoltaics*, 2:114, 2012.

[9] Yongbo Yuan, Gaurav Giri, Alexander L Ayzner, Arjan P Zoombelt, Stefan CB Mannsfeld, Jihua Chen, Dennis Nordlund, Michael F Toney, Jinsong Huang, and Zhenan Bao. Ultra-high mobility transparent organic thin film transistors grown by an off-centre spin-coating method. *Nat. commun.*, 5, 2014.

[10] Hao-Chiang Cho, Fu-Chu Chou, Ming-Wen Wang, and Chu-Shu Tsai. Effect of coriolis force on fingering instability and liquid usage reduction. *Jpn. J. Appl. Phys.*, 44(4L):L606, 2005.

[11] M. B. Mackaplow, I. E. Zarraga, and J. F. Morris. Rotary spray congealing of a suspension: effect of disk speed and dispersed particle properties. *J. Microencapsul.*, 23:793, 2006.

[12] Y. Senuma, S. Franceschin, J. G. Hilborn, P. Tissieres, I. Bisson, and P. Frey. Bioresorbable microspheres by spinning disk atomization as injectable cell carrier: from preparation to in vitro evaluation. *Biomaterials*, 21:1135, 2000.

[13] Yoshinori Senuma and Jöuns G Hilborn. High speed imaging of drop formation from low viscosity liquids and polymer melts in spinning disk atomization. *Polym. Eng. Sci.*, 42(5):969–982, 2002.

[14] B. Albertini, N. Passerini, F. Pattarino, and L. Rodriguez. New spray congealing atomizer for the microencapsulation of highly concentrated solid and liquid substances. *Eur. J. Pharm. Biopharm.*, 69:348, 2008.

[15] RP Fraser, N Dombrowski, and JH Routley. The filming of liquids by spinning cups. *Chem. Eng. Sci.*, 18(6):323–337, 1963.

[16] AR Frost. Rotary atomization in the ligament formation mode. *J. Agr. Eng. Res.*, 26(1):63–78, 1981.

[17] Huimin Liu. *Science and Engineering of Droplets:: Fundamentals and Applications*. William Andrew, 1999.

[18] Hao Peng, Na Wang, Dongxiang Wang, and Xiang Ling. Experimental study on the critical characteristics of liquid atomization by a spinning disk. *Ind. Eng. Chem. Res*, 55(21):6175–6185, 2016.

[19] Paul Oxley, Clemens Brechtelsbauer, Francois Ricard, Norman Lewis, and Colin Ramshaw. Evaluation of spinning disk reactor technology for the manufacture of pharmaceuticals. *Ind. Eng. Chem. Res*, 39(7):2175–2182, 2000.

[20] LM Cafiero, G Baffi, A Chianese, and RJJ Jachuck. Process intensification: precipitation of barium sulfate using a spinning disk reactor. *Ind. Eng. Chem. Res*, 41(21):5240–5246, 2002.

[21] A. G. Emslie, F. T. Bonner, and L. G. Peck. Flow of a viscous liquid on a rotating disk. *J. Appl. Phys.*, 29:858, 1958.

[22] M. A. Spaid and G. M. Homsy. Stability of newtonian and viscoelastic dynamic contact lines. *Phys. Fluids*, 8:460, 1996.

[23] S K Wilson, R Hunt, and B R Duffy. The rate of spreading in spin coating. *J. Fluid Mech.*, 413:65–88, 2000.

[24] Stanley Middleman. The effect of induced air-flow on the spin coating of viscous liquids. *Journal of applied physics*, 62(6):2530–2532, 1987.

[25] O K Matar, G M Sisoev, and C J Lawrence. Thin film flow over spinning discs: The effect of surface topography and flow rate modulation. *Chem. Engg. Sci.*, 63(8):2225–2232, 2008.

[26] E Momoniat and DP Mason. Investigation of the effect of the coriolis force on a thin fluid film on a rotating disk. *Int. J. Non-linear Mech.*, 33(6):1069–1088, 1998.

[27] T G Myers and J P F Charpin. The effect of the coriolis force on axisymmetric rotating thin film flows. *Int. J Non-linear Mech.*, 36(4):629–635, 2001.

[28] L. W. Schwartz and R. V. Roy. Theoretical and numerical results for spin coating of viscous liquids. *Phys. Fluids*, 16:569, 2004.

[29] TG Myers and M Lombe. The importance of the coriolis force on axisymmetric horizontal rotating thin film flows. *Chem. Engg. Processing: Process Intensification*, 45(2):90–98, 2006.

[30] Timothy J Rehg and Brian G Higgins. The effects of inertia and interfacial shear on film flow on a rotating disk. *Phys. Fluids*, 31(6):1360–1371, 1988.

[31] B Reisfeld, S G Bankoff, and S H Davis. The dynamics and stability of thin liquid films during spin coating. i. films with constant rates of evaporation or absorption. *J. Appl. Phys.*, 70(10):5258–5266, 1991.

[32] J A Moriarty, L W Schwartz, and E O Tuck. Unsteady spreading of thin liquid films with small surface tension. *Phys. Fluids A*, 3(5):733–742, 1991.

[33] Brian G Higgins. Film flow on a rotating disk. *Phys. Fluids*, 29(11):3522–3529, 1986.

[34] Chun Huh and LE Scriven. Hydrodynamic model of steady movement of a solid/liquid/fluid contact line. *J. Colloid and Interf. Sci.*, 35(1):85–101, 1971.

[35] L M Hocking. A moving fluid interface on a rough surface. . *Fluid Mech.*, 76(04):801–817, 1976.

[36] EB Dussan. On the spreading of liquids on solid surfaces: static and dynamic contact lines. *Annu. Rev. Fluid Mech.*, 11(1):371–400, 1979.

[37] Peter A Thompson and Sandra M Troian. A general boundary condition for liquid flow at solid surfaces. *Nature*, 389(6649):360–362, 1997.

[38] W Bate Hardy. Iii. the spreading of fluids on glass. *The London, Edinburgh, and Dublin Philosophical Magazine and Journal of Science*, 38(223):49–55, 1919.

[39] D Ausserré, AM Picard, and L Léger. Existence and role of the precursor film in the spreading of polymer liquids. *Phys. Rev. Lett.*, 57(21):2671, 1986.

[40] L Leger, M Erman, AM Guinet-Picard, D Ausserre, and C Strazielle. Precursor film profiles of spreading liquid drops. *Phys. rev. Lett.*, 60(23):2390, 1988.

[41] D1 Beaglehole. Profiles of the precursor of spreading drops of siloxane oil on glass, fused silica, and mica. *J Phys. Chem.*, 93(2):893–899, 1989.

[42] EO Tuck and LW Schwartz. A numerical and asymptotic study of some third-order ordinary differential equations relevant to draining and coating flows. *SIAM Rev.*, 32(3):453–469, 1990.

[43] Tim G Myers. Thin films with high surface tension. *SIAM Rev.*, 40(3):441–462, 1998.

[44] Javier A Diez, L Kondic, and Andrea Bertozzi. Global models for moving contact lines. *Phys. Rev. E*, 63(1):011208, 2000.

[45] IS McKinley, SK Wilson, and BR Duffy. Spin coating and air-jet blowing of thin viscous drops. *Phys. Fluids*, 11(1):30–47, 1999.

[46] N. Fraysse and G. M. Homsy. An experimental study of rivulet instabilities in centrifugal spin coating of viscous newtonian and non-newtonian fluids. *Phys. Fluids*, 6:1491, 1994.

[47] M. A. Spaid and G. M. Homsy. Stability of viscoelastic dynamic contact lines: An experimental study. *Phys. Fluids*, 9:823, 1997.

[48] A McIntyre and L N Brush. Spin-coating of vertically stratified thin liquid films. *J. Fluid Mech.*, 647:265–285, 2010.

[49] B S Dandapat and S K Singh. Two-layer film flow on a rotating disk: A numerical study. *Int. J. Non-Lin. Mech.*, 46(1):272–277, 2011.

[50] B S Dandapat and S K Singh. Two-layer film flow over a rotating disk. *Commun. Nonlin. Sci. Numer. Simul.*, 17(7):2854–2863, 2012.

[51] A. Acrivos, M. J. Shah, and E. E. Petersen. On the flow of a non-newtonian liquid on a rotating disk. *J. Appl. Phys.*, 31:963, 1960.

[52] S. A. Jenekhe and S. B. Schuldt. Coating flow of non-newtonian fluids on a flat rotating disk. *Ind. Eng. Chem. Fundam.*, 23:432, 1984.

[53] C. J. Lawrence and W. Zhou. Spin coating of non-newtonian fluids. *J. Non-Newtonian Fluid Mech.*, 39:137, 1991.

[54] T. J. Rehg and G. Higgins. Spin coating of colloidal suspensions. *AIChE J.*, 38:489, 1992.

[55] J P F Charpin, M Lombe, and T G Myers. Spin coating of non-newtonian fluids with a moving front. *Phys. Rev. E*, 76(1):016312, 2007.

[56] Bin Hu and Sarah L Kieweg. The effect of surface tension on the gravity-driven thin film flow of newtonian and power-law fluids. *Computers & fluids*, 64:83–90, 2012.

[57] A. Arora and P. Doshi. Fingering instability in the flow of a power-law fluid on a rotating disc. *Phys. Fluids*, 28(1):013102, 2016.

[58] H. E. Huppert. Flow and instability of a viscous current down a slope. *Nature*, 300:427, 1982.

[59] S M Troian, E Herbolzheimer, S A Safran, and J F Joanny. Fingering instabilities of driven spreading films. *Europhys. Lett.*, 10(1):25, 1989.

[60] A. L. Bertozzi and M. P. Brenner. Linear stability and transient growth in driven contact lines. *Phys. Fluids*, 9:530, 1997.

[61] I. S. McKinley and S. K. Wilson. The linear stability of a drop of fluid during spin coating or subject to a jet of air. *Phys. Fluids*, 14:133, 2002.

[62] F Melo, J F Joanny, and S Fauve. Fingering instability of spinning drops. *Phys. Rev. Lett.*, 63(18):1958, 1989.

[63] K. E. Holloway, P. Habdas, N. Semsarillar, K. Burfitt, and J. R. de Bruyn. Spreading and fingering in spin coating. *Phys. Rev. E*, 75:046308, 2007.

[64] J. Zhou, B. Dupuy, A. L. Bertozzi, and A. E. Hosoi. Theory for shock dynamics in particle-laden thin films. *Phys. Rev. Lett.*, 94:117803, 2005.

[65] T. Ward, C. Wey, R. Glidden, A. E. Hosoi, and A. L. Bertozzi. Experimental study of gravitation effects in the flow of a particle-laden thin film on an inclined plane. *Phys. Fluids*, 21:083305, 2009.

[66] N. Murisic, J. Ho, V. Hu, P. Latterman, T. Koch, K. Lin, M. R. Mata, and A. L. Bertozzi. Particle-laden viscous thin-film flows on an incline: Experiments compared with a theory based on shear-induced migration and particle settling. *Physica D*, 240:1661, 2011.

[67] N. Murisic, B. Pausader, D. Peschka, and A. L. Bertozzi. Dynamics of particle settling and resuspension in viscous liquid films. *J. Fluid Mech.*, 717:203, 2013.

[68] C. Ancey, N. Andreini, and G. Epely-Chauvin. The dam-break problem for concentrated suspensions of neutrally buoyant particles. *J. Fluid Mech.*, 724:95, 2013.

[69] S. Lee, Y. Stokes, and A. L. Bertozzi. Behavior of a particle-laden flow in a spiral channel. *Phys. Fluids*, 26:043302, 2014.

[70] L. Wang, A. Mavromoustaki, A. L. Bertozzi, G. Urdaneta, and K. Huang. Rarefaction-singular shock dynamics for conserved volume gravity driven particle-laden thin film. *Phys. Fluids*, 27:033301, 2015.

[71] B. D. Timberlake and J. F. Morris. Particle migration and free-surface topography in inclined plane flow of a suspension. *J. Fluid Mech.*, 538:309, 2005.

[72] J. R. de Bruyn, P. Habdas, and S. Kim. Fingering instability of a sheet of yield-stress fluid. *Phys. Rev. E*, 66:031504, 2002.

[73] H. Tabuteau, J. C. Baudez, X. Chateau, and P. Coussot. Flow of a yield stress fluid over a rotating surface. *Rheol. Acta*, 46:341, 2007.

[74] N. Balmforth, S. Ghadge, and T. Myers. Surface tension driven fingering of a viscoplastic film. *J. Non-Newtonian Fluid Mech.*, 142:143, 2007.

[75] B. P. Cook, O. Alexandrov, and A. L. Bertozzi. Linear stability of particle-laden thin films. *Eur. Phys. J. Special Topics*, 166:77, 2009.

[76] N. Grunewald, R. Levy, M. R. Mata, T. Ward, and A. L. Bertozzi. Self-similarity in particle-laden flows at constant volume. *J. Eng. Math.*, 66:53, 2010.

[77] Ching W Tang. Two-layer organic photovoltaic cell. *Appl. Phys. Lett.*, 48(2):183–185, 1986.

[78] George L Gaines. Langmuir–blodgett films of long-chain amines. *Nature*, 1982.

[79] G M Sisoev and V Ya Shkadov. Two-layer film flow over the surface of a rotating disc. *J. Engg. Phys. Thermopys.*, 55(3):999–1003, 1988.

[80] Yuriko Renardy. Viscosity and density stratification in vertical poiseuille flow. *Phys. Fluids*, 30(6):1638–1648, 1987.

[81] Nitin R Anturkar, Tasos C Papanastasiou, and James O Wilkes. Lubrication theory for n-layer thin-film flow with applications to multilayer extrusion and coating. *Chem. Engg. Sci.*, 45(11):3271–3282, 1990.

[82] Gilbert Strang and George J Fix. *An analysis of the finite element method*, volume 212. Prentice-Hall Englewood Cliffs, NJ, 1973.

[83] P M Gresho, R L Lee, and R L Sani. On the time-dependent solution of the incompressible navier-stokes equations in two and three dimensions. *Recent Adv. Numer. Meth. Fluids*, 1:27–29, 1980.

[84] P Hood. Note on frontal solution program1 for unsymmetric matrices. *Int. J. Numer. Methods Eng.*, 11(6):1055–1055, 1977.

[85] Paul Hood. Frontal solution program for unsymmetric matrices. *Int. J. Numer. Methods Eng.*, 10(2):379–399, 1976.

[86] Roy A Walters. The frontal method in hydrodynamics simulations. *Computers & Fluids*, 8(2):265–272, 1980.

[87] Talal T Al-Housseiny, Peichun A Tsai, and Howard A Stone. Control of interfacial instabilities using flow geometry. *Nature Phys.*, 8(10):747–750, 2012.

[88] Fernando A Castro, Carlos FO Graeff, Jakob Heier, and Roland Hany. Interface morphology snapshots of vertically segregated thin films of semiconducting polymer/polystyrene blends. *Polymer*, 48(8):2380–2386, 2007.

[89] P. B. Umbanhowar, V. Prasad, and D. A. Weitz. Monodisperse emulsion generation via drop break off in a coflowing stream. *Langmuir*, 16:347, 2000.

[90] I. Cohen, H. Li, J. L. Houghland, M. Mrksich, and S. R. Nagel. Using selective withdrawal to coat microparticles. *Science*, 292:265, 2001.

[91] S. L. Anna, N. Bontoux, and H. A. Stone. Formation of dispersions using "flow focusing" in microchannels. *Appl. Phys. Lett.*, 82:364, 2003.

[92] C. Cramer amd P. Fischer and E. J. Windhab. Drop formation in a co-flowing ambient fluid. *Chem. Engg. Sci.*, 59:3045, 2004.

[93] R. Suryo and O. A. Basaran. Tip streaming from a liquid drop forming from a tube in a co-flowing outer fluid. *Phys. Fluids*, 18:082102, 2006.

[94] S. Mintova and T. Bein. Microporous films prepared by spin-coating stable colloidal suspensions of zeolites. *Adv. Materials*, 13:1880, 2001.

[95] M. Pichumani, P. Bagheri, K. M. Poduska, W. Gonzàlez-Viñas, and A. Yethiraj. Dynamics, crystallization and structures in colloid spin coating. *Soft Mat.*, 9:3220, 2013.

[96] K. E. Holloway, H. Tabuteau, and J. R. de Bruyn. Spreading and fingering in a yield-stress fluid during spin coating. *Rheol. Acta*, 49:245, 2010.

[97] Irvin M Krieger and Thomas J Dougherty. A mechanism for non-newtonian flow in suspensions of rigid spheres. *Transac. Soc. Rheol.*, 3(1):137–152, 1959.

[98] J. Han and C. Kim. Spreading of a suspension drop on a horizontal surface. *Langmuir*, 28:2680, 2012.

[99] H. J. Jeong, W. R. Hwang, C. Kim, and S. J. Kim. Numerical simulations of capillary spreading of a particle-laden droplet on a solid surface. *J. Mat. Proc. Tech.*, 210:297, 2010.

[100] M. P. Brenner. Instability mechanism at driven contact lines. *Phys. Rev. E*, 47:4597, 1993.

[101] David Leighton and Andreas Acrivos. The shear-induced migration of particles in concentrated suspensions. *J. Fluid Mech.*, 181:415–439, 1987.